MACROSCALE MODELING OF THE PIEZORESISTIVE EFFECT IN NANOFILLER-MODIFIED FIBER-REINFORCED COMPOSITES

by

Sultan M. Ghazzawi

A Dissertation

Submitted to the Faculty of Purdue University

In Partial Fulfillment of the Requirements for the degree of

Doctor of Philosophy

School of Aeronautics and Astronautics

West Lafayette, Indiana

May 2024

THE PURDUE UNIVERSITY GRADUATE SCHOOL
STATEMENT OF COMMITTEE APPROVAL

Dr. Tyler N. Tallman, Chair

School of Aeronautics and Astronautics

Dr. Wenbin Yu

School of Aeronautics and Astronautics

Dr. Dianyun Zhang

School of Aeronautics and Astronautics

Dr. Fabio Semperlotti

School of Mechanical Engineering

Approved by:

Dr. Gregory Blaisdell

In The Name of Allah, The Most Gracious, The Most Merciful

ACKNOWLEDGMENTS

I would like to begin by thanking Almighty Allah for all the blessings in my life, including the opportunity to contribute to the collective body of knowledge. I am deeply grateful to the Saudi Arabian government and King Fahd University of Petroleum and Minerals (KFUPM) for their kind support, which allowed me to pursue doctoral studies. Their financial assistance and facilitation were invaluable. I am grateful for KFUPM's support from my undergraduate studies in 2010 to my master's degree and doctoral studies. Being a member of KFUPM and a Saudi citizen are two things I am very proud of.

Dr. Tyler Tallman, my Ph.D. mentor, played a crucial role in making all of this possible. The commitment and mentorship provided by him have played a crucial role in shaping my research path. The profound impact of his insights and wisdom on my academic and personal development has been significant.

I would like to express my gratitude and extend my sincere thanks to my esteemed committee members, Dr. Wenbin Yu, Dr. Dianyun Zhang, and Dr. Fabio Semperlotti, for their invaluable input and constant encouragement in pushing the limits of my research. Their profound knowledge and insightful advice have played a pivotal role in the development of this project.

I appreciate my family and friends. A large part of my life is owed to my mother, Fayruz Talib. She has always prayed and supported me. My support from her is invaluable. I also remember my father, Mohammedali Ghazzawi, whose dedication I still feel. The love and devotion of my spouse, Shrooq Bukhari, is greatly appreciated. She has given me strength throughout this journey and has contributed to my success. Thank you, dear friends, for your endless help. Your help is greatly appreciated.

Finally, I hope that this effort will benefit someone somewhere in the world. I remain optimistic that this is the start of more productive and groundbreaking research that will benefit society.

TABLE OF CONTENTS

LIST OF TABLES

LIST OF FIGURES

ABSTRACT

The demand and utilization of fiber-reinforced composites are increasing in various sectors, including aerospace, civil engineering, and automotive industries. Non-destructive methods are necessary for monitoring fiber-reinforced composites due to their complex and often visually undetectable failure modes. An emerging method for monitoring composite structures is through the integration of self-sensing capabilities. Self-sensing in nanocomposites can be achieved through nanofiller modifications, which involve introducing an adequate amount of nanofillers into the matrix, such as carbon nanotubes (CNTs) and carbon nanofillers (CNFs). These fillers form an electrically well-connected network that allows the electrical current to travel through conductive pathways. The disruption of connectivity of these pathways, caused by mechanical deformations or damages, results in a change in the overall conductivity of the material, thereby enabling intrinsic self-sensing.

Currently, the majority of predictive modeling attempts in the field of self-sensing nanocomposites have been dedicated to microscale piezoresistivity. There has been a lack of research conducted on the modeling of strain-induced resistivity changes in macroscale fiber-matrix material systems. As a matter of fact, no analytical macroscale model that addresses the impact of continuous fiber reinforcement in nanocomposites has been presented in the literature. This gap is significant because it is impossible to make meaningful structural condition predictions without models relating observed resistivity changes to the mechanical condition of the composite. Accordingly, this dissertation presents a set of three research contributions. The overall objective of these contributions is to address this knowledge gap by developing and validating an analytical model. In addition to advancing our theoretical understanding, this model provides a practical methodology for predicting the piezoresistive properties of continuous fiber-reinforced composites with integrated nanofillers.

To bridge the above-mentioned research gap, three scholarly contributions are presented in this dissertation. The first contribution proposes an analytical model that aims to predict the variations in resistivity within a material system comprising a nanofiller-modified polymer and continuous fiber reinforcement, specifically in response to *axial* strain. The fundamental principle underlying our methodology involves the novel use of the concentric

cylindrical assembly (CCA) homogenization technique to model piezoresistivity. The initial step involves the establishment of a domain consisting of concentric cylinders that represent a continuous reinforcing fiber phase wrapped around by a nanofiller-modified matrix phase. Subsequently, the system undergoes homogenization to facilitate the prediction of changes in the axial and transverse resistivity of the concentric cylinder as a consequence of longitudinal deformations. The second contribution investigates the effect of *radial* deformations on piezoresistivity. Here, we demonstrate yet another novel application of the CCA homogenization technique to determine piezoresistivity. This contribution concludes by presenting closed-form analytical relations that describe changes in axial and transverse resistivity as functions of externally applied radial strain. The third contribution involves computationally analyzing piezoresistivity in fiber-reinforced laminae by using three-dimensional representative volume elements (RVE) with a CNF/epoxy matrix. By comparing the single-fiber-based analytical model with the computational model, we can investigate the impact of interactions between multiple adjacent fibers on the piezoresistive properties of the material. The study revealed that the differences between the single-fiber CCA analytical model and the computational model are quite small, particularly for composites with low- to moderate-fiber volume fractions that undergo relatively minor deformations. This means that the analytical methods herein derived can be used to make accurate predictions without resorting to much more laborious computational methods.

In summary, the impact of this dissertation work lies in the development of novel analytical closed-form nonlinear piezoresistive relations. These relations relate the electrical conductivity/resistivity changes induced by axial or lateral mechanical deformations in directions parallel and perpendicular to the reinforcing continuous fibers within fiber-reinforced nanocomposites and are validated against in-depth computational analyses. Therefore, these models provide an important and first-ever bridge between simply observing electrical changes in a self-sensing fiber-reinforced composite and relating such observations to the mechanical state of the material.

1. INTRODUCTION AND MOTIVATION

A version of this chapter has been previously published in *Composites Science and Technology* [1].

1.1 Introduction

Due to their excellent strength-to-weight ratio, fiber-reinforced composites have found extensive use in a variety of industries, including the aerospace, civil, automotive, medical, and marine sectors [2]–[13]. Non-destructive evaluation (NDE) is often used to ensure the structural integrity of these materials due to their complicated failure mechanisms [14]–[23]. However, many NDE procedures are routinely carried out at predetermined times, which may allow unchecked damage growth between inspections. Continuous monitoring via embedded sensing has been studied as a possible solution to this problem. Sensors can be surface-mounted or embedded; however, sensor integration within the composite creates weak areas and complicates manufacturing. Therefore, self-sensing materials, in which the condition is determined by changes in properties such as electrical conductivity, have attracted interest from the scientific and engineering communities [24]–[27].

The piezoresistive effect, a prevalent method of self-sensing, enables materials to exhibit deformation-dependent electrical conductivity (or its inverse, resistivity). Materials exhibiting piezoresistivity include semiconductors such as silicon and germanium [28], as well as polymer composites reinforced with conductive fillers such as carbon black, graphite, carbon nanofibers (CNFs), and carbon nanotubes (CNTs). This phenomenon, induced by the integration of a sufficient amount of micro- to nanoscale conductive fillers, such as CNFs or CNTs, into cement or polymer-based composites [29]–[32], arises from the formation of an electrically well-connected network of nanofillers within the matrix. This network enables the electric current to flow through conductive pathways. Mechanical effects that alter these pathways' connectivity manifest as changes in conductivity, facilitating intrinsic self-sensing [33]–[37]. In other words, mechanical stress leads to deformation of the polymer matrix and reorientation or movement of the conductive filler particles [38], as well as changes in

the distance between these particles, affecting tunneling resistance and, consequently, the overall resistivity of the composite [39], [40]. Piezoresistivity is also observed in carbon fiber-reinforced polymer composites (CFRPCs) with nonconductive matrix phases due to the contact between adjacent in-plane conductive fibers or interlaminar crossing fibers, which allows for electrical transport between carbon fiber threads and/or layers [41]–[43].

It is important to highlight that although this research focuses on self-sensing via the piezoresistive effect, one should differentiate between piezoresistivity and piezoelectricity effects because, despite similar sounding names, they are fundamentally different in their physical mechanisms. In piezoresistive materials, the electrical properties change in response to mechanical stress, making them suitable for applications where changes in force, pressure, or strain need to be detected by observing the resultant variation in electrical resistivity of the material. On the other hand, piezoelectric materials generate an electrical charge when subjected to mechanical stresses, or vice versa; i.e., these materials can generate mechanical strains when subjected to an external electric field, a phenomenon called the inverse piezoelectric effect. Unlike the mechanism that causes the piezoresistive effect, which is due to the electrical network formed by the inclusion of conductive nanofillers, the piezoelectric effect occurs because the crystal structure in these materials lacks a center of symmetry; the crystal lattice is arranged in a way that ions occupy positions that do not mirror each other across a plane of symmetry. When the structure is under mechanical stress, these ions are displaced such that positive and negative ions move relative to each other but remain bound within the lattice structure, causing an asymmetrical distribution of the charges and leading to accumulation of positive charges on one side of the material and negative charges on the other. As a result, an internal electric field is generated, which has a direction and magnitude directly related to the direction and amount of externally applied stress. Due to their properties, piezoelectric materials are often used as actuators [44]–[48], where voltage is applied to induce mechanical strain, or sensors, where electrical signals are observed due to the material being subjected to mechanical stress or vibrations. These piezoelectric sensors play an important role in structural health monitoring and NDE, as suggested by recent studies [49]–[53].

The subsequent sections will first delve into the significance of piezoresistivity modeling, highlight its necessity for fiber-reinforced composites, and discuss the motivations driving this research work. Following this, an examination of current modeling approaches will be provided, alongside a presentation of notable existing models from the literature. The discussion will then extend to a comparison between piezoresistivity models and thermal transfer models, illustrating the distinctions and connections between these two types of model.

1.2 Motivation

A limitation of piezoresistive self-sensing is that inspectors typically do not care about electrical properties but rather want to know the stress, strain, and damage states of the composite. To derive this information from the material's electrical signature, models that correlate conductivity with the mechanical condition are essential. For further insight, refer to Figure 1.1, which depicts a piezoresistive plate with a central hole created by Hassan and Tallman [54]. This plate was subjected to various uniaxial tension tests during which changes in conductivity were monitored. The question arises from the observed conductivity changes distribution, obtained via electrical impedance tomography (EIT): Can any of these conductivity images be used to predict an imminent failure of the plate? To accurately determine this, it is necessary to deduce the stress-strain state of the plate from the observed changes in electrical properties. Thus, piezoresistivity models, where the change in resistivity (or conductivity) is expressed as a function of strain, are vital for inferring the mechanical state of the composite from the electrical data collected using inverse problem techniques. For instance, using a simple damage model, Hashim and Tallman [54] successfully identified the size and shape of delamination damage in a CNF-modified glass fiber/epoxy laminate by applying a genetic algorithm to invert the model. They and other researchers have also succeeded in using metaheuristic and deep learning algorithms to deduce full-field stresses and strains in a CNF/epoxy plate with a through-hole under tension [54]–[56]. Recent studies highlight the crucial role of detecting, imaging, and predicting structural damage within composite materials using EIT and inverse problem techniques [57]–[63]. These studies

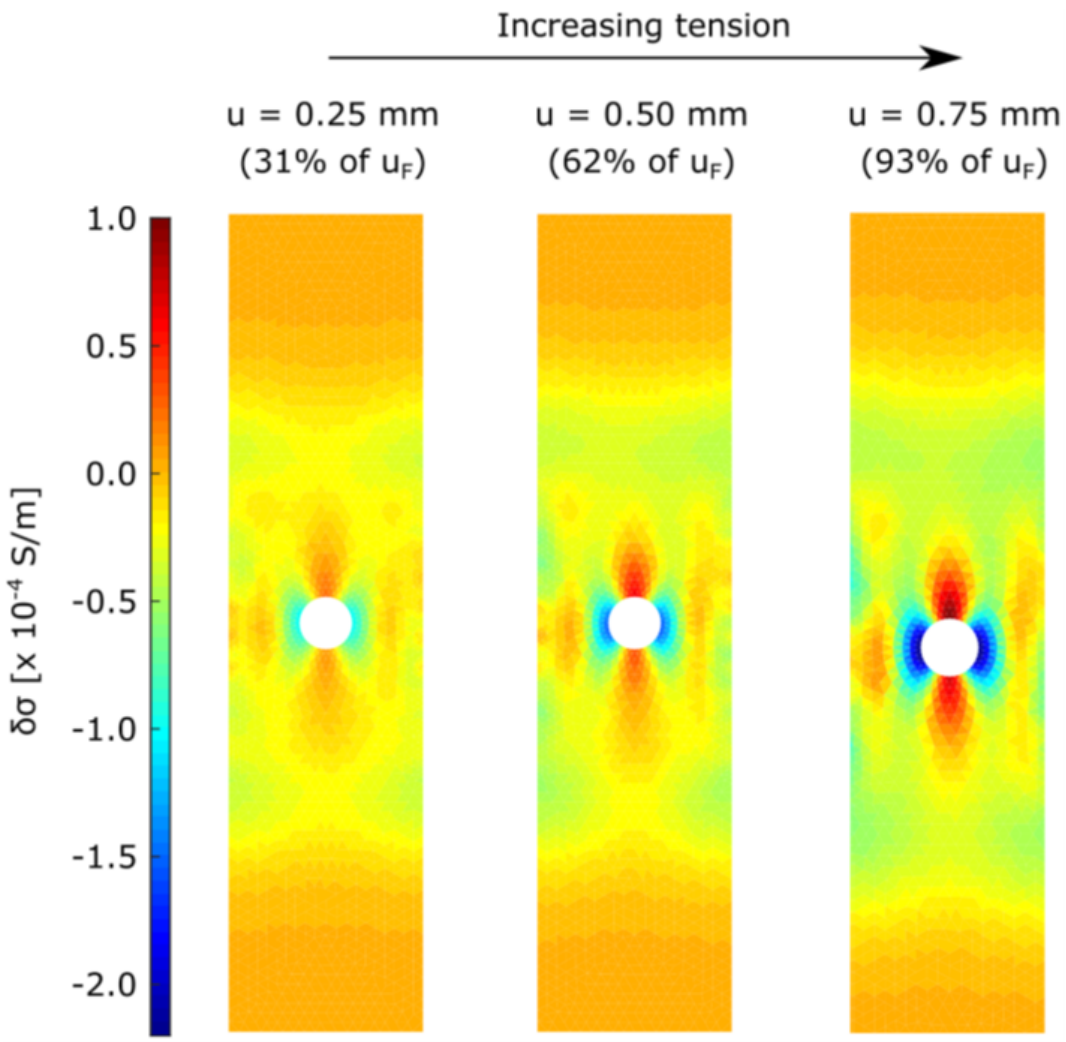

Figure 1.1. Observed distribution of conductivity changes via electrical impedance tomography forward problem [54].

emphasize the necessity of piezoresistivity models for deducing the mechanical state of the composite from observed changes in electrical conductivity.

Despite the previously discussed significance of piezoresistive models, there remains a notable deficiency in the literature regarding the modeling of fiber-reinforced composites with piezoresistive matrices. In fact, very few works have explored piezoresistivity in fiber-reinforced composites with conductive matrices. In these works, piezoresistivity is modeled exclusively using computational micromechanical techniques [64], [65]. However, there is

no analytical macroscale piezoresistivity model for fiber-reinforced, nanofiller-modified composites in the available literature. These macroscale analytical models provide closed-form relations dealing with the composite holistically and can offer accurate and close-to-real-life structural-level predictions. They do not consider individual filler locations, movements, etc., which can vary randomly, making it nearly impossible to precisely replicate the macroscale piezoresistive behavior of composites by considering individual filler locations and orientations. In addition, these analytical models can be considered as convenient tools for identifying the mechanical conditions of fiber-reinforced nanocomposites.

To be more explicit, research to date has almost exclusively focused on simulating piezoresistivity at the microscale to nanoscale levels without considering the effect of a continuous fiber reinforcement phase. Since the continuous fiber phase is crucial for structural composites, this represents a significant gap in the current state of knowledge. Consequently, there is a need for the development of analytical models that incorporate fiber reinforcements and have the ability to be implemented at structural levels.

This dissertation work is motivated by the need to fill the previously described gap in the state-of-the-art, which is the lack of analytical models that accurately predict the piezoresistive effect in continuous fiber-reinforced nanocomposites at structural scales. Macroscale models that account for the fiber-reinforcement phase are required if this technology is to be utilized to make meaningful structural-scale predictions of composite health and condition.

1.3 Summary of Existing Literature

In light of the preceding discussion, there is a clear need for piezoresistive models. These models are crucial because they enable engineers and researchers to embed self-sensing capabilities into structures and make meaningful predictions of mechanical condition from electrical data. To this end, existent modeling approaches for piezoresistivity are covered in subsequent discussions. These approaches can be broadly categorized into three main categories: resistor-network models, computational-based micromechanical models, and analytical models.

1.3.1 Resistor-Network Models

In resistor network modeling, groups of individual conductive fillers (often one-dimensional stick-like fillers such as CNTs or CNFs) are treated as resistor elements, as are inter-filler electron tunneling junctions [66]–[80], as illustrated in Figure 1.2. The piezoresistive effect is incorporated into these models by allowing the stick-like fillers to translate and rotate due to applied deformation. This approach provides good insight into the interaction of nanofillers and their agglomerations. However, it is also of limited use for large-scale predictions due to the necessity of modeling individual fillers, which leads to an overall high computational cost. Furthermore, this process generally does not explicitly model the matrix phase, which may lead to lower accuracy levels, as found by Hu et al. [77]. Continuous fiber reinforcement is also not considered. Thus, due to these limitations, resistor network modeling is not preferable for developing a macroscale piezoresistive model that incorporates continuous fiber reinforcement, as high accuracy and low computational cost are highly desired for structural-level applications.

1.3.2 Computational Micro-Mechanics Models

Another modeling approach relies on computational micromechanical techniques (e.g., finite element method or peridynamics) [81]–[89]. In this approach, unlike the previously discussed equivalent resistor network modeling, both individual fillers and the surrounding matrix are simulated. This enables the consideration of mechanical factors, such as matrix-to-nanofiller separations illustrated in Figure 1.3. Piezoresistivity at the micro and nanoscales, influenced by factors like inter-filler electron transport and matrix-filler debonding, significantly affects the electromechanical behaviors of composites at the macroscale level. Despite providing rich nanoscale information, these models also simulate individual nanofillers, making them computationally prohibitive for structural-scale predictions. Although computational modeling allows for the analysis of more complex loading conditions compared to other approaches, it necessitates the imposition of periodic boundary conditions (PBCs) on the representative volume element (RVE), as depicted in Figure 1.4, to ensure microscale responses accurately reflect the macroscale response of the composite structure.

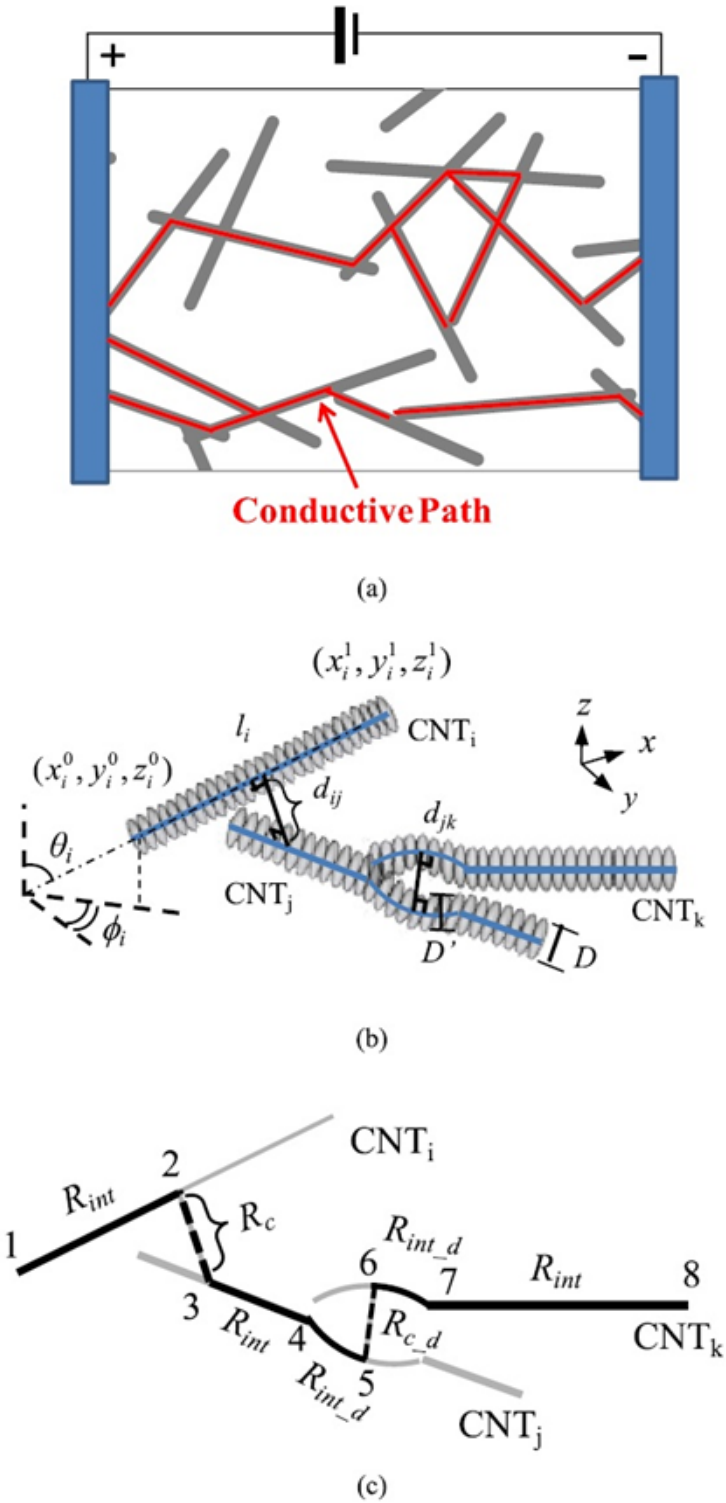

Figure 1.2. The modeling approach of an individual conductive fillers as equivalent resistors within a CNT agglomerate for the piezoresistive model developed by Gong et al. [72].

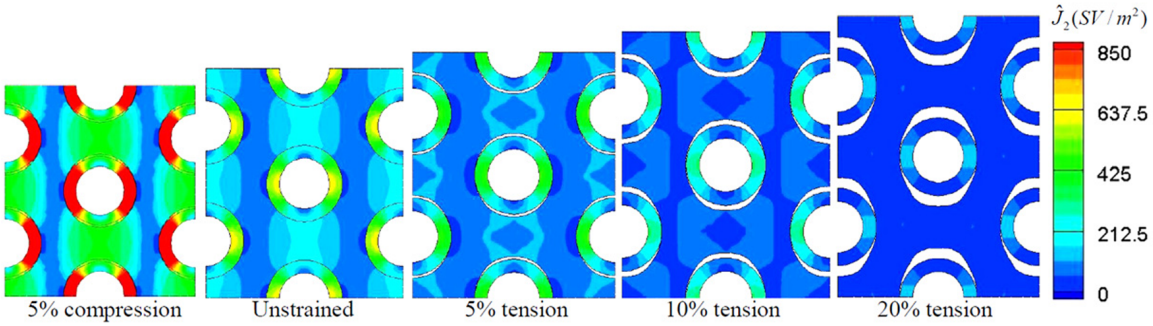

Figure 1.3. Images, illustrated by Chaurasia et al. [81], depict the progression of localized separation at the interface surrounding a carbon nanotube (CNT) within a hexagonal nanoscale representative volume element (RVE), in compression, unstressed and tension conditions. These pictures emphasis that computational models can take matrix-filler separations into account

While PBCs improve accuracy, they significantly increase the computational cost due to the generation of a large number of additional constraint equations. Consequently, computationally modeling fiber-reinforced nanocomposites would be highly inefficient and potentially less accurate, since considering individual fillers and continuous fibers (their locations, dispersion, and orientations) at the macroscale level is impractical due to their often random distribution within the matrix.

1.3.3 Analytical Models

Due to the computational costs of modeling individual fillers, researchers have also explored analytical modeling of the piezoresistive effect [90]–[95]. The general approach in these models is to predict piezoresistivity based on the strain state, as well as the mechanical and geometrical properties of the composite using micromechanical homogenization techniques. For instance, Garcia-Macias and colleagues [92], [96] utilized mean-field homogenization methods to model the piezoresistive effect. To elaborate, Garcia-Macias et al. [96] calculated the effective conductivity by averaging over all possible orientations of the fillers, as illustrated in Figure 1.5. One of the major advantages of analytical models is that they are generally less computationally demanding because, unlike computational and equivalent

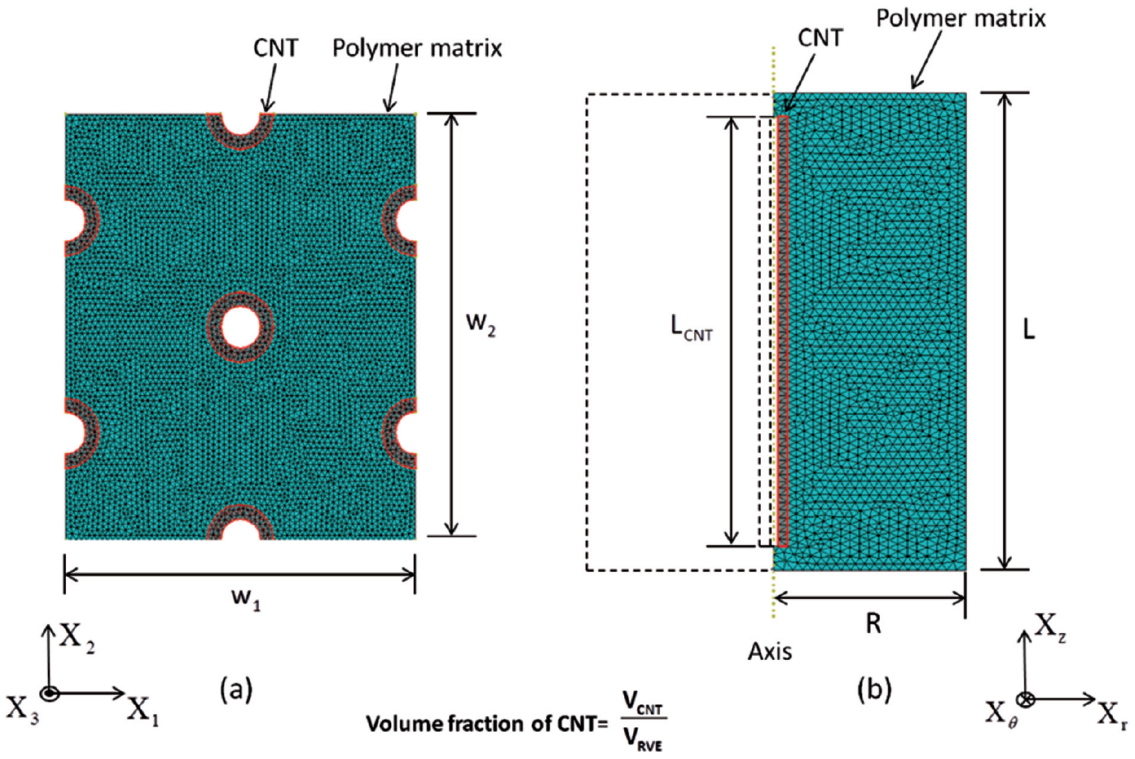

Figure 1.4. The representative volume elements used by Ren and Seidel [83] for their computational analysis.

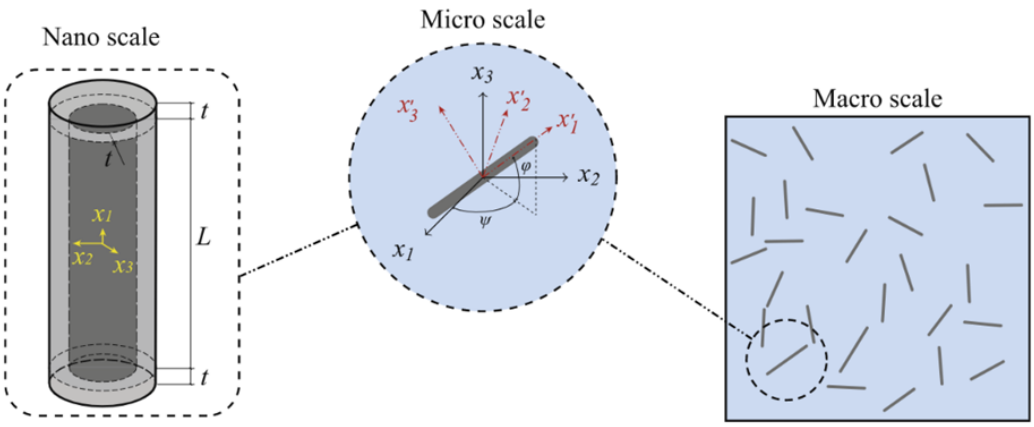

Figure 1.5. Garcia-Macias et al. applied mean-field homogenization in CNT cement-based composite to analytically model the piezoresistivity [96].

resistor network models, fillers are not modeled individually. Furthermore, they provide closed-form relations, such as in the model developed by Tallman and Wang [97], who used excluded volume theory to incorporate strain into an existing nanocomposite conductivity model by Takeda et al. [98]. Panozzo et al. [99] also offered an analytical closed-form relationship by modeling conductive networks of CNTs within a polymeric matrix, accounting for the three-dimensional random orientations of the nanofillers, CNT waviness, and CNT entanglement. These analytical relations are often adaptable to structural-level applications and are generally easier to apply in inverse problem applications, making this approach most suitable for developing a macroscale model for predicting strain-induced resistivity changes in fiber-reinforced nanofiller-modified composites. However, it is important to note that analytical models often rely on predetermined idealizations and assumptions, such as estimating averages of inter-filler distances and filler orientations, and they do not account for continuous fiber phases, which makes them of limited usefulness to structural composites.

1.4 Comparison to Thermal Transfer Models

This section aims to highlight the distinctions between thermal transport models and the modeling approach employed in this dissertation, which primarily concentrates on electric dif-

fusion. To address any potential ambiguity surrounding the similarities between the present study and the thermal diffusion models in fiber-reinforced composites, it is first important to acknowledge that both phenomena can be mathematically modeled using analogous governing partial differential equations (PDEs), which are derived from Laplace's second-order PDEs. As a result, several analytical homogenization techniques used in finding the effective electrical properties of a composite can also be implemented in heat flow boundary value problems (BVPs) to find the effective thermal properties. For example, the concentric cylinders assemblage homogenization approach, also known as the composite cylinder assemblage (CCA) approach, has been used to find the effective electrical properties of fiber-reinforced composites [100], as well as the effective thermal conductivities of fiber-reinforced composites [101], [102]. However, the following points outline the primary differences between our piezoresistivity system and thermal transport systems in terms of the underlying physics and modeling.

- **Different mechanisms at nanoscale**

  Strain-induced changes in thermal properties have been observed primarily in nanoscale structures such as monolayer silicene, silicon nanowires, and single-walled carbon nanotubes [101], [103]–[106]. However, there is a significant difference between the mechanisms behind the strain-induced electrical and thermal conductivity changes at *nanoscale levels*. Piezoresistivity in nanocomposites is mainly caused by the electron-hopping effect, in which electrons (real particles with charge) move between adjacent nanofillers. However, the modulation of thermal conductivity under strain is strongly dependent on the unique characteristics of the material, such as its lattice structure, bond strength, and frequency variations of phonons (quantized modes of vibration of atoms in a crystal lattice) [104], [106]. Basically, changes in deformation-dependent thermal conductivity at nanoscale levels are caused by variations in the *vibration frequencies* of atoms within a crystal lattice, unlike piezoresistivity caused by the movement of electrons. This distinction results in fundamentally different mathematical frameworks that describe changes in thermal and electrical properties. In other words, unlike piezoresistivity, which is caused by the movement of electrons, deformation-

dependent thermal conductivity changes at nanoscale levels are caused by variations in the vibration frequencies of atoms within a crystal lattice. This main difference leads to a fundamentally different mathematical framework for representing the variation mechanism.

- **No strain dependency in thermal transport models of fiber-reinforced macroscale structures**

  Existing models in the literature that address thermal transport in fiber-reinforced composites do not incorporate strains [107]–[111]. The thermal properties of fiber-reinforced composites may be temperature-dependent [102]. However, to the best of our knowledge, strain-induced thermal conductivity changes have not been observed (yet even modeled) in fiber-reinforced macroscale structures. They have hardly been observed in a very limited number of nanofiller-modified polymeric composites without a continuous fiber reinforcement phase in which specific types of nanofillers, such as cellulose nanocrystals (CNC) [112], are used. These fillers must be highly crystalline and disperse well in the matrix, unlike carbon nanofibers, which are vulnerable to form more agglomerations.

2. PROBLEM STATEMENT, RESEARCH GOAL, DISSERTATION CONTRIBUTIONS, AND DISSERTATION ORGANIZATION

In light of the previous discussion in Chapter 1, the following research problem statement and goal are proposed.

2.1 Problem Statement

A critical deficiency in the current state of the art regarding macroscale piezoresistivity models for continuous fiber-reinforced nanocomposites is identified in this dissertation. The potential for self-sensing in these materials, which could enhance safety through integrated NDE, is an important consideration. Piezoresistive models are necessary in order to infer the mechanical state of the composite from the observed electrical condition. However, the lack of macroscale analytical models for piezoresistivity in nanofiller-modified composites with continuous fiber reinforcement prevents us from exploiting electrical data for generating meaningful predictions of the mechanical condition.

2.2 Research Goal

The primary objective of this study is to construct an analytical model at a macroscopic level that accurately predicts the relationship between resistivity/conductivity and strain in continuous fiber-reinforced composites having nanofiller-modified matrices. This goal, when integrated with piezoresistive inversion techniques (i.e., deducing full-field mechanics from electrical observations by inverting piezoresistivity relationships), will pave the way for material state awareness in next-generation composites, establishing new possibilities for monitoring and optimizing composite structures.

2.3 Dissertation Contributions

To accomplish the previously stated research goal, this dissertation will make three research contributions, as summarized in the following.

- Research Contribution 1: Analytical Modeling of *Axial* Strain Piezoresistivity

  At this stage, we work at the single-fiber level, presenting a novel use of the CCA electrical homogenization technique to characterize the piezoresistive effect in continuous fiber-reinforced nanocomposites, where the reinforcing fiber is represented as a long cylinder surrounded by a nanofiller-modified matrix phase. The significance of this contribution lies in the fact that the CCA method delivers analytical closed-form relations that capture the changes in axial and transverse resistivity caused by axial strain in fiber-reinforced composites.

- Research Contribution 2: Analytical Modeling of *Radial* Strain Piezoresistivity

  Here, we present another novel use of the CCA homogenization methodology to identify the piezoresistivity characteristics of fiber-reinforced nanofiller-modified composites induced by *radial* strain. By the end of this contribution, closed-form analytical relations are developed to describe the axial and transverse resistivity changes as functions of externally applied radial strain. This contribution, along with the first, addresses a critical gap in the current literature by offering closed-form macroscale analytical piezoresistive relations that can be extended for structural sensing applications.

- Research Contribution 3: Lamina-Level Validation via Computational Analyses

  Next, we will use computational methods (i.e., FEA) to analyze the piezoresistivity of a fiber-reinforced nanocomposite lamina. This is achieved by using a representative volume element that may have fibers arranged in a certain manner, such as the hexagonal packing arrangement, to reflect a unidirectional fiber group consisting of several adjacent fibers that are embedded inside a piezoresistive matrix phase. Then, the impact of the interaction between these fibers on the overall electrical property and piezoresistivity of the composite is investigated. The importance of this contribution is that it provides insight into how the piezoresistive effect at the lamina level might differ from that at a single-fiber level obtained previously via the CCA analytical approach. By the end of this contribution, it is demonstrated that the proposed CCA model offers an accurate and easy-to-use piezoresistive macroscale modeling tool, despite the minor discrepancies observed at high fiber volume fractions. These marginal

deviations, which are even less pronounced at small deformations, are compensated for by the simplicity and low computational cost associated with analytical models.

2.4 Dissertation Organization

The remainder of this dissertation is organized as follows. First, the derivation of analytical axial and lateral resistivity-strain relations for composites under longitudinal deformations is presented. Then, the developed CCA model is demonstrated using carbon fiber and glass fiber-reinforced nanocomposites. Next, the derivation of piezoresistive relations for axial and transverse resistivity changes caused by radial strain is illustrated, and again, the model is demonstrated using glass and carbon fiber nanocomposites. A computational modeling approach for the piezoresistivity of a unidirectional fiber-reinforced lamina is presented. We will compare the results obtained using the CCA analytical model and the computational finite element approach to gain deeper insight into the influence of adjacent fibers on the overall macroscale piezoresistivity response of the composite. Finally, we present a summary, followed by conclusions and recommendations for future work.

3. ANALYTICAL MODELING OF AXIAL STRAIN PIEZORESISTIVITY

This chapter was previously published in *Composites Science and Technology* [1].

3.1 Introduction

In this chapter, we establish a relationship between the axial strain and the resulting changes in the axial and transverse resistivity of a nanofiller-modified epoxy with fiber reinforcement. For simplicity during development of the model, we assume that the fiber reinforcement is elastically transversely isotropic and that the matrix is elastically isotropic. To begin, the system is homogenized; it is made up of two concentric cylinders, the inner of which represents the fiber reinforcement while the outer is the piezoresistive matrix phase (e.g., epoxy modified with CNTs or CNFs). In particular, we make use of the resistivity-strain relation proposed by Koo and Tallman [113] for the piezoresistive matrix in conjunction with the CCA elasticity model (to obtain the elasticity solution of a deformed assembly). Note that the matrix resistivity-strain relation was experimentally validated in the original work by Koo and Tallman [113].

To develop the model, assume that a continuous reinforcing fiber is represented by a long cylinder of radius a that is surrounded by nanofiller-modified matrix. The entire assembly is represented by two concentric cylinders with an overall radius of b. The end goal is to homogenize the composite in such a way that the piezoresistive properties of the homogenized system are equivalent to those of the inhomogeneous cylinder, as shown in Figure 3.1. Note that the cylindrical coordinate system is defined such that the z-axis points along the longitudinal/axial direction, and the origin of the coordinate system is at the center of the concentric circles that make up the cross section.

The model is constructed first by considering the governing equation for the three-dimensional steady-state electrical diffusion, which is shown in equation (3.1), where $\mathbf{J}$ is the

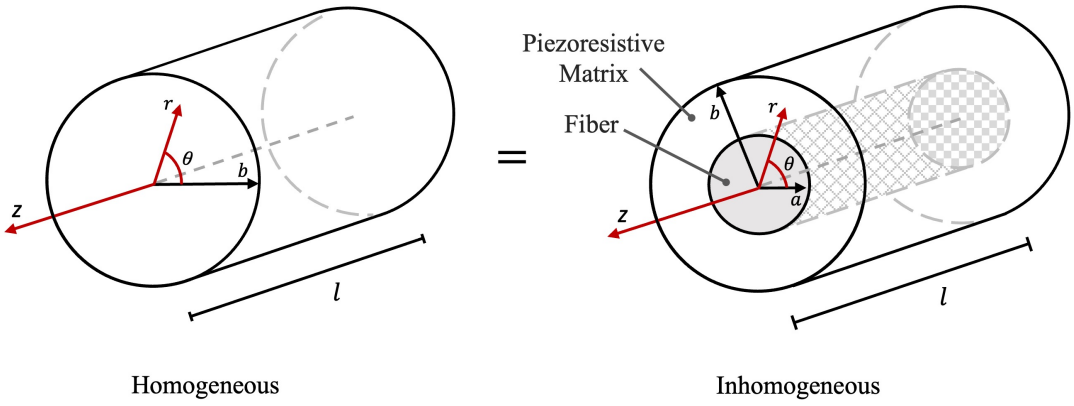

Figure 3.1. Concentric cylinders assemblage and homogenization. Note that in the inhomogeneous image, the gray inner cylinder represents the continuous fiber reinforcement. Our goal is to replicate the resistivity change-strain response of the inhomogeneous system in the homogeneous system.

vector of the current density distribution, ϕ is the electrical potential, and ρ is the electrical resistivity.

$$\nabla \cdot (-\mathbf{J}) = \nabla \cdot \frac{1}{\rho} \nabla \phi = 0 \tag{3.1}$$

It is worth mentioning that the resistivity ρ can be a second-order tensor as follows:

$$\rho^c = \begin{bmatrix} \rho_r^c & 0 & 0 \\ 0 & \rho_\theta^c & 0 \\ 0 & 0 & \rho_z^c \end{bmatrix} \tag{3.2}$$

where the subscripts r, θ, and z represent the radial, angular, and axial directions, respectively, while the superscript c denotes that this is the resistivity of the homogenized composite. Note that for fibers aligned with the z-axis, the radial and angular resistivity values are assumed to be the same and will be denoted throughout the forthcoming analysis as ρ_2^c, which is the transverse resistivity (i.e., $\rho_r^c = \rho_\theta^c = \rho_2^c$), whereas the axial resistivity of the composite ρ_z^c will be referred to as ρ_1^c. It is also important to say that throughout this manuscript, both the fiber and the matrix phases are going to be assumed electrically isotropic; that is, the resistivity of the fiber is ρ^f, while the resistivity of the matrix is ρ^m. To be more explicit, over the course of the entire manuscript, any ρ with a subscript 1 refers to axial resistivity, while any ρ with a subscript 2 refers to transverse resistivity.

3.2 Axial Piezoresistivity

Next, we look to homogenize the piezoresistive relation for the CCA along the longitudinal direction. To find the change in resistivity in the longitudinal direction due to axial strain, we begin by assuming that the potential gradient only exists along the longitudinal axis (i.e., by putting voltage or Dirichlet boundary conditions on each end of the composite cylinder). For this case, the steady-state electrical conductivity relation in equation (3.1) is reduced to a second-order ordinary differential equation shown in equation (3.3) below.

$$\frac{1}{\rho} \frac{d^2\phi}{dz^2} = 0 \tag{3.3}$$

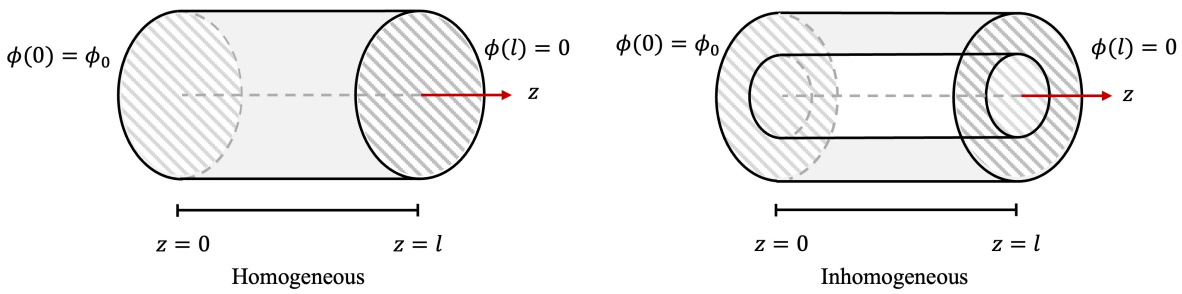

Figure 3.2. Dirichlet (voltage) boundary conditions are imposed at both ends of the inhomogeneous system and the homogeneous system.

We next express the change in electric potential of a one-dimensional cylinder by integrating equation (3.3), which results in the following:

$$\phi(z) = Az + B. \tag{3.4}$$

In this equation, A and B are integration constants, which are determined by imposing boundary constraints on both systems as shown in Figure 3.2, as follows:

$$\phi(z = 0) = \phi_0 \tag{3.5a}$$

$$\phi(z = l) = 0 \tag{3.5b}$$

where ϕ_0 represents the applied voltage at $z = 0$. The applied voltage is set to zero at the other end; that is, at $z = l$, where l is the length of the assemblage. After imposing the aforementioned boundary conditions, we obtain the following electrical potential distribution across the length of the cylinder.

$$\phi(z) = \phi_0 \left(1 - \frac{1}{l} z\right) \tag{3.6}$$

Enforcing the law of conservation of electrical charge allows us to homogenize the continuous fiber + piezoresistive matrix system. Conservation of charge dictates that the sum of the currents flowing through the individual components of the inhomogeneous system must equal the total current flowing through the homogenized system. This can be expressed mathematically as

$$I^c_{axial} = I^f_{axial} + I^m_{axial} \tag{3.7}$$

where I^c_{axial} is the current that flows through the homogenized system in the axial direction, while I^f_{axial} and I^m_{axial} are the currents associated with the fiber and the matrix, respectively. In general, the electrical current I can be found by integrating the current density distribution vector $\mathbf{J}$ over an area as follows:

$$I = \int_A \mathbf{J} \cdot \mathbf{n} \, \mathrm{d}A \tag{3.8}$$

where $\mathbf{n}$ is an outward-pointing normal vector. As mentioned before, the current density $\mathbf{J}$ can be calculated from the gradient of the potential. For instance, the current density distribution of the matrix phase in the inhomogeneous system is found as follows.

$$\mathbf{J}^m = -\frac{1}{\rho^m}\nabla\phi = -\frac{1}{\rho^m}\begin{Bmatrix} 0 \\ 0 \\ \frac{\partial\phi(z)}{\partial z} \end{Bmatrix} = \frac{\phi_0}{l\rho^m}\begin{Bmatrix} 0 \\ 0 \\ 1 \end{Bmatrix}. \tag{3.9}$$

Therefore, the current flowing through the matrix is

$$I^m_{axial} = \frac{\phi_0}{l\rho^m}\int_0^{2\pi}\int_a^b r \, \mathrm{d}r \, \mathrm{d}\theta = \frac{\phi_0}{l\rho^m}\boldsymbol{\pi}\left(b^2 - a^2\right). \tag{3.10}$$

The current flowing through the fiber phase can be found in a similar manner.

$$I^f_{axial} = \frac{\phi_0}{l\rho^f}\int_0^{2\pi}\int_0^a r \, \mathrm{d}r \, \mathrm{d}\theta = \frac{\phi_0}{l\rho^f}\boldsymbol{\pi}a^2 \tag{3.11}$$

Looking back at equation (3.7), we need to find the electrical current flowing through the hypothetical homogeneous cylindrical system, such that the system has a radius of b and an electrical resistivity of ρ^c_1 that gives rise to the same electrical response as the inhomogeneous

composite. Similarly to equations (3.9) and (3.10), the current in the homogenized composite is

$$I^c_{axial} = \frac{\phi_0}{l\rho^c_1}\int_0^{2\pi}\int_0^b r\,\mathrm{d}r\,\mathrm{d}\theta = \frac{\phi_0}{l\rho^c_1}\pi b^2. \tag{3.12}$$

From equations (3.7), (3.10), (3.11), and (3.12), we end up with the following expression.

$$\frac{\phi_0}{l\rho^c_1}\pi b^2 = \frac{\phi_0}{l\rho^f}\pi a^2 + \frac{\phi_0}{l\rho^m}\pi\left(b^2 - a^2\right) \tag{3.13}$$

As in reference [100], the rule of mixtures for the axial conductivity of the fiber-matrix system may be obtained by eliminating like terms on both sides of equation (3.13), then dividing the resulting equation by b^2. This is because the fiber volume fraction is defined as $V_f = a^2/b^2$. However, by rearranging equation (3.13), we are able to describe the resistivity of a homogenized cylindrical fiber-reinforced composite—the effective axial resistivity—as a function the constituents properties and dimensions. The resulting expression is shown in equation (3.14).

$$\rho^c_1 = \frac{b^2\rho^f\rho^m}{\rho^m a^2 + \rho^f\left(b^2 - a^2\right)} \tag{3.14}$$

In light of equation (3.14), the resistivity change of a continuous fiber enveloped by a piezoresistive matrix that undergoes a longitudinal deformation can be found by taking the difference between the effective resistivity before and after the deformation, as shown in equation (3.15).

$$\Delta\rho^c_1 = \frac{b_d^2\,\rho^f_d\,\rho^m_d}{\rho^m_d a_d^2 + \rho^f_d\left(b_d^2 - a_d^2\right)} - \frac{b^2\,\rho^f_0\,\rho^m_0}{\rho^m_0 a^2 + \rho^f_0\left(b^2 - a^2\right)} \tag{3.15}$$

In equation (3.15), the subscripts of 0 and d denote the pre- and post-deformation states of the composite, respectively. Moreover, a and b represent the pre-deformed radii of the fiber and the entire assembly, respectively, while ρ^f_0 and ρ^m_0 are the pre-deformed resistivities of the fiber and the matrix, respectively, which are constituents' electrical properties.

For the case of axial piezoresistivity, we need to express $\Delta\rho^c_1$, shown in equation (3.15), solely in terms of the axial strain of the homogenized composite, ε^c_{zz}. To do so, the radii of the deformed fiber and the composite (that is, a_d and b_d) must be first expressed in terms of ε^c_{zz}, which can be done by considering the CCA elastically. The elastic constitutive relations

for a cylinder-shaped fiber-reinforced composite subjected to uniaxial stress can be expressed as follows.

$$\varepsilon_f = S_f \sigma_f \tag{3.16a}$$

$$\varepsilon_m = S_m \sigma_m \tag{3.16b}$$

Above, σ and ε denote the stress and the strain column vectors, respectively, in Voigt notation, which are expanded for the case of uniaxial stress as shown below.

$$\sigma = \begin{Bmatrix} 0 & 0 & \sigma_{zz} & 0 & 0 & 0 \end{Bmatrix}^T \tag{3.17a}$$

$$\varepsilon = \begin{Bmatrix} \varepsilon_{rr} & \varepsilon_{\theta\theta} & \varepsilon_{zz} & 2\varepsilon_{\theta z} & 2\varepsilon_{rz} & 2\varepsilon_{r\theta} \end{Bmatrix}^T \tag{3.17b}$$

Note that the subscript and superscript of m and f can be utilized with equations (3.17) in order to construct the elastic constitutive relations of the matrix and the fiber individually. In the constitutive relations expressed in equations (3.16), the compliance matrices for a transversely isotropic fiber and an isotropic matrix are shown below.

$$S_f = \begin{bmatrix} s_{11}^f & s_{12}^f & s_{13}^f & 0 & 0 & 0 \\ s_{12}^f & s_{11}^f & s_{13}^f & 0 & 0 & 0 \\ s_{13}^f & s_{13}^f & s_{33}^f & 0 & 0 & 0 \\ 0 & 0 & 0 & s_{44}^f & 0 & 0 \\ 0 & 0 & 0 & 0 & s_{44}^f & 0 \\ 0 & 0 & 0 & 0 & 0 & 2\left(s_{11}^f - s_{12}^f\right) \end{bmatrix} \tag{3.18a}$$

$$S_m = \begin{bmatrix} s_{11}^m & s_{12}^m & s_{12}^m & 0 & 0 & 0 \\ s_{12}^m & s_{11}^m & s_{12}^m & 0 & 0 & 0 \\ s_{12}^m & s_{12}^m & s_{11}^m & 0 & 0 & 0 \\ 0 & 0 & 0 & 2\left(s_{11}^m - s_{12}^m\right) & 0 & 0 \\ 0 & 0 & 0 & 0 & 2\left(s_{11}^m - s_{12}^m\right) & 0 \\ 0 & 0 & 0 & 0 & 0 & 2\left(s_{11}^m - s_{12}^m\right) \end{bmatrix} \tag{3.18b}$$

Thus, via the elastic constitutive relations, the strains in the fiber and the matrix are as follows.

$$\varepsilon_f = \sigma_{zz}^f \begin{Bmatrix} s_{13}^f & s_{13}^f & s_{33}^f & 0 & 0 & 0 \end{Bmatrix}^T \tag{3.19a}$$

$$\varepsilon_m = \sigma_{zz}^m \begin{Bmatrix} s_{12}^m & s_{12}^m & s_{11}^m & 0 & 0 & 0 \end{Bmatrix}^T \tag{3.19b}$$

Using these relations, it is possible to describe the radial and angular strains of the constituents in terms of their axial strains. For the fiber phase, since $\varepsilon_{zz}^f = s_{33}^f \sigma_{zz}^f \neq 0$, then, $\sigma_{zz}^f = \varepsilon_{zz}^f / s_{33}^f$, which leads to the following radial and angular strains in the fiber.

$$\varepsilon_{rr}^f = s_{13}^f \sigma_{zz}^f = \frac{s_{13}^f}{s_{33}^f} \varepsilon_{zz}^f = \varepsilon_{\theta\theta}^f \tag{3.20}$$

For the matrix phase, since $\varepsilon_{zz}^m = s_{11}^m \sigma_{zz}^m \neq 0$, then, $\sigma_{zz}^m = \varepsilon_{zz}^m / s_{11}^m$, leads to the following radial strain in the matrix

$$\varepsilon_{rr}^m = s_{12}^m \sigma_{zz}^m = \frac{s_{12}^m}{s_{11}^m} \varepsilon_{zz}^m, \tag{3.21}$$

which equals $\varepsilon_{\theta\theta}^m$ for the isotropic matrix. Taking advantage of the continuity condition for axial deformation in the CCA elastic model, $U_z^f(a) = U_z^m(a)$ where U_z is the displacement in the axial direction, the fiber and matrix displacements at the interface are equal. As a result, the homogenized composite undergoes the same amount of axial strain as the matrix and fiber individually. That is,

$$\varepsilon_{zz}^f = \varepsilon_{zz}^m = \varepsilon_{zz}^c. \tag{3.22}$$

From the above equations, we are able to express the deformed radius of the fiber, a_d, and the deformed thickness of the matrix, t_d^m, in terms of ε_{zz}^c and the components of their associated compliance matrices, s_{ij}, as follows

$$a_d = a\left(1 + \varepsilon_{rr}^f\right) = a\left(1 + \frac{s_{13}^f}{s_{33}^f} \varepsilon_{zz}^c\right) \tag{3.23}$$

$$t_d^m = t^m\left(1 + \varepsilon_{rr}^m\right) = t^m\left(1 + \frac{s_{12}^m}{s_{11}^m} \varepsilon_{zz}^c\right) \tag{3.24}$$

where t^m represents the thickness of the undeformed matrix (i.e., $t^m = b - a$). Therefore, by simply adding the radius of the deformed fiber, a_d, found via equation (3.23) to the thickness of the deformed matrix, t_d^m, obtained by equation (3.24), we can find the overall radius of the deformed composite b_d in terms of the axial strain of the homogenized composite.

Returning to equation (3.15), we also need to consider the effect of strain on the electrical properties of the CCA, ρ_d^f and ρ_d^m. We assume that the piezoresistive effect in a continuous fiber is very small (i.e., $\Delta\rho^f \approx 0$ such that $\rho_d^f \approx \rho_0^f$). The change in resistivity of the modified matrix, however, is significant and must be considered. To calculate the resistivity change of the nanofiller-modified matrix, the relation developed by Koo and Tallman [113], which describes the change in resistivity of the nanofiller modified matrix as a function of strains, is implemented. This can be expressed mathematically as shown in equation (3.25). Again, it is emphasized that this resistivity-strain relation was experimentally validated in the original work by Koo and Tallman [113].

$$\Delta\rho = \kappa\left(\varepsilon_{11} + \varepsilon_{22} + \varepsilon_{33}\right) + \left(\Pi_1 + \Pi_2\right)\left(\varepsilon_{11}^2 + \varepsilon_{22}^2 + \varepsilon_{33}^2\right) + 2\Pi_1\left(\varepsilon_{11}\varepsilon_{22} + \varepsilon_{33}\varepsilon_{11} + \varepsilon_{22}\varepsilon_{33}\right) + 2\Pi_2\left(\varepsilon_{12}^2 + \varepsilon_{31}^2 + \varepsilon_{23}^2\right) \quad (3.25)$$

In this equation, κ, Π_1, and Π_2 are experimentally determined 'piezoresistive constants' (i.e., similar to elastic constants). Note that equation (3.25) was originally developed in Cartesian coordinates; however, by going back to its original tensorial form and using coordinate transformation tensor relations, it can easily be shown that this relation is also valid for any orthogonal coordinate system. Therefore, for our case, since we use the cylindrical coordinate system, subscripts 1, 2, and 3 in equation (3.25) refer to r, θ, and z directions, respectively. It is emphasized here that the focus of this work is on the homogenization of a continuous fiber + piezoresistive matrix system, rather than the development of a new piezoresistivity model for nanofiller-modified polymers without a continuous fiber reinforcement phase. Moreover, the relation developed by Koo and Tallman [113] is based on fitting a general tensorial-based strain-resistivity model to experimental data. These experiments involve specimens with various degrees of nanoparticle agglomeration. As a result, this piezoresistivity model necessarily accounts for variations in nanoparticle dispersion. That is, since it is calibrated

to real macroscale data, the model intrinsically takes into consideration features such as agglomeration, which are routinely observed in real material systems. Interested readers are directed to the original work by Koo and Tallman [113] for more details on the derivation of equation (3.25) and the experimental determination of the piezoresistive constants in this equation.

Returning to the task at hand, by applying equation (3.25) to the matrix, we can determine the change in the matrix's resistivity, $\Delta\rho^m$. Then, we take the obtained expression of the change in the matrix's resistivity and add it to the matrix's undeformed resistivity, ρ_0^m, in order to determine the resistivity of the deformed matrix, ρ_d^m (i.e., $\rho_d^m = \Delta\rho^m + \rho_0^m$). Next, we plug the expression obtained for ρ_d^m and the value of ρ_d^f (recall that we assume $\rho_d^f = \rho_0^f$) into equation (3.15) while expressing the deformed radii as functions of the axial strain and the undeformed radii, following equations (3.23) and (3.24). This allows us to obtain a formula that represents the change in the axial resistivity of the homogenized composite as a function of the axial strain and the elastic and electrical properties of the constituents, which can be mathematically expressed as follows in equation (3.26).

$$\Delta\rho_1^c\left(\varepsilon_{zz}^c\right) = \frac{b_d^2\rho_0^f\left(\rho_0^m+\alpha\right)}{\rho_0^f\left(b_d^2-a_d^2\right)+\left(\rho_0^m+\alpha\right)a_d^2} - \frac{b^2\rho_0^f\rho_0^m}{\rho_0^f\left(b^2-a^2\right)+\rho_0^m a^2} = \rho_{1d}^c - \rho_{10}^c \tag{3.26a}$$

Above, the subscript 1 followed by d and the subscript 1 followed by 0 in the right-most part of the equation (3.26a) refer to the axial resistivity after and before deformation, respectively, while α is shown below.

$$\alpha = 2\Pi_1\varepsilon_{rr}^m\left(\varepsilon_{rr}^m+\varepsilon_{zz}^c\right) + \left(\Pi_1+\Pi_2\right)\left[2\left(\varepsilon_{rr}^m\right)^2+\left(\varepsilon_{zz}^c\right)^2\right] + \kappa\left(\varepsilon_{zz}^c+2\varepsilon_{rr}^m\right) \tag{3.26b}$$

Note that both the radial strain of the matrix ε_{rr}^m and the thickness of the deformed matrix b_d can be expressed in terms of the axial strain of the homogenized system ε_{zz}^c as seen earlier in equations (3.20) to (3.24). Thus, equation (3.26) describes the piezoresistive effect of a fiber-reinforced nanofiller-modified epoxy in the axial direction as a function of the axial strain.

3.3 Transverse Piezoresistivity

In this subsection, we consider the change in resistivity in the transverse direction due to axial deformations. Again, we seek to derive a homogenized electrical CCA model for this effect. To study the piezoresistive effect in the transverse direction, we treat the potential of the domain as a function of r and θ; that is, $\phi = \phi(r, \theta)$ such that the governing equation representing steady-state electrical diffusion in the transverse direction of a cylinder, which is derived from equation (3.1), is as follows in equation (3.27).

$$\frac{1}{\rho_r}\frac{\partial^2\phi}{\partial r^2} + \frac{1}{\rho_\theta}\left(\frac{1}{r^2}\frac{\partial^2\phi}{\partial\theta^2} + \frac{1}{r}\frac{\partial\phi}{\partial r}\right) = 0 \tag{3.27}$$

Next, we find the solution to equation (3.27) for an electrically transversely isotropic composite, where the resistivities in the radial and angular directions are equal as $\rho_r^c = \rho_\theta^c = \rho_2^c$. For the case of concentric cylinders, equation (3.27) has the following solution as shown by Heider et al. [100].

$$\phi^f = (Ar + \frac{B}{r})\cos\theta, \quad \text{for } 0 \le r \le a \tag{3.28a}$$

$$\phi^m = (Cr + \frac{D}{r})\cos\theta, \quad \text{for } a \le r \le b \tag{3.28b}$$

Above, A, B, C, and D are again constants of integration, which can be found by solving the boundary value problem. Since $\phi^f(r = 0)$ must have a finite value, the constant B has to be zero. To find the remaining three constants in equations (3.28), one boundary condition and two continuity conditions are imposed. The following Neumann boundary condition is imposed on the system, which is the application of a uniform external electric field E_{ext} in the transverse direction at a sufficiently large distance, as shown in Figure 3.3.

$$\mathbf{E}^m = -\nabla\phi^m(b,\theta) = \left\{\begin{array}{l} E_r^m = -\frac{\partial}{\partial r}\phi^m(r,\theta) \\ E_\theta^m = -\frac{1}{r}\frac{\partial}{\partial\theta}\phi^m(r,\theta) \end{array}\right\}_{r=b} = \left\{\begin{array}{l} E_{ext}\cos\theta \\ E_{ext}\sin\theta \end{array}\right\} \tag{3.29}$$

Consider the first component of the electric field vector, $E_r^m = E_{ext}\cos\theta$, such that the potential at $r = b$ can be found by integrating it. This leads to

$$\phi^m(b,\theta) = -b\,E_{ext}\cos\theta. \tag{3.30}$$

To establish the electrical continuity condition, the potential and the current density distribution at the fiber-to-matrix interface (i.e., at $r = a$) must be the same. These continuity conditions can be stated mathematically as follows.

$$\phi^f(a,\theta) = \phi^m(a,\theta) \tag{3.31}$$

$$\mathbf{J}^f(a,\theta) = \mathbf{J}^m(a,\theta) \tag{3.32}$$

Since the current density $\mathbf{J}$ is related to the electric field $\mathbf{E}$ by $\mathbf{J} = \frac{1}{\rho}\mathbf{E}$ where $\mathbf{E}$ is found by taking the gradient of the potential (i.e., $\mathbf{E} = -\nabla\phi$), we can go further by representing the vectors in equation (3.32) with their components as

$$\frac{1}{\rho^f}\left\{\frac{\partial\phi^f}{\partial r} \quad \frac{1}{r}\frac{\partial\phi^f}{\partial\theta}\right\}^T_{r=a} = \frac{1}{\rho^m}\left\{\frac{\partial\phi^m}{\partial r} \quad \frac{1}{r}\frac{\partial\phi^m}{\partial\theta}\right\}^T_{r=a}. \tag{3.33}$$

By considering the first vector component in equation (3.33), which is

$$\frac{1}{\rho^f}\left(\frac{\partial\phi^f(r,\theta)}{\partial r}\right)_{r=a} = \frac{1}{\rho^m}\left(\frac{\partial\phi^m(r,\theta)}{\partial r}\right)_{r=a} \tag{3.34}$$

along with equations (3.30) and (3.31), we have three unknowns with three equations and thus can find the integration constants A, C, and D in equations (3.28) as follows. First, by imposing the Neumann boundary conditions presented in equation (3.30) on the potential in the matrix phase, which has the assumed form illustrated in equation (3.28b), the following expression is obtained.

$$b\,C + \frac{1}{b}D = -E_{ext}\,b \tag{3.35}$$

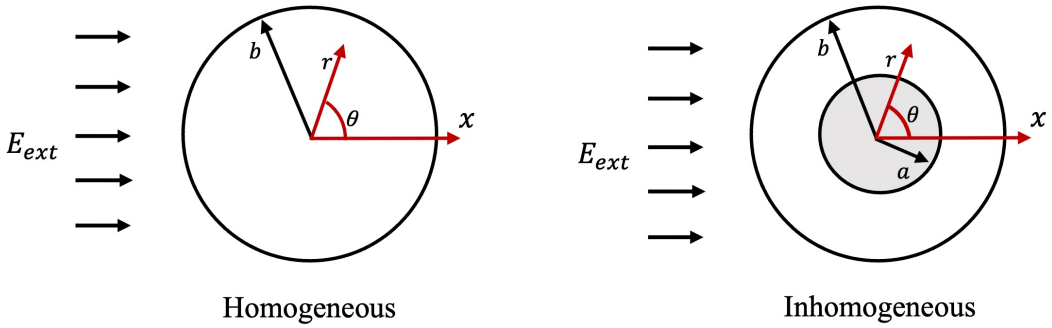

Figure 3.3. The Neumann boundary conditions are imposed on the inhomogeneous system as well as the homogeneous system by introducing external transverse electric fields at a sufficiently large distance from both systems.

Next, by utilizing the assumed solutions of the potentials in the constituents, the continuity conditions in equations (3.31) and (3.34) give us the following relations.

$$a\,A - a\,C - \frac{1}{a}D = 0 \tag{3.36}$$

$$\frac{1}{\rho^f}A - \frac{1}{\rho^m}C + \frac{1}{a^2\rho^m}D = 0 \tag{3.37}$$

Equations (3.35)–(3.37) can then be solved simultaneously to find A, C, and D.

To electrically homogenize the system in the transverse direction and determine the effective transverse electrical resistivity of the composite, we will assume that the volumetric average of current density in the homogenized composite $\bar{\mathbf{J}}^c$ is equal to the sum of the volumetric average of current densities within the components of the inhomogeneous composite. That is,

$$\bar{\mathbf{J}}^c = \bar{\mathbf{J}}^f + \bar{\mathbf{J}}^m \tag{3.38}$$

where the bar accents denote volumetric averages. Equation (3.38) can be expressed in integral form as follows.

$$\frac{1}{V_c}\int_{V_c}\mathbf{J}^c\,\mathrm{d}V_c = \frac{1}{V_f}\int_{V_f}\mathbf{J}^f\,\mathrm{d}V_f + \frac{1}{V_m}\int_{V_m}\mathbf{J}^m\,\mathrm{d}V_m \tag{3.39}$$

In the above equation, V_c, V_f, and V_m represent the volumes of the homogenized cylinder, fiber, and matrix, respectively. Note that J_x is the current flux in the x direction, which is the same direction as the direction of the external electric field E_{ext} (see Figure 3.3). The component of $\mathbf{J}$ in the x direction using the components of $\mathbf{J}$ in the polar coordinate system is $J_x = J_r\cos\theta - J_\theta\sin\theta$. The volumetric average of current densities in the x-direction for the homogeneous composite, the fiber, and the matrix are as follows.

$$\bar{J}_x^c = \frac{1}{V_c}\int_{V_c}J_x^c\,\mathrm{d}V_c = \frac{1}{\pi b^2 l}\int_0^l\int_0^{2\pi}\int_0^b\left(J_r^c\cos\theta - J_\theta^c\sin\theta\right)r\,\mathrm{d}r\,\mathrm{d}\theta\,\mathrm{d}z \tag{3.40a}$$

$$\bar{J}_x^f = \frac{1}{V_f}\int_{V_f}J_x^f\,\mathrm{d}V_f = \frac{1}{\pi a^2 l}\int_0^l\int_0^{2\pi}\int_0^a\left(J_r^f\cos\theta - J_\theta^f\sin\theta\right)r\,\mathrm{d}r\,\mathrm{d}\theta\,\mathrm{d}z \tag{3.40b}$$

$$\bar{J}_x^m = \frac{1}{V_m}\int_{V_m}J_x^m\,\mathrm{d}V_m = \frac{1}{\pi\left(b^2-a^2\right)l}\int_0^l\int_0^{2\pi}\int_a^b\left(J_r^m\cos\theta - J_\theta^m\sin\theta\right)r\,\mathrm{d}r\,\mathrm{d}\theta\,\mathrm{d}z \tag{3.40c}$$

The polar components of the current density distribution of the fiber and the matrix in equations (3.40) are derived from their associated electric fields. These electric fields are found by calculating the gradient of electric potentials, ϕ^f and ϕ^m. In other words, we use the following mathematical formula to calculate the electric field $\mathbf{E}$ and, as a result, the current density distribution $\mathbf{J}$.

$$\mathbf{J} = \frac{1}{\rho}\mathbf{E} = -\frac{1}{\rho}\nabla\phi = -\frac{1}{\rho}\left\{\frac{\partial\phi}{\partial r}\quad \frac{1}{r}\frac{\partial\phi}{\partial\theta}\right\}^T. \tag{3.41}$$

Equation (3.41) is applied to the fiber and matrix, as well as to the homogenized composite in order to enforce equations (3.38) through (3.40).

The current density distribution of the homogenized composite, $\mathbf{J}^c$, has not yet been established. For this, we use a similar approach. That is, we assume a solution to equation (3.27) as shown in equation (3.42), impose Neumann boundary conditions to obtain

the integration constants, and then use equation (3.41) to find the current density of the composite.

$$\phi^c = \left(A_c\, r + \tfrac{1}{r} B_c\right) \cos\theta, \quad \text{for } 0 \le r \le b, \tag{3.42}$$

Above, A_c and B_c are constants of integration. As with fiber, B_c must be zero in order for ϕ^c not to go to infinity as $r \to 0$. By imposing the same Neumann boundary conditions as used in equation (3.29), it can be found that $A_c = -E_{ext}$ and from equations (3.41) and (3.42), the current density distribution in the homogenized system is

$$\mathbf{J}^c = \frac{1}{\rho_2^c} E_{ext} \begin{Bmatrix} \cos\theta \\ -\sin\theta \end{Bmatrix} \tag{3.43}$$

where ρ_2^c represents the resistivity of the homogenized system in the transverse direction.

By imposing equation (3.38) on equations (3.39) through (3.43), we end up with a mathematical expression containing the electrical properties of the fiber, the matrix, and the homogenized composite, as well as the dimensions of each constituent. Solving this expression for the resistivity of the homogenized composite gives us the following relation, which is similar to the relation found in [100], [114] representing the effective conductivity in the transverse direction.

$$\rho_2^c = \rho^m \frac{a^2\left(\rho^f - \rho^m\right) + b^2\left(\rho^f + \rho^m\right)}{a^2\left(\rho^m - \rho^f\right) + b^2\left(\rho^f + \rho^m\right)} \tag{3.44}$$

Like in the longitudinal case, the change in resistivity in the transverse direction is found by taking the difference between the pre- and post-axial deformation states,

$$\Delta\rho_2^c = \rho_{2d}^c - \rho_{20}^c, \tag{3.45}$$

where the subscripts $2d$ and 20 denote the transverse resistivity after and before axial deformations, respectively. Combining equation (3.45) with the elastic and matrix piezoresistivity relations that were described earlier in equations (3.23)–(3.25), the change in effective resis-

tivity in the transverse direction as a function of the axial strain can be found as shown in equation (3.46).

$$\Delta\rho_2^c\left(\varepsilon_{zz}^c\right) = \eta\,\frac{a_d^2\left(\rho_0^f-\eta\right)+\beta^2\left(\rho_0^f+\eta\right)}{a_d^2\left(\eta-\rho_0^f\right)+\beta^2\left(\rho_0^f+\eta\right)} - \rho_0^m\,\frac{a^2\left(\rho_0^f-\rho_0^m\right)+b^2\left(\rho_0^f+\rho_0^m\right)}{a^2\left(\rho_0^m-\rho_0^f\right)+b^2\left(\rho_0^f+\rho_0^m\right)} \tag{3.46a}$$

The terms β and η can be calculated using the following mathematical expressions.

$$\beta = a_d - (a-b)\left(\frac{s_{12}^m}{s_{11}^m}\varepsilon_{zz}^c + 1\right) \tag{3.46b}$$

$$\eta = \left\{2\Pi_1\frac{s_{12}^m}{s_{11}^m}\left(2+\frac{s_{12}^m}{s_{11}^m}\right) + (\Pi_1+\Pi_2)\left[1+2\,\frac{\left(s_{12}^m\right)^2}{\left(s_{11}^m\right)^2}\right]\right\}\left(\varepsilon_{zz}^c\right)^2 + \left[\kappa\left(1+2\,\frac{s_{12}^m}{s_{11}^m}\right)\right]\varepsilon_{zz}^c + \rho_0^m \tag{3.46c}$$

Note that the deformed radius of the fiber a_d, which was given in equation (3.23), is also a function of the axial strain of the composite ε_{zz}^c.

3.4 Results and Discussions

Next, we make use of piezoresistivity data for CNF-modified epoxy as described by Koo and Tallman [113] to validate our homogenized model. To that end, we compare the homogenized model predictions to the inhomogeneous system (i.e., the exact solution) and a simple rule of mixtures prediction. This is done for both a continuous glass fiber and a continuous carbon fiber reinforcement phase. Note also that both the CNF/epoxy and the reinforcing fibers are treated as being elastically isotropic, per references [115], [116]. In the forthcoming, the free end of the CCA assembly undergoes a uniform axial displacement resulting in strains ranging from -6 mε to 6 mε, while the other end of the cylinder is axially held but free to contract or expand. radially.

The mechanical and electrical properties of the constituents used in this manuscript are outlined in Table 3.1. The matrix is epoxy modified with 1 wt.% CNFs, and the piezoresistive constants, which were shown in equation (3.25), are as follows: $\kappa = 4.10\,k\Omega\cdot m$, $\Pi_1 = -150\,k\Omega\cdot m$, and $\Pi_2 = 5.15\,k\Omega\cdot m$ [113]. Again, interested readers are directed to this reference for additional details on the determination of these piezoresistive constants.

Table 3.1. Elastic and electric properties of the composite's constituents, retrieved from references [113], [116]–[123].

Constituent Type	**Diameter** (μm)	E (GPa)	ν	ρ_0 (Ω·m)
CNF/Epoxy	—	2.711	0.351	10^5
Glass Fiber	15	73	0.250	40.2×10^9
Carbon Fiber	10	224	0.260	17×10^{-6}

In order to determine the accuracy of the proposed homogenized model, we will compare it with the inhomogeneous fiber + matrix system, which represents the exact solution. Finding the exact solution requires solving the boundary value problem for electrical diffusion in an inhomogeneous composite shown on the right side of Figure 3.1. In light of equation (3.1) along with equations (3.3) though (3.5), by integrating the electrical current density distribution **J**, we can find the overall electrical current in the inhomogeneous system as follows.

$$I_{axial}^{exact} = I_{axial}^{f} + I_{axial}^{m} = \frac{\phi_0}{l\rho^f}\pi a^2 + \frac{\phi_0}{l\rho^m}\pi\left(b^2 - a^2\right) \tag{3.47}$$

Here, the superscript $exact$ refers to the inhomogeneous solution. Note that the resistivity of the constituents varies with axial deformation and ϕ_0 is set to 10 V; thus, the current in the above equation is a function of axial strain. Next, Ohm's law is used to calculate the resistance of the inhomogeneous system from the applied voltage and the calculated current. From the resistance, the resistivity is calculated as shown below.

$$\rho_1^{exact} = R_{exact}\frac{A}{l} \tag{3.48}$$

l is the length of the system, which is assumed to be 100 μm for the undeformed composite, while A is the overall cross-sectional area. Equation (3.48) can therefore be used to find the axial resistivity of the inhomogeneous system for axial displacements that result in strains ranging from -6 mε to $+6$ mε. To find the change in resistivity, $\Delta\rho$, the undeformed resistivity is simply subtracted from the deformed resistivity at each strain increment.

Similar to the method used to get the exact solution of the axial piezoresistive response, we first look back at the governing equation for electrical diffusion in the transverse direction, shown in equation (3.27). Next, we use equations (3.28) to (3.37) and equation (3.41) to determine the total current density in the inhomogeneous composite, which is found by considering the average of the current densities within the constituents (i.e., the fiber and matrix phases) of the system in the x direction:

$$J_{trans}^{exact} = J_x^{avg} = \frac{1}{V}\int_V (J_x^f + J_x^m)\,\mathrm{d}V. \tag{3.49}$$

Here, V is the volume of the entire assembly, while J_x^f and J_x^m are given in equations (3.40b) and (3.40c). Using the continuum form of Ohm's law, $\mathbf{E} = \rho\mathbf{J}$, in the transverse direction, where $\mathbf{E}$ has a nonzero component only in the x-direction (i.e., E_{ext} due to the imposed Neumann boundary condition represented in Figure 3.3), we can calculate the resistivity of the inhomogeneous system as shown below.

$$\rho_2^{exact} = \frac{E_{ext}}{\frac{1}{V}\int_V (J_x^f + J_x^m)\,\mathrm{d}V} \tag{3.50}$$

Like the axial piezoresistivity solution, we will use this relation as the exact transverse piezoresistivity of the inhomogeneous composite.

In the following, we will also compare the homogenized and inhomogeneous piezoresistive responses to the rule of mixtures prediction for the piezoresistivity (inspired from the rule of mixtures for conductivity found in reference [100]), which states that

$$\Delta\rho^c = (1 - V_f)\,\Delta\rho^m + V_f\Delta\rho^f \tag{3.51}$$

where $V_f = a^2/b^2$ is the fiber volume fraction. An important distinction between the work presented here and the rule-of-mixtures approach is that the rule of mixtures results in an electrically isotropic composite, meaning that the piezoresistive effect is the same in the axial and transverse directions. The purpose of this comparison with the rule of mixtures is to test whether the rule of mixtures is applicable for predicting the electrical behavior of the continuous fiber + piezoresistive matrix systems. Furthermore, we will look at how the change in the reinforcing fiber volume fraction influences the piezoresistive effect of two types of fiber-reinforced nanocomposites: a continuous glass fiber enveloped by CNF-modified epoxy and a continuous carbon fiber enveloped by CNF-modified epoxy. These two material systems were chosen to investigate the impact of the insulating versus conducting reinforcement phases.

Glass fiber results with volume fractions of 20, 40, 60, and 80 vol.% are shown in Figures 3.4 through 3.7. A couple of noteworthy observations can be gleaned from these results. First, these results show that the proposed homogenized solution is in excellent agreement

with the exact solution for both the axial and transverse directions. Second, the results also show a significant difference between the exact solution and the rule-of-mixtures solution. Therefore, although the CCA homogenization approach resulted in a restatement of the rule of mixtures for the effective axial *conductivity* of the composite [100], the rule of mixtures is inaccurate for predicting the *piezoresistive* effect. Third, we also observe that when the volume fraction of the glass fiber increases, the differences between the axial and transverse homogenization solutions and the prediction of the directionless rule of the mixtures become more pronounced. This can be rationalized as follows: As the glass fiber volume fraction decreases, all piezoresistivity predictions converge, and the composite begins to behave as a pure CNF-modified epoxy with isotropic electrical properties. This is also why, for lower glass fiber volume fractions, the rule of mixtures provides more accurate predictions. However, because the composite is electrically anisotropic, the directionless rule of mixtures prediction becomes less accurate at higher glass fiber volume fractions.

Next, we consider a composite with conductive carbon fiber as continuous reinforcement, as shown in Figures 3.8 through 3.11. The same volume fractions are considered: 20, 40, 60, and 80 vol.% carbon fiber. Again, we can make some interesting observations from these results. First, we note that as the carbon fiber content becomes smaller and smaller, the prediction of the rule of mixtures converges with the transverse CCA homogenization model, similar to what was observed for the glass fiber results. Second, for all carbon fiber volume fractions, the resistivity change in the axial direction is very small. This is expected because the highly conductive carbon fiber dominates the electrical response along the axial direction. That is, even as the fiber stretches, changes in resistivity of the enveloping CNF/epoxy matrix are negligible compared to the highly conductive carbon fiber. However, we observe that $\Delta\rho_2^c$, which is the change in transverse resistivity, for carbon fiber composites exhibits a clear dependence on the axial strain. The explanation for this is that the current, in the case of the transverse direction, has to pass through the piezoresistive matrix before reaching the much more conductive carbon fiber.

The piezoresistive responses of the glass fiber and carbon fiber composites can also be compared, allowing us to arrive at several additional observations. First, in the case of glass fiber, the current travels predominantly through the conductive matrix (i.e., little

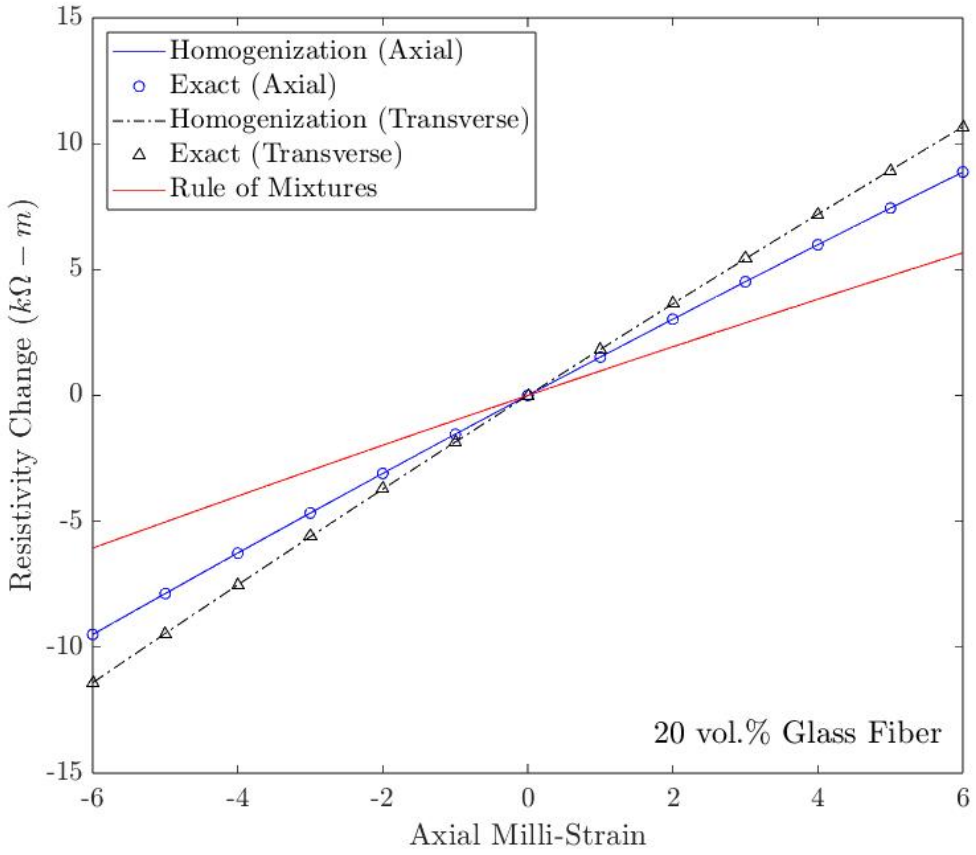

Figure 3.4. The change in the axial and transverse resistivity as a function of axial strain of CNF-modified epoxy composite with glass fiber reinforcement at 20 vol.% glass fiber based on CCA homogenization model, the exact solution, and the rule of mixtures.

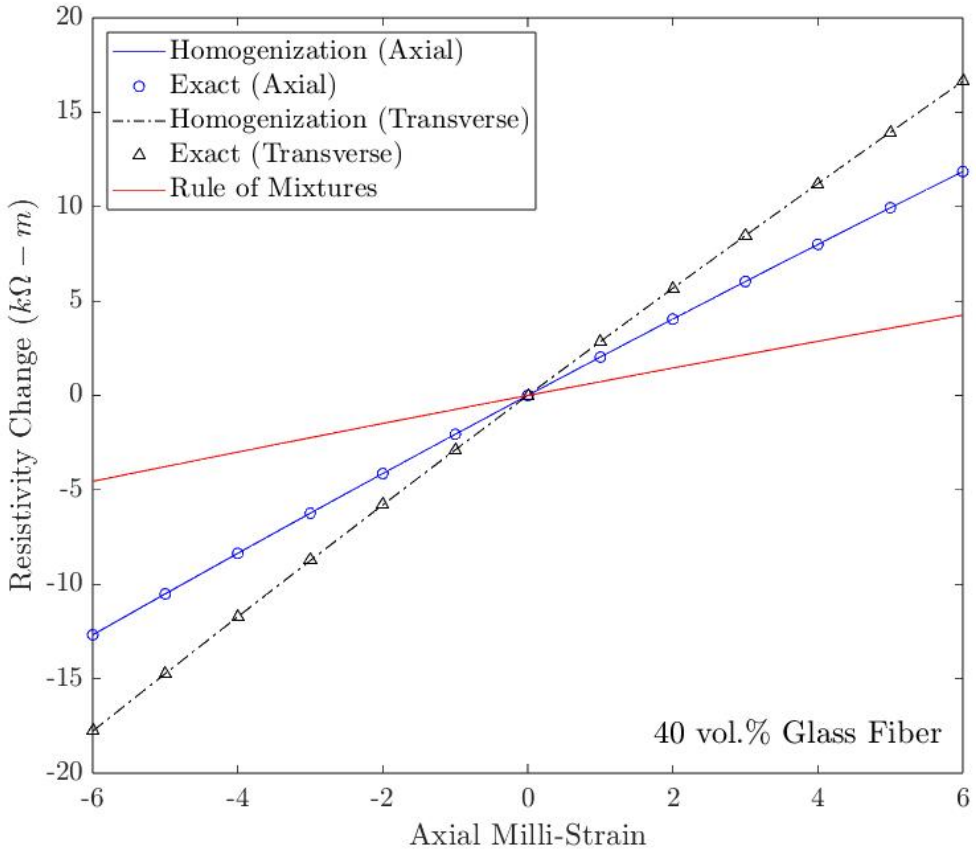

Figure 3.5. The change in the axial and transverse resistivity as a function of axial strain of CNF-modified epoxy composite with glass fiber reinforcement at 40 vol.% glass fiber based on CCA homogenization model, the exact solution, and the rule of mixtures.

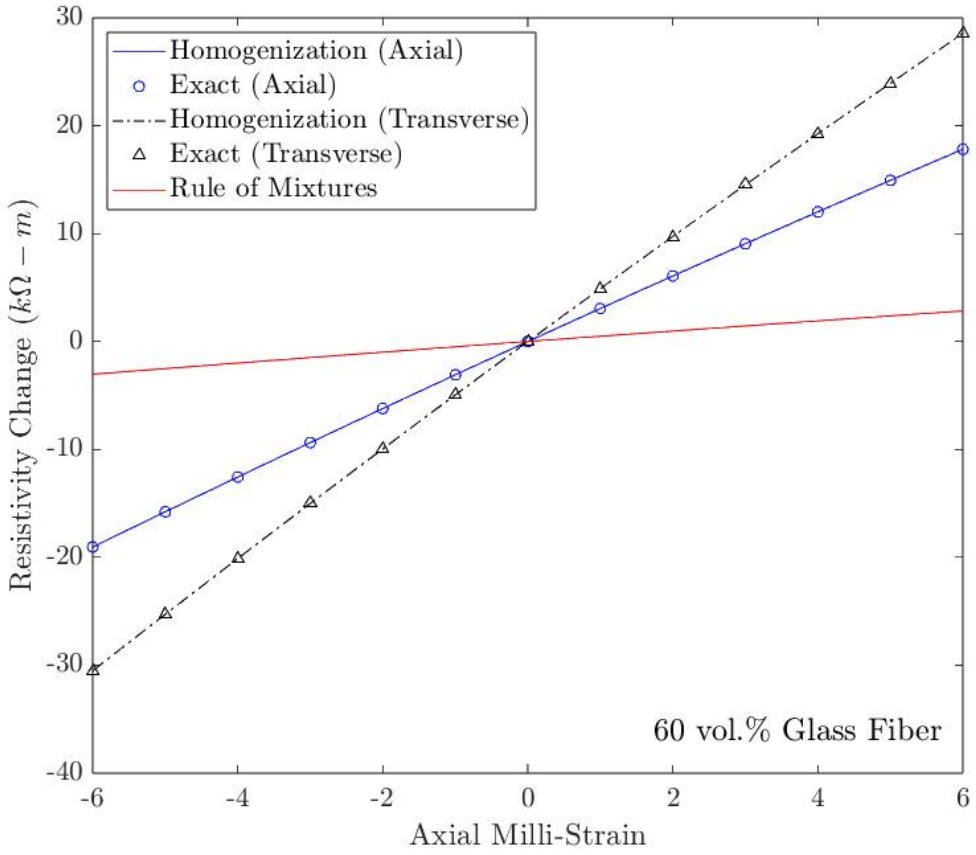

Figure 3.6. The change in the axial and transverse resistivity as a function of axial strain of CNF-modified epoxy composite with glass fiber reinforcement at 60 vol.% glass fiber based on CCA homogenization model, the exact solution, and the rule of mixtures.

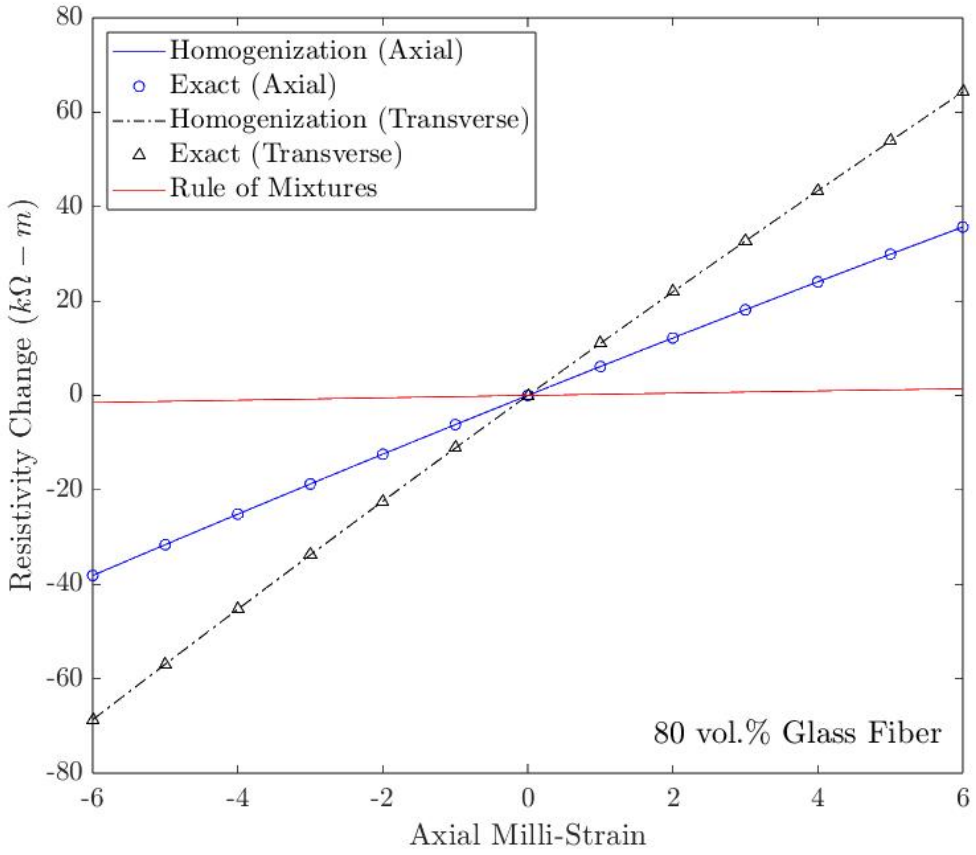

Figure 3.7. The change in the axial and transverse resistivity as a function of axial strain of CNF-modified epoxy composite with glass fiber reinforcement at 80 vol.% glass fiber based on CCA homogenization model, the exact solution, and the rule of mixtures.

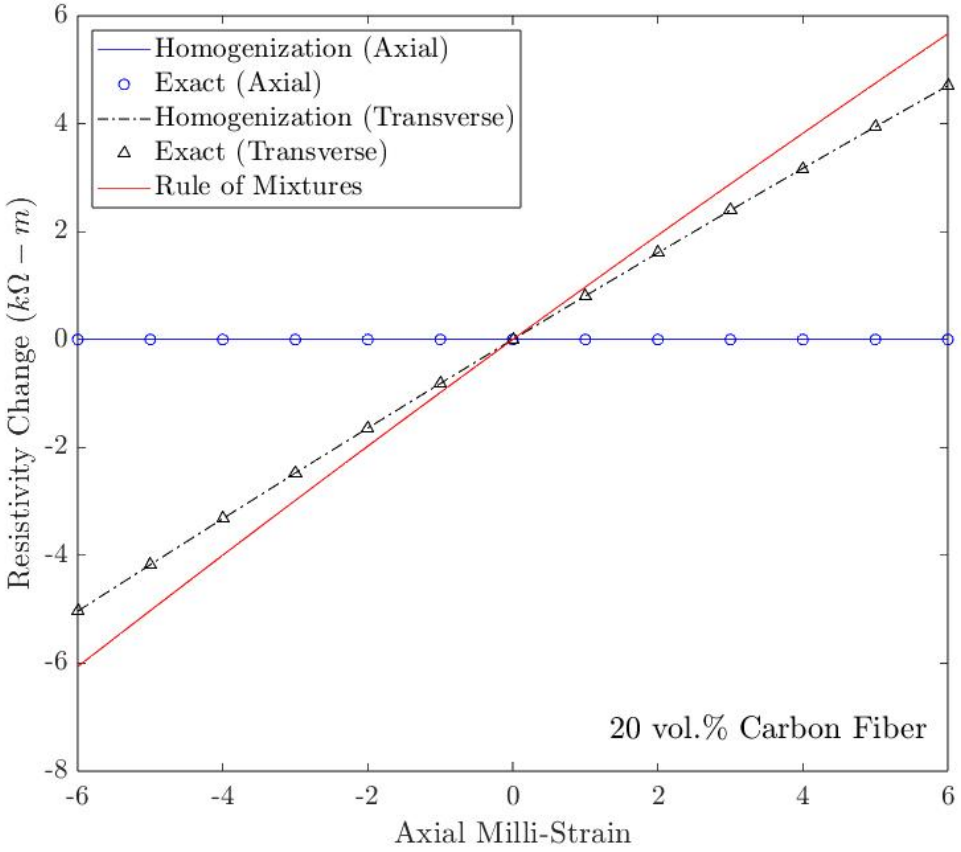

Figure 3.8. The change in the axial and transverse resistivity as a function of axial strain of CNF-modified epoxy composite with carbon fiber reinforcement at 20 vol.% carbon fiber based on CCA homogenization model, the exact solution, and the rule of mixtures.

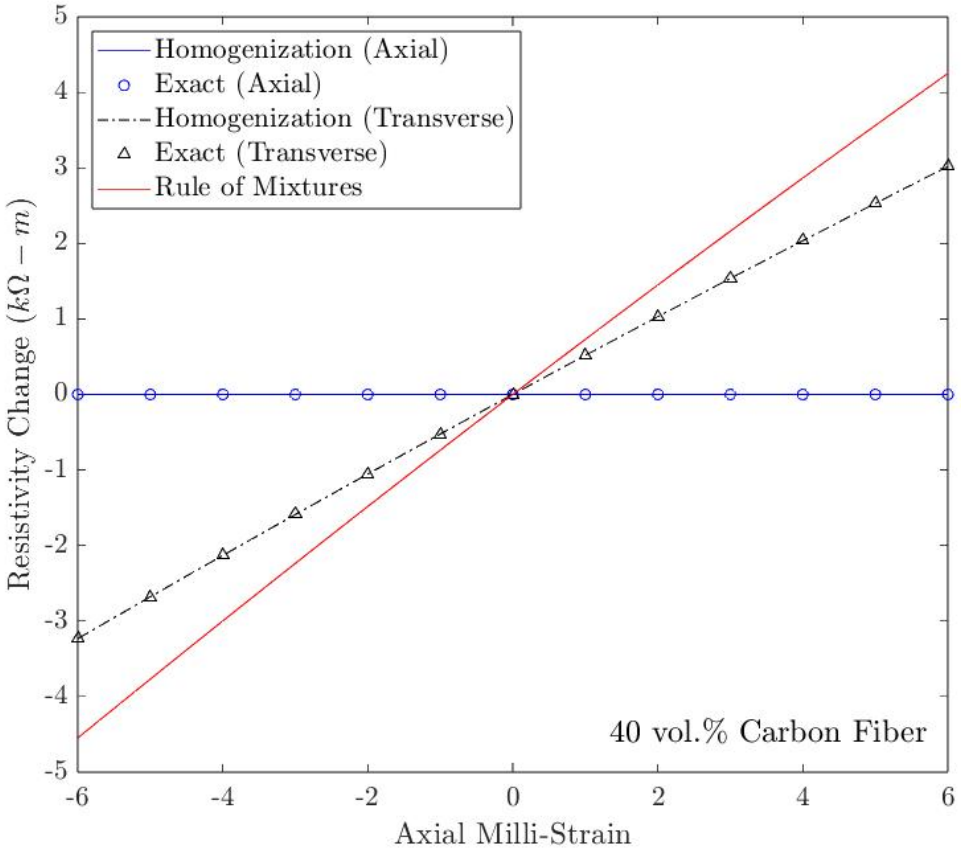

Figure 3.9. The change in the axial and transverse resistivity as a function of axial strain of CNF-modified epoxy composite with carbon fiber reinforcement at 40 vol.% carbon fiber based on CCA homogenization model, the exact solution, and the rule of mixtures.

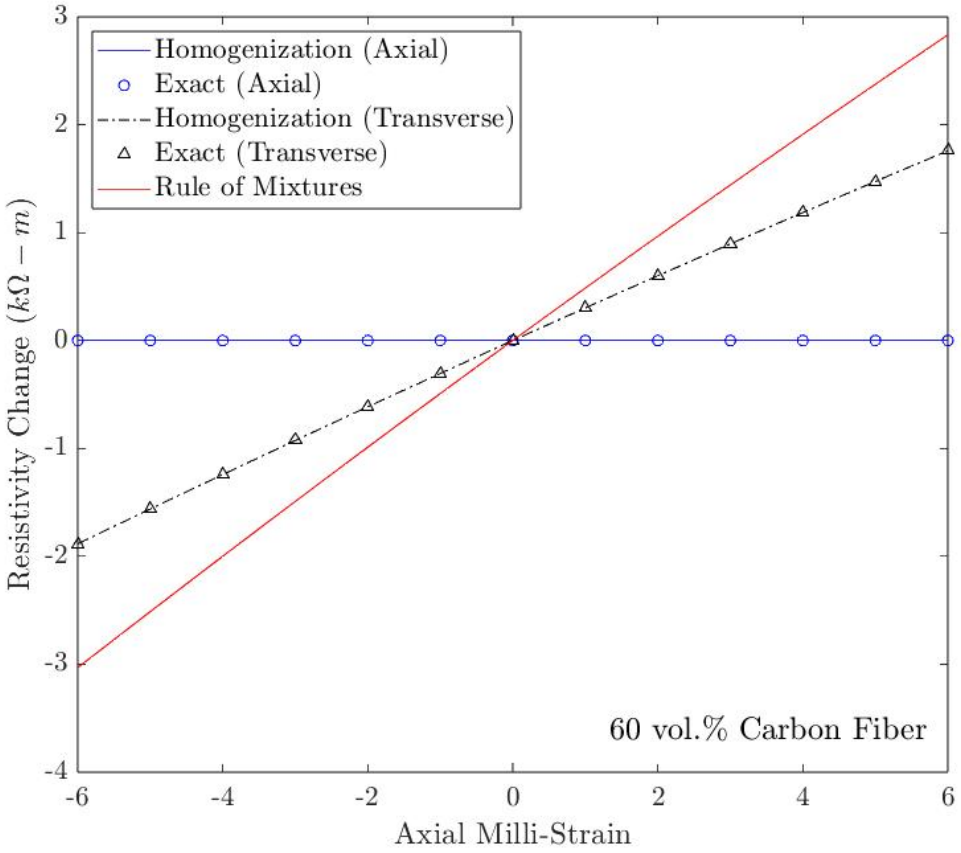

Figure 3.10. The change in the axial and transverse resistivity as a function of axial strain of CNF-modified epoxy composite with carbon fiber reinforcement at 60 vol.% carbon fiber based on CCA homogenization model, the exact solution, and the rule of mixtures.

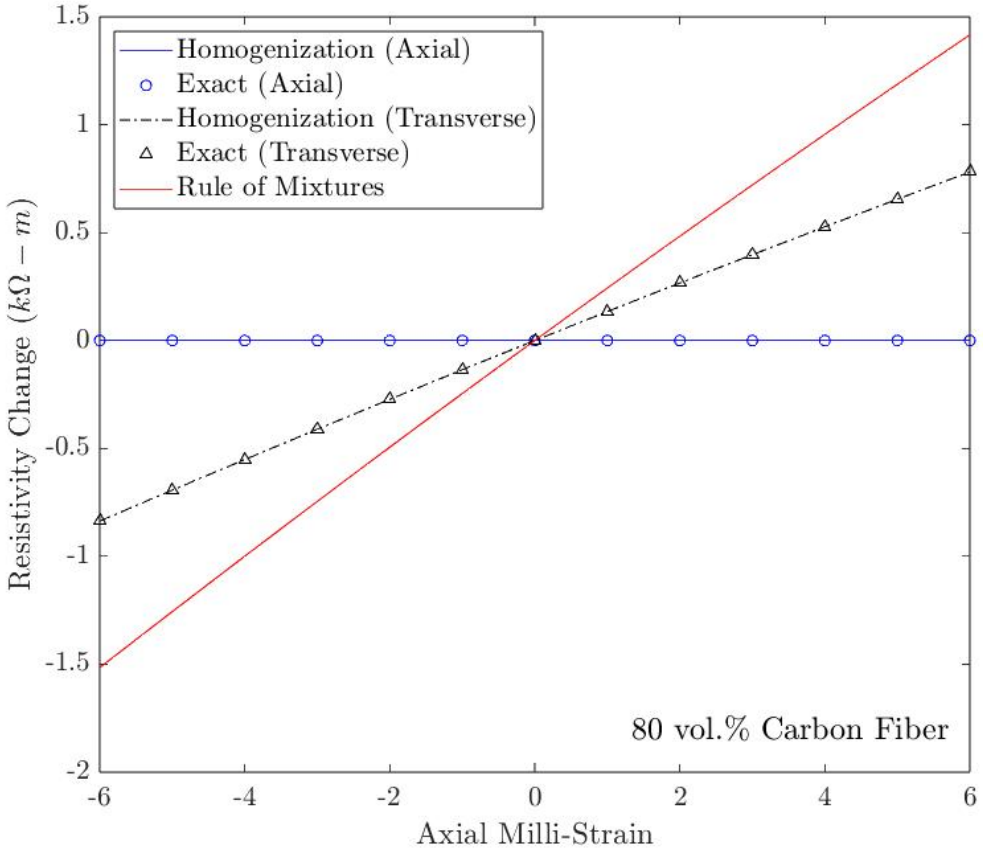

Figure 3.11. The change in the axial and transverse resistivity as a function of axial strain of CNF-modified epoxy composite with carbon fiber reinforcement at 80 vol.% carbon fiber based on CCA homogenization model, the exact solution, and the rule of mixtures.

current enters the essentially insulating glass fiber). This is why we observe a variation in $\Delta\rho_1^c$. In other words, the modified matrix is the electrically dominant phase. Second, in contrast to the glass fiber case, increasing the carbon fiber volume fraction decreases the slope of the resistivity change curves. This is again due to the dominating effect of the conductive carbon fiber. As the volume fraction of the carbon fiber increases, more and more current propagates through the carbon fiber, which also does not change the resistivity due to deformation. Thus, the effective resistivity of the composite material is increasingly insensitive to deformation and, consequently, the curves have decreasing slopes. Third, we notice that the influence of the continuous carbon fiber reinforcement on axial piezoresistivity cannot be appreciably affected by simply reducing the carbon fiber volume fraction (at least for realistic volume fractions). This is because carbon fiber, due to its extremely high conductivity compared to the surrounding matrix, essentially creates a short circuit. On the other hand, for the glass fiber case, the matrix has much higher conductivity, creating a favorable path for the current, which is the reason for having axial piezoresistivity.

4. ANALYTICAL MODELING OF RADIAL STRAIN PIEZORESISTIVITY

4.1 Introduction

This chapter presents analytical relations that describe changes in the electrical properties of fiber-reinforced nanofiller-modified composites in both longitudinal and lateral directions as a result of transverse deformations. The model derivation process will adhere to the same assumptions as discussed in Chapter 3, specifically, that the conductive matrix is elastically isotropic and the fiber's mechanical properties are transversely isotropic. Furthermore, since the composite is modeled at the level of a single fiber, an electrical CCA modeling approach is employed. This approach represents a fiber of radius a as a long cylinder encircled by a piezoresistive matrix phase modified with nanofillers to resemble tubular structures. The system consists of two concentric cylinders, namely the fiber phase and the matrix phase, which have an overall radius of b. Furthermore, it is important to note that since the CCA approach is based on a system of two concentric cylinders, the cylindrical coordinate is adopted for the mathematical analysis. Therefore, in this manuscript, the term "transverse strain" specifically denotes the strain that occurs in the radial direction, which is perpendicular to the longitudinal direction (the fiber direction). Basically, the terms radial and transverse strain/deformation may be used interchangeably throughout this dissertation.

The general steps for deriving the axial and transverse piezoresistivity relations due to transverse (radial) strains are similar to those of piezoresistivity relations due to axial strain found in Chapter 3. We begin by solving partial differential equations (PDEs) that describe axial and transverse electrical diffusion problems for a particular strain state (deformed or undeformed system). The three-dimensional governing PDE is described in equation (3.1). Note that the electric potential is the primary variable; therefore, after solving the PDE, the potential field is fully defined. Next, we impose the principle of conservation of electrical current or energy to homogenize the composite and find the effective electrical properties in the longitudinal (fiber) and lateral directions for the unstrained composite. The idea behind electrical homogenization is that we seek to develop a fictitious homogeneous cylindrical system such that the electrical properties of this homogeneous system are identical

to the heterogeneous fiber + matrix concentric cylinder system, as represented in Figure 3.1. This homogenization technique allows us to determine the effective electrical properties of the composite. Because the composite is piezoresistive, i.e., its electrical response changes when subjected to mechanical strains, we need to find the effective electrical resistivity of the system experiencing a radial deformation, then compare it with the resistivity of the unstrained system (base resistivity). This will allow us to identify resistivity changes due to transverse strain. After that, to express resistivity changes relations as functions of the applied external radial strain, we use the well-known elastic CCA model to fully describe the geometrical properties of the composite after deformation. Eventually, closed-form mathematical expressions for longitudinal and lateral piezoresistivities as functions of the applied radial strain are established.

4.2 Axial Piezoresistivity

In this section, the changes in axial electrical resistivity due to applied external radial displacement in fiber-reinforced composites are established by implementing several steps. First, we begin by deriving and solving the differential equation that characterizes the electrical diffusion in the fiber direction. Then, we apply the law of conservation of electrical energy to be able to homogenize the system and find the effective electrical properties for both strained and unstrained states. Following that, we use the Koo and Tallman resistivity-strain relation, found in equation (3.25), which allows us to predict the resistivity changes in the matrix phase as a function of the strain tensor. Finally, we can derive the closed-form axial piezoresistivity relation for fiber-reinforced composites with modified matrix by finding the difference between the effective base resistivity and the effective resistivity of the deformed composite.

4.2.1 Electrical Homogenization in The Axial Direction

In this sub-section, we solve the differential equations for steady-state electrical diffusion in the axial direction for both homogeneous and heterogeneous systems. This would allow us to fully identify the potential fields within these systems, which would then be used to impose

the conservation law, allowing us to homogenize the inhomogeneous system. Eventually, we would derive an analytical expression for the axial piezoresistivity in a fiber-reinforced nanocomposite subjected to externally applied radial displacements.

To fully describe the distribution of the electrical potential within homogeneous and heterogeneous systems in the axial direction, we need to solve the steady-state electrical diffusion problem in the fiber direction by considering the partial differential equation illustrated previously in equation (3.1). In more detail, we need to derive the differential equation for a special case of longitudinal electrical diffusion, which is accomplished by assuming that the potential distribution is only a function of z (that is, the potential ϕ only varies along the continuous fiber direction). This is achieved by imposing Dirichlet (voltage) boundary conditions at each end of the homogeneous system and the fiber + matrix system, as illustrated in Figure 3.2, and setting $\phi = \phi(z)$ accordingly. The PDE in equation (3.1) will be reduced to a second-order ordinary differential equation (ODE), as shown below in equation (4.1).

$$\frac{1}{\rho(r)} \frac{d^2\phi(z)}{dz^z} = 0 \tag{4.1}$$

It is important to mention that the above ODE cab be utilized to characterize the steady-state electrical diffusion within the homogenized system, which assumed to have a constant effective axial resistivity ρ_1^c. In this case, $\rho(r) = \rho_1^c = constant$. It can also be applied to the inhomogeneous deformed system in which the deformed piezoresistive matrix, for the radial strain case, would have a resistivity that varies across the radial direction, i.e., $\rho(r) = \rho_d^m(r)$, as we shall see later. For this reason, and for the sake of generality, the resistivity in equation (4.1) is written as a function of r, unlike the constant resistivity shown in equation (3.3) (used to obtain the axial piezoresistivity due to axial deformation) to account for situations that result in variable resistivities. However, for both the constant and variable resistivity cases, the above differential equation has the following linear general solution in z.

$$\phi^q(z) = A^q z + B^q \tag{4.2}$$

The superscript q is either replaced by m, f, or c in order to individually specify the general solution of the steady-state electrical diffusion problem in the matrix, the fiber and the homogenized composite, respectively. To obtain particular solutions, we need to identify the integration constants of the homogenized composite as well as the integration constants associated with the constituents of the heterogeneous composite. In other words, we need to find A^q and B^q. These constants can be found by setting a fixed voltage value on one side, $\phi^q(z=0)=\phi_0$, while maintaining the zero voltage condition on the other side, $\phi^q(z=l)=0$. l here is the length of the system. After imposing the aforementioned boundary conditions, we can obtain the following electrical potential distribution across the longitudinal direction of the cylindrical system.

$$\phi^q(z) = \left(1 - \frac{1}{l}z\right)\phi_0 \tag{4.3}$$

Next, we apply the law of conservation of electrical current to the fiber-matrix system in order to achieve homogeneity. This ensures that the electrical characteristics of the non-homogeneous system are equivalent to those of the homogeneous system. By applying the principle of electrical current conservation, as described in equation (3.7), to the undeformed composite, a mathematical relation can be derived that provides the resistivity of the homogenized composite or the effective resistivity. This relation can be expressed as follows.

$$\rho_{10}^c = \frac{\rho_0^f \rho_0^m}{V_f \rho_0^m + \rho_0^f (1 - V_f)} \tag{4.4}$$

The subscript 1 followed by 0 refers to the base axial resistivity of the composite (unstrained composite's resistivity). The above expression is obtained by multiplying the numerator and the denominator on the right-hand side of equation (3.14) by $1/b^2$, since the fiber volume fraction is defined as $V_f = a^2/b^2$. The full details of obtaining the effective axial resistivity relation of the composite are found in Chapter 3 (refer to equations (3.7) to (3.14)). It is important to note that equation (4.4) is only valid when the resistivities of the constituents are constant. However, as mentioned earlier, unlike the case of piezoresistivity due to axial strain, we will see that the resistivity of the matrix phase in the composite is *not* constant when subjected to an external radial strain; it varies radially. Thus, we need to again impose

the law of conservation of current for the deformed composite while, this time, considering a variable resistivity of the matrix $\rho_d^m = \rho_d^m(r)$. To do so, we go back to the mathematical form of current conservation, which is

$$I^c_{axial,d} = I^f_{axial,d} + I^m_{axial,d}. \tag{4.5}$$

Based on equation (4.5) above, the current in the deformed homogeneous composite is equal to the sum of the currents in the matrix phase and the fiber phase within the inhomogeneous system. The subscript d in equation (4.5) denotes the deformed state. The electric currents, I, for the homogeneous composite, the fiber, and the matrix are calculated, respectively, by integrating the current density distribution vector $\mathbf{J}$ over the area that is normal to the vector.

$$I^c_{axial,d} = \int_{A_c} \mathbf{J}^c_d \cdot \mathbf{n}^c_d \, \mathrm{d}A_c \tag{4.6a}$$

$$I^f_{axial,d} = \int_{A_f} \mathbf{J}^f_d \cdot \mathbf{n}^f_d \, \mathrm{d}A_f \tag{4.6b}$$

$$I^m_{axial,d} = \int_{A_m} \mathbf{J}^m_d \cdot \mathbf{n}^m_d \, \mathrm{d}A_m \tag{4.6c}$$

In the above integrations, A_c, A_f, and A_m are the cross-sectional areas of the composite, the fiber and the matrix, respectively, while $\mathbf{n}^c_d$, $\mathbf{n}^f_d$, and $\mathbf{n}^m_d$ are their corresponding outward-pointing normal vectors. The previous chapter has established a relationship between the current density vector and *phi*. This relationship can be described by equation (3.41), which states that the gradient of the potential multiplied by the negative of the conductivity, which is the reciprocal of the resistivity, is equivalent to the current density vector. Since the resistivities of the fiber and the homogenized system are still constant for the case of radial strain piezoresistivity, the derivation of their corresponding current density vectors and, as a consequence, the current flow through them is directly similar to what was illustrated in equations (3.9) through (3.12). That is, the current flow through the homogenized composite is

$$I^c_{axial,d} = \frac{\phi_0}{l\rho^c_{1d}} \boldsymbol{\pi} b_d^2, \tag{4.7}$$

whereas the current flow through the fiber phase is

$$I^{f}_{axial,d} = \frac{\phi_0}{l\rho^{f}_{d}}\pi a_d^2. \tag{4.8}$$

It is important to observe that a_d represents the radius of the fiber, while b_d represents the radius of the entire assemblage (in this case the radius of the homogenized composite) after deformation. The effective resistivity of the composite in the axial direction at a particular radial deformation state is indicated as ρ^{c}_{1d}, which is written in equation (4.7). To determine the change in axial resistivity caused by radial strain, it is necessary to solve for this value, which is assumed to be constant. Following this, the current within the matrix phase must be determined. The current density distribution of the deformed matrix phase $\mathbf{J}^{m}_{d}$ is determined initially, as outlined below.

$$\mathbf{J}^{m}_{d} = -\frac{1}{\rho^{m}_{d}(r)}\nabla\phi^{m} = -\frac{1}{\rho^{m}_{d}(r)}\begin{Bmatrix} 0 \\ 0 \\ \frac{\partial\phi^{m}(z)}{\partial z} \end{Bmatrix} = \frac{\phi_0}{l\rho^{m}_{d}(r)}\begin{Bmatrix} 0 \\ 0 \\ 1 \end{Bmatrix}. \tag{4.9}$$

From equation (4.6c), the current flow through the deformed matrix phase is

$$I^{m}_{axial,d} = \frac{\phi_0}{l}\int_0^{2\pi}\int_{a_b}^{b_b}\frac{1}{\rho^{m}_{d}(r)}\,r\,\mathrm{d}r\,\mathrm{d}\theta = \frac{2\pi\phi_0}{l}\int_{a_b}^{b_b}\frac{1}{\rho^{m}_{d}(r)}r\,\mathrm{d}r. \tag{4.10}$$

Now, we can impose the current conservation relation shown in equation (4.5) and use equations (4.7), (4.8), and (4.10) to have the following mathematical expression.

$$\frac{\phi_0}{l\rho^{c}_{1d}}\pi b_d^2 = \frac{\phi_0}{l\rho^{f}_{d}}\pi a_d^2 + \frac{2\pi\phi_0}{l}\,\omega^{m}_{\rho} \tag{4.11a}$$

The term ω^{m}_{ρ} is written above for simplicity, and it represents the integral part of equation (4.10), which is as follows.

$$\omega^{m}_{\rho} = \int_{a_b}^{b_b}\frac{1}{\rho^{m}_{d}(r)}\,r\,\mathrm{d}r \tag{4.11b}$$

By rearranging equation (4.11a) and solving it for the resistivity of the deformed homogenized composite ρ^{c}_{1d}, we can derive a mathematical expression that describes the effective resistivity

of the fiber-reinforced nanocomposite as a function of the constituent's geometrical and electrical characteristics. This expression is shown below in equation (4.12).

$$\rho_{1d}^{c} = \frac{b_d^2\,\rho_d^f}{a_d^2 + 2\,\rho_d^f\,\omega_\rho^m} \tag{4.12}$$

Taking into account equations (4.4) and (4.12), the variation in the resistivity of a continuous fiber surrounded by a piezoresistive matrix subjected to radial deformation is determined by calculating the difference in the effective resistivities before and after the deformation, as depicted in equation (4.13) below.

$$\Delta\rho_1^c = \frac{b_d^2\,\rho_d^f}{a_d^2 + 2\,\rho_d^f\,\omega_\rho^m} - \frac{\rho_0^f\rho_0^m}{V_f\rho_0^m + \rho_0^f\,(1 - V_f)} \tag{4.13}$$

Within equation (4.13), the subscripts 0 and d refer to the states before and after deformation of the composite material, correspondingly. Furthermore, a and b refer to the initial radii of the fiber and the entire structure, while ρ_0^f and ρ_0^m denote the initial resistivity values of the fiber and matrix, illustrating the electrical characteristics of these components. Also note the main difference between this relation and the one shown in equation (3.15), which was derived for constant deformed matrix resistivity. We now have ω_ρ^m, which represents the radial integration of the variable matrix conductivity, shown in equation (4.11b) above.

4.2.2 CCA Elasticity Model

Next, we will make use of the elasticity solution for the CCA model, subjected to radial deformation, so that we can express $\Delta\rho_1^c$ shown in equation (4.13) as a function of the applied radial strain only. This is accomplished by rewriting the deformed geometrical properties of the composite constituents in terms of the external radial strain. Moreover, the elasticity model will aid us in obtaining the resistivity of the matrix after deformation, $\rho_d^m(r)$, as we need to find the strain tensor within the deformed matrix in order to be able to utilize Koo and Tallman resistivity-strain relation [113], which will be discussed in the next subsection.

In summary, the following are the procedural steps that will be taken in this subsection. Initially, the mechanical equilibrium equation is derived by considering the displacements of

both cylindrical systems. In order to solve the boundary value problem (BVP) and obtain the displacement fields, specific boundary and continuity conditions are imposed. In light of the applied external radial strain, we will use displacement-strain relations to determine the strain tensors of both the fiber and the matrix. Ultimately, the deformed radii of the fiber and the composite are derived in terms of the applied radial strain.

To derive the equilibrium equation of the elastic CCA model in terms of displacements, we start by assuming the plane-strain condition, that is, the CCA model is relatively long in the z-direction such that the longitudinal strain, ε_{zz}, can be ignored. Moreover, as mentioned before, since we are dealing with a cylindrical model, it is assumed that the transverse stain is in the radial direction, that is, $\varepsilon_{22} = \varepsilon_{rr}$. Therefore, the composite is subjected to an externally applied radial strain, ε_{rr}^{ext}, as shown in Figure 4.1, where the superscript ext denotes the externally applied radial strain. Throughout our elasticity analysis, the fiber and the matrix individually are assumed to be isotropic. Their elastic constitutive relations (stress-strain relations) in the Voigt notation, as well as their strain-displacement relations, are illustrated in equations (4.14) and (4.15), respectively.

$$\sigma_q = C_q \varepsilon_q \tag{4.14a}$$

The above equation can be further expanded as follows.

$$\begin{bmatrix} \sigma_{rr}^q \\ \sigma_{\theta\theta}^q \\ \sigma_{r\theta}^q \end{bmatrix} = \begin{bmatrix} c_{11}^q & c_{12}^q & 0 \\ c_{12}^q & c_{11}^q & 0 \\ 0 & 0 & c_{66}^q \end{bmatrix} \begin{bmatrix} \varepsilon_{rr}^q \\ \varepsilon_{\theta\theta}^q \\ \varepsilon_{r\theta}^q \end{bmatrix} \tag{4.14b}$$

The stain-displacement relations are

$$\varepsilon_{rr} = \frac{\partial U_r^q}{\partial r}, \tag{4.15a}$$

$$\varepsilon_{\theta\theta} = \frac{1}{r}\frac{\partial U_\theta^q}{\partial \theta} + \frac{U_r^q}{r}, \tag{4.15b}$$

$$\varepsilon_{r\theta} = \frac{1}{2}\left(\frac{\partial U_r^q}{\partial \theta} + \frac{1}{r}\frac{\partial U_\theta^q}{\partial r} - \frac{U_\theta^q}{r}\right), \tag{4.15c}$$

where U_r is the displacement in the radial direction, and U_θ is the displacement in the circumferential direction. Moreover, the superscripts and superscripts q in the above equations can be replaced by m, f, or c to specify the plane-strain constitutive relations and strain-displacement relations for the matrix, the fiber, and the homogenized composite, respectively. However, it is worth mentioning that although the fiber and the matrix are assumed to be isotropic, the homogenized composite is considered to be elastically transversely isotropic, which also has similar plane-strain governing relations but different out-of-plane relations. As we apply the radial deformation, shown in Figure 4.1, we would have an axisymmetric plane-strain condition resulting in zero angular displacement. In other words, $U_\theta = 0$ and the radial displacement solely depends on r, namely, $U_r = U_r(r)$. Subsequently, the displacement-strain relations simplify as

$$\varepsilon_{rr} = \frac{dU_r^q(r)}{dr}, \tag{4.16a}$$

$$\varepsilon_{\theta\theta} = \frac{U_r^q(r)}{r}, \tag{4.16b}$$

$$\varepsilon_{r\theta} = \frac{1}{2}\left(\frac{\partial U_r^q(r)}{\partial \theta}\right) = 0. \tag{4.16c}$$

We aim to derive a governing equilibrium equation for the elastic CCA model in terms of displacement. This can be accomplished by substituting the strain-displacement relations found in equations (4.16) into the stress-strain relations found in equation (4.14), then substituting the obtained expressions into the stress equilibrium equations, allowing us to derive the following equilibrium equation in terms of the radial displacement, which can also be found in [124].

$$\frac{d^2U_r^q(r)}{dr^2} + \frac{1}{r}\frac{dU_r^q(r)}{dr} - \frac{U_r^q(r)}{r^2} = 0 \tag{4.17}$$

The stress equilibrium equations for plane-strain condition are presented below.

$$\frac{\partial \sigma_{rr}^q}{\partial r} + \frac{1}{r}\frac{\partial \sigma_{r\theta}^q}{\partial \theta} + \frac{\sigma_{rr}^q - \sigma_{\theta\theta}^q}{r} = 0 \tag{4.18a}$$

$$\frac{\partial \sigma_{\theta\theta}^q}{\partial \theta} + \frac{1}{r}\frac{\partial \sigma_{r\theta}^q}{\partial r} + \frac{2\sigma_{r\theta}^q}{r} = 0 \tag{4.18b}$$

To solve the ordinary differential equation (ODE) shown in equation (4.17) and find the particular solutions for the matrix and fiber phases, we need to find the general solution first and then find the particular solutions based on specific boundary and continuity conditions. As suggested by Shu and Stanciulescu [124], the derived ODE has the following general solution.

$$U_r^q(r) = A^q r + \frac{B^q}{r} \tag{4.19}$$

A^q and B^q are constants of integration. Finding their values enables us to fully describe the displacement fields within the fiber and matrix phases and, consequently, the strain fields via displacement-strain relations. Note that the value of B^f must be zero so that the radial displacement at $r = 0$ is defined. Therefore, the radial displacements of the fiber and the matrix are

$$U_r^f(r) = A^f r, \tag{4.20a}$$

$$U_r^m(r) = A^m r + \frac{B^m}{r}. \tag{4.20b}$$

From equations (4.20), we have three unknowns, which are A^f, A^m, and B^m. To obtain their values, two continuity conditions are imposed at the fiber-matrix interface, i.e., at $r = a$, and a boundary condition is imposed at the outer surface of the composite. These conditions can be expressed mathematically as shown in the following equations.

$$U_r^f(r = a) = U_r^m(r = a) \tag{4.21a}$$

$$\sigma_{rr}^f(r = a) = \sigma_{rr}^m(r = a) \tag{4.21b}$$

$$\varepsilon_{rr}^m(r = b) = \varepsilon_{rr}^{ext} \tag{4.21c}$$

The continuity conditions stated in equations (4.21a) and (4.21b) are fulfilled based on the assumption that the fiber and the matrix at the interface are perfectly bonded, and the boundary condition shown in equation (4.21c) indicates that the composite is subjected to an axisymmetric radial external strain that has a value of ε_{rr}^{ext} at the outer surface of the composite ($r = b$), as illustrated in Figure 4.1. We begin with the first displacement

continuity condition; that is, by substituting equations (4.20a) and (4.20b) into equation (4.21a), we can get the following expression.

$$aA^f = aA^m + \frac{1}{a}B^m \tag{4.22}$$

To impose the stress continuity condition in equation (4.21b), the radial stresses within the fiber and the matrix must be expressed in terms of displacements, which can be achieved by first considering the stress-strain relations in equations (4.14b), so that the radial stress is expressed in terms of strains as follows.

$$\sigma_{rr}^q = c_{11}^q \varepsilon_{rr}^q + c_{12}^q \varepsilon_{\theta\theta}^q \tag{4.23}$$

Then, via the strain-displacement relations for plane-strain condition, stated previously in equations (4.16), and the above equation, we can express the radial stress (in both the fiber and the matrix) in terms of the radial displacements, as shown below.

$$\sigma_{rr}^q = c_{11}^q \frac{dU_r^q(r)}{dr} + c_{12}^q \frac{U_r^q(r)}{r} \tag{4.24}$$

In the above equation, c_{11}^q and c_{12}^q are the components of the stiffness matrix for the fiber (if $q = f$) and the matrix (if $q = m$). Now, since we have successfully expressed the radial stress fields within the composite constituents in terms of their corresponding displacement fields, we can impose the stress continuity condition at the interface by substituting equations (4.20) into equation (4.24), then plugging the resulting expressions into equation (4.21b), so that we can obtain the following mathematical expression.

$$A^f \left(c_{11}^f + c_{12}^f\right) = A^m \left(c_{11}^m + c_{12}^m\right) + \frac{1}{a^2}\left(c_{12}^m - c_{11}^m\right) B^m \tag{4.25}$$

For simplicity, assume that $\gamma_f = \left(c_{11}^f + c_{12}^f\right)$, $\gamma_m = (c_{11}^m + c_{12}^m)$, and $\lambda_m = (c_{12}^m - c_{11}^m)$, which are constants representing the fiber and the matrix mechanical properties. Therefore, equation (4.25) is re-expressed as follows.

$$\gamma_f A^f = \gamma_m A^m + \frac{1}{a^2}\lambda_m B^m \tag{4.26}$$

We now impose the boundary condition at the outer surface of the composite by first finding the radial strain field within the matrix through equations (4.20b) and (4.16a), then substituting the obtained expression into equation (4.21c) to get the following expression.

$$A^m - \frac{1}{b^2}B^m = \varepsilon_{rr}^{ext} \tag{4.27}$$

By solving the system of three equations, which are equations (4.22), (4.26), and (4.27), we can find the values of the three integration constants, which are A^f, A^m, and B^m, in terms of the mechanical and geometrical properties of the composite constituents, as well as the applied external radial strain, ε_{rr}^{ext}. These constants can be mathematically illustrated as follows.

$$A^f = \mu\left(\lambda_m - \gamma_m\right)\varepsilon_{rr}^{ext} \tag{4.28a}$$

$$A^m = \mu\left(\lambda_m - \gamma_f\right)\varepsilon_{rr}^{ext} \tag{4.28b}$$

$$B^m = a^2\mu\left(\gamma_f - \gamma_m\right)\varepsilon_{rr}^{ext} \tag{4.28c}$$

The term μ is introduced to simplify the above expression, and it is defined as

$$\mu = \left[V_f\left(\gamma_m - \gamma_f\right) - \gamma_f + \lambda_m\right]^{-1} \tag{4.29}$$

where V_f is the fiber volume fraction. After identifying the constants A^f, A^m, and B^m, as shown in equations (4.28), we can fully describe the radial displacement fields within the fiber $U_r^f(r)$ and the matrix $U_r^m(r)$. In other words, the obtained displacement fields represent the particular solutions of the governing differential equations, presented in equation (4.17)

that state the mechanical equilibrium equations in terms of radial displacements within the fiber and the matrix.

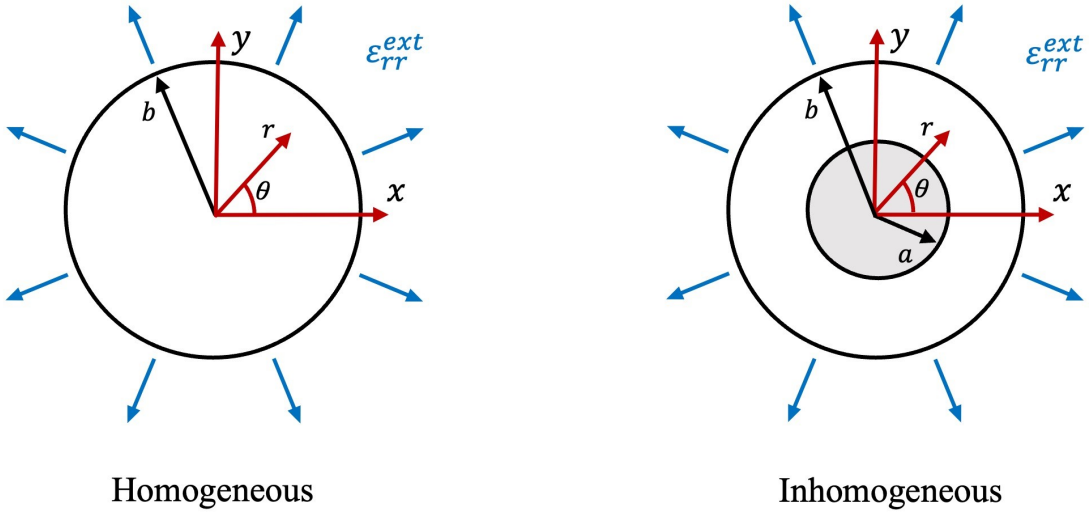

Figure 4.1. The homogeneous and inhomogeneous CCA systems subjected to externally applied radial axisymmetric strain ε_{rr}^{ext}. Note that in the inhomogeneous image, the gray inner cylinder represents the continuous fiber reinforcing phase. Our goal is to replicate the strain-induced resistivity changes of the inhomogeneous system in the homogeneous system.

Recall that our task in this subsection is to use the elasticity solution to express the deformed radius of the fiber, a_d, and the deformed radius of the composite, b_d, which appear in equation (4.13), in terms of the external radial strain, ε_{rr}^{ext}. For that to be achieved, we first need to derive the components of the fiber and matrix strain tensors, namely the radial and angular strains, using the displacement fields derived, presented in equations (4.20) through (4.29), and the strain-displacement relations in equations (4.16). The radial and angular strains of the fiber are as follows.

$$\varepsilon_{rr}^{f}(r) = \frac{d}{dr}U_r^f(r) = A^f \tag{4.30a}$$

$$\varepsilon_{\theta\theta}^{f}(r) = \frac{U_r^f(r)}{r} = A^f \tag{4.30b}$$

The radial and the angular strains within the matrix are as follows.

$$\varepsilon_{rr}^{m}(r) = \frac{d}{dr}U_{r}^{m}(r) = A^{m} - \frac{1}{r^{2}}B^{m} \tag{4.31a}$$

$$\varepsilon_{\theta\theta}^{m}(r) = \frac{U_{r}^{m}(r)}{r} = A^{m} + \frac{1}{r^{2}}B^{m} \tag{4.31b}$$

In the above equations, A^{f}, A^{m}, and B^{m}, derived previously in equations (4.28) and (4.29), are dependent on the external radial strain, ε_{rr}^{ext}. Therefore, the deformed radius of the fiber can be calculated using the following integration.

$$a_{d} = \int_{0}^{a} \left[1 + \varepsilon_{rr}^{f}(r)\right] \mathrm{d}r \tag{4.32}$$

Similarly, the deformed radius of the composite can be calculated via the following integration.

$$b_{d} = a_{d} + \int_{a}^{b} \left[1 + \varepsilon_{rr}^{m}(r)\right] \mathrm{d}r \tag{4.33}$$

The above integrals give us the geometrical properties of the composite after deformation in terms of the radial strain.

4.2.3 Resistivity-Strain Analytical Relation

Our aim here is to find individual changes in resistivity, $\Delta\rho$, of the homogenized fiber-matrix system due to radial deformations. This would allow us to calculate the resistivity values after deformations, which were mentioned in equation (4.13), and eventually obtain the piezoresistivity of the composite as a function of the radial strain. As we have assumed before in Chapter 3, the resistivity changes in the fiber are insignificant compared to the resistivity changes in the nanomodified matrix, which are triggered by the piezoresistivity effect due to the presence of nanofillers. Thus, we will assume that the resistivity of the deformed fiber is equal to its resistivity before deformations, i.e., $\rho_{d}^{f} = \rho_{0}^{f} = \rho^{f}$.

To calculate the resistivity of the matrix after deformation, we need to investigate how the resistivity of the matrix phase changes due to strain. Derived from the empirical relation between resistivity and strain of Koo and Tallman [113], which is valid for the strain

tensors defined in any orthogonal coordinate system and was previously mentioned in equation (3.25), the change in matrix resistivity due to applied external radial strain (with the assumption of plane-strain) is shown in the following equation.

$$\Delta\rho^m(r) = \kappa\left[\varepsilon^m_{rr}(r) + \varepsilon^m_{\theta\theta}(r)\right] + (\Pi_1 + \Pi_2)\left\{\left[\varepsilon^m_{rr}(r)\right]^2 + \left[\varepsilon^m_{\theta\theta}(r)\right]^2\right\} + 2\Pi_1\left[\varepsilon^m_{rr}(r)\,\varepsilon^m_{\theta\theta}(r)\right] \quad (4.34)$$

In this equation, κ, Π_1, and Π_2 are empirically obtained piezoresistive constants that are analogous to elastic constants. As we noted earlier in Chapter 3, the model developed by Koo and Tallman [113] is grounded in aligning a tensor-based strain-resistivity framework with empirical data, involving specimens that demonstrate varying degrees of nanoparticle agglomerations. Consequently, this piezoresistivity model effectively captures the variability in nanoparticle dispersion.

We should now be able to construct a closed-form analytical relation that detects the change in axial resistivity as a function of the external radial strain for fiber-reinforced nanofiller-modified composites. Initially, it is necessary to determine the resistivity values of both the matrix and the fiber following deformation. This can be accomplished using equation (4.34) to calculate the resistivity of the deformed matrix, which is $\rho^m_d = \Delta\rho^m + \rho^m_0$. However, it is important to note that the resistivity of the fiber remains constant, as previously mentioned, with $\rho^f_d = \rho^f_0 = \rho^f$. Next, the resistivities, which are written as functions of the radial strain, are substituted into equation (4.13). Additionally, the radii of the deformed composite, denoted by b_d, and the deformed fiber, denoted by a_d, which are expressed as functions of the undeformed radii and external radial strains, are substituted back into equation (4.13). The axial piezoresistivity in the homogenized composite due to radial strain is represented by the formula indicated in equation (3.35) below.

$$\Delta\rho^c_1(\varepsilon^{ext}_{rr}) = \frac{\rho^f\, N^2(\varepsilon^{ext}_{rr})}{b^2\, D(\varepsilon^{ext}_{rr})\,\left[(\gamma_m - \gamma_f)\,V_f + \lambda_m - \gamma_f)\right]^2} - \frac{\rho^f \rho^m_0}{V_f\rho^m_0 + \rho^f\,(1 - V_f)} \quad (4.35a)$$

Above, $N(\varepsilon^{ext}_{rr})$ and $D(\varepsilon^{ext}_{rr})$, which are functions of ε^{ext}_{rr}, are defined as

$$N(\varepsilon^{ext}_{rr}) = \left[(\lambda_m - \gamma_f)b^2 - (\gamma_m - \gamma_f)a^2\right]\varepsilon^{ext}_{rr} + (\lambda_m - \gamma_f)b^2 + (\gamma_m - \gamma_f)a^2, \quad (4.35b)$$

$$D(\varepsilon_{rr}^{ext}) = a^2 \left[\frac{\lambda_m - \gamma_f}{(\gamma_m - \gamma_f)\, V_f + \lambda_m - \gamma_f}\, \varepsilon_{rr}^{ext} + 1 \right]^2 + 2\rho^f Q(\varepsilon_{rr}^{ext}), \tag{4.35c}$$

where $Q(\varepsilon_{rr}^{ext})$ is the following integration.

$$Q(\varepsilon_{rr}^{ext}) = \int_{\mathrm{LB}(\varepsilon_{rr}^{ext})}^{\mathrm{UB}(\varepsilon_{rr}^{ext})} \frac{r^5}{A(\varepsilon_{rr}^{ext})\, r^4 + 2B(r, \varepsilon_{rr}^{ext}) + \left(\lambda_m^2 + \gamma_f^2\right) \rho_0^m}\, \mathrm{d}r \tag{4.35d}$$

Note that $A(\varepsilon_{rr}^{ext})$ and $B(r, \varepsilon_{rr}^{ext})$ in the integrand above can be calculated as

$$A(\varepsilon_{rr}^{ext}) = 2\,\psi \left(\varepsilon_{rr}^{ext}\right)^3 + \left(\gamma_f^2 + \gamma_m^2\right) V_f^2 \rho_0^m, \tag{4.35e}$$

$$B(r, \varepsilon_{rr}^{ext}) = \left[\left(\lambda_m^2 - \tau\right) \psi r^4 + \Pi_2 a^4 \left(\gamma_f - \gamma_m\right)^2\right] \left(\varepsilon_{rr}^{ext}\right)^2 - \tau\, \kappa\, r^4\, \varepsilon_{rr}^{ext}, \tag{4.35f}$$

where ψ and τ are piezoresistive and mechanical constants corresponding to the constituents, respectively, and were introduced to simplify the above expressions of $A(\varepsilon_{rr}^{ext})$ and $B(r, \varepsilon_{rr}^{ext})$. They are defined as $\psi = 2\Pi_1 + \Pi_2$ and $\tau = 2\gamma_f \lambda_m$. Moreover, in the integration displayed in equation (4.35d) above, the lower and upper bounds of the integration, that is, LB and UB, respectively, are obtained by the following mathematical formulas.

$$\mathrm{LB}(\varepsilon_{rr}^{ext}) = a \left[\frac{\lambda_m - \gamma_m}{(\gamma_m - \gamma_f)\, V_f + \lambda_m - \gamma_f}\, \varepsilon_{rr}^{ext} + 1 \right] \tag{4.35g}$$

$$\mathrm{UB}(\varepsilon_{rr}^{ext}) = b \left[\frac{\lambda_m - \gamma_f - (\gamma_m - \gamma_f) V_f}{(\gamma_m - \gamma_f)\, V_f + \lambda_m - \gamma_f}\, \varepsilon_{rr}^{ext} + 1 \right] \tag{4.35h}$$

Note that both the lower and the upper bounds are linear polynominal functions of the external radial strains, ε_{rr}^{ext}. Equation (4.35) describes the fiber-direction piezoresistivity effect of a nanofiller-modified composite with a continuous fiber-reinforced phase subjected to external radial deformations in the form of radial axisymmetric strains.

4.3 Transverse Piezoresistivity

The derivation of an analytical relation that describes resistivity changes in the lateral direction of a fiber-reinforced composite with a conductive matrix phase subjected to radial deformation, i.e., deformation in a direction perpendicular to the continuous fiber direction, is

discussed throughout this section. As before, we begin by solving the steady-state electrical diffusion problem in both homogeneous and heterogeneous systems. The solutions of the electrical problem allow us to obtain the electric potential field within the composite, which is the primary field of the PDE. Then, by using the electric fields, we would be able to derive the current density distribution vectors. Next, the principle of conservation of electrical energy is applied to electrically homogenize the composite, and a relation is drawn to calculate the effective electrical resistivity of the fiber-reinforced composite. With the aid of the elasticity solution, we can formulate an analytical closed-form mathematical expression that predicts the transverse piezoresistivity as a result of radial external displacements.

4.3.1 Electrical Governing Equations

To derive the electrical governing equation, assume that the potential field is a function of r and θ, that is, $\phi^q = \phi^q(r, \theta)$, where q is replaced by either f, m, or c representing the potential (or later any other variable) within the fiber, the matrix, or the homogenized composite, respectively. From equation (3.1), which represents PDEs that describe steady-state electrical diffusion in a three-dimensional space, we can find the following partial differential equation for steady-state electrical diffusion in the lateral direction.

$$\frac{\partial^2 \phi^q}{\partial r^2} + \frac{1}{r^2}\frac{\partial^2 \phi^q}{\partial \theta^2} + \frac{1}{r}\frac{\partial \phi^q}{\partial r} = 0 \tag{4.36}$$

The above PDE is identical to that described previously in equation (3.27), which is derived based on the assumption that the resistivity within an electrically isotropic material (i.e., the resistivity value is the same in all directions) is constant, in other words, ρ^q does not show spatial dependence. This governing equation is true for the homogenized composite, although it is electrically transversely isotropic, in which the z axis, directed along the fiber direction, is the axis of symmetry, and the x-y plane is the plane of symmetry. As a result of this anisotropy, the resistivity in the radial direction within the homogenized composite, ρ_r^c, is equal to the resistivity in the angular direction ρ_θ^c, but different from the resistivity along the longitudinal direction. Consequently, the transverse resistivity of the homogenized composite is referred to as ρ_{20}^c before deformation and ρ_{2d}^c after deformation. Equation

(4.36) also holds for the fiber phase, regardless of the strain states, since it would have constant resistivity values before and after deformations. Note that this is true as well for the undeformed matrix phase with a constant base resistivity value equals ρ_0^m. However, as we have observed before in equations (4.31), since the strain tensor within the deformed matrix varies radially, the resistivity within the matrix is a function of r, as illustrated in equation (4.34). As a result, the following partial differential equation governs the electrical diffusion within the deformed nanofiller-modified matrix phase.

$$\frac{1}{\rho_d^m(r)}\left(\frac{\partial^2\phi^m}{\partial r^2}+\frac{1}{r}\frac{\partial\phi^m}{\partial r}+\frac{1}{r^2}\frac{\partial^2\phi^m}{\partial\theta^2}\right)-\frac{1}{\rho_d^m(r)}\frac{d\rho_d^m(r)}{dr}\frac{\partial\phi^m}{\partial r}=0 \tag{4.37}$$

Note that this PDE is unsolvable, analytically at least, due to the appearance of the second term caused by the fact that the resistivity of the matrix subjected to external radial strain is not constant as the resulted internal strain tensor of the matrix is a function of r. Consequently, the effective resistivity of the homogenized composite after deformation can not be calculated analytically (in a straightforward manner) as we have done previously in Chapter 3. We will later see how we can tackle this issue.

4.3.2 Effective Resistivity Relations

Here, the effective resistivity relations for the composite before and after deformations are derived based on the CCA electrical homogenization techniques.

Since the effective resistivity values of the homogenized composite (before and after deformations), as well as the resistivities of the fiber and matrix phases within the undeformed heterogeneous system, are constants, we can use the governing equations, presented in equation (4.36), and impose the conservation of energy law. This will allow us to calculate the effective lateral resistivity of the homogenized composite and the effective lateral resistivity of the heterogeneous composite prior to deformation. We can follow a similar procedure as discussed earlier in Chapter 3, particularly Section 3.3, where we can start by assuming

the following general solution for (4.36) representing the potential distribution within the inhomogeneous and homogeneous systems.

$$\phi^f(r,\theta) = (Cr + \frac{E}{r})\cos\theta, \quad \text{for } 0 \le r \le a \tag{4.38a}$$

$$\phi^m(r,\theta) = (Fr + \frac{G}{r})\cos\theta, \quad \text{for } a \le r \le b \tag{4.38b}$$

$$\phi^c(r,\theta) = (Hr + \frac{K}{r})\cos\theta, \quad \text{for } 0 \le r \le b \tag{4.38c}$$

In the above equations, C, E, F, G, H, and K are all integration constants such that finding their values allows us to identify the particular solutions of their corresponding PDEs. From the above general solutions, we can directly deduce that for the potentials in both the fiber and the homogenized composite, which are illustrated in equations (4.38a) and (4.38c), respectively, to have finite values at $r = 0$; that is, to avoid singularities, both integration constants E and K must be zero. Then, applying the electrical boundary and continuity conditions illustrated in Figure (3.3), which can be summarized below, we would be able to fully identify the potential of both systems prior to radial deformations.

$$E_r^m = E_{ext}\cos\theta \tag{4.39a}$$

$$\phi^m(r=a,\theta) = \phi^m(r=a,\theta) \tag{4.39b}$$

$$\frac{1}{\rho^f}\frac{\partial\phi^f(r=a,\theta)}{\partial r} = \frac{1}{\rho_0^m}\frac{\partial\phi^m(r=a,\theta)}{\partial r} \tag{4.39c}$$

$$E_r^c = E_{ext}\cos\theta \tag{4.39d}$$

Please refer to Chapter 3 for more details regarding the derivation of the above electrical boundary and continuity conditions. Now, we have four unknowns, which are C, F, G, and H, and four conditions. For the homogenized composite, we can directly find the value of H by substituting equation (4.38c) into equation (4.39d) while taking into consideration that

the electric field, E, would be related to the potential, ϕ and the current density distribution vector, $\mathbf{J}$, throughout the following mathematical relation.

$$\mathbf{J}^q = \frac{1}{\rho^q}\,\mathbf{E}^q = -\frac{1}{\rho^q}\nabla\phi^q = -\frac{1}{\rho^q}\left\{\begin{array}{cc}\frac{\partial\phi^q}{\partial r} & \frac{1}{r}\frac{\partial\phi^q}{\partial\theta}\end{array}\right\}^T \tag{4.40}$$

It can be calculated that $H = -E_{ext}$, thus, the electric potential distribution within the undeformed homogeneous system is $\phi^c(r,\theta) = -E_{\text{ext}}\, r\, \cos\theta$. For the fiber and the matrix phases within the inhomogeneous system, we can arrive at the following expressions by imposing the Neumann boundary condition represented in equation (4.39a) and the electrical continuity conditions at the matrix-fiber interface that are shown in equations (4.39b) and (4.39c).

$$b\,F + \frac{1}{b}\,G = -E_{\text{ext}}\,b \tag{4.41a}$$

$$a\,C - a\,F - \frac{1}{a}G = 0 \tag{4.41b}$$

$$\frac{1}{\rho^f}C - \frac{1}{\rho_0^m}F + \frac{1}{a^2\rho_0^m}G = 0 \tag{4.41c}$$

Solving the above system of three equations with three unknowns gives us the values of C, F, and G. By now, we should have fully recognized the potential distributions in both the homogeneous and heterogeneous systems.

Next, to electrically homogenize the composite in the transverse direction, the conservation of electrical energy is considered. In fact, a version of it was already stated in Chapter 3 as the idea of equal average current densities represented in equation (3.38). That assumption was, in fact, based on the law of conservation of electrical energy [83] and the derivation is explained in more detail below. First, let us define a quantity called the volume power density, denoted by w, which is defined as the amount of electrical energy transferred per second per unit volume. It can be mathematically defined as

$$w = \mathbf{J}\cdot\mathbf{E} = J_{\text{i}}\,E_{\text{i}}, \quad \text{i} = 1,2,3 \tag{4.42}$$

or, in words, the volume power density is the dot product of the current density vector and the electric field vector. It has an SI unit of Watt per cubic meter. The version of the law of

conservation of electric energy utilized here states that the volumetric average of the volume power density within the homogeneous system equals the volumetric average of the volume power density within the non-homogeneous system. This is expressed mathematically as $\bar{w}^H = \bar{w}^{nH}$, where the bar accents denote the volumetric averages, and the superscript H refers to the homogeneous system, whereas the superscript nH refers to the non-homogeneous system. According to equation (4.42), the volumetric average of the energy conservation expression can be expressed in terms of the current density and electric field as follows.

$$\bar{J}_{\mathrm{i}}^H \bar{E}_{\mathrm{i}}^H = \bar{J}_{\mathrm{i}}^{nH} \bar{E}_{\mathrm{i}}^{nH} \tag{4.43}$$

Both systems are subjected to the same potential boundary conditions, $\bar{E}_{\mathrm{i}}^H = \bar{E}_{\mathrm{i}}^{nH}$, therefore, from the above equation, the volumetric average of the current density vector for the homogeneous composite equals to the volumetric average of the current density vector for the non-homogeneous composite, which is the sum of the volumetric averages of the current densities within the constituents of the non-homogeneous composite, i.e.,

$$\bar{J}_{\mathrm{i}}^H = \bar{J}_{\mathrm{i}}^{nH} = \bar{J}_{\mathrm{i}}^f + \bar{J}_{\mathrm{i}}^m. \tag{4.44}$$

Note how the expression in equation (4.44) is identical to the expression illustrated previously in equation (3.38), where $\bar{J}_{\mathrm{i}}^H = \bar{\mathbf{J}}^c$. In general, to find the volumetric average of a field function, M, which can be a scalar or a vector field, the following integration is calculated over the volume of the domain.

$$\bar{M} = \frac{1}{V_M} \int_{V_M} M \, \mathrm{d}V_M \tag{4.45}$$

Above, V_M is the volume of the domain where the volumetric average is carried out. Imposing the above-mentioned conservation law while following a procedure similar to the one described in Chapter 3, particularly in equations (3.38) to (3.43), we can derive a formula de-

scribing the effective resistivity in a fiber-reinforced composite along the transverse direction, which is shown below.

$$\rho_{20}^{c} = \rho_0^m \frac{V_f\left(\rho^f - \rho_0^m\right) + \left(\rho^f + \rho_0^m\right)}{V_f\left(\rho_0^m - \rho^f\right) + \left(\rho^f + \rho_0^m\right)} \tag{4.46}$$

The above expression is sufficient to calculate the transverse base resistivity of a composite (resistivity of a non-deformed composite) knowing the fiber volume fraction, V_f, the base resistivity of the fiber, ρ^f, and the base resistivity of the electrically isotropic piezoresistive matrix, ρ_0^m.

Now, let us revisit the governing equation for the deformed matrix, which was previously presented in equation (4.37). We will use this equation to continue our analysis and determine the effective electrical property of the homogenized *deformed* composite. The problem with the given PDE is that it cannot be solved using analytical approaches because the resistivity of the matrix under radial strain depends on r. Hence, we are presented with two alternatives to resolve this matter. First, we can attempt to solve this PDE using numerical methods, which will be demonstrated in the subsequent chapter through the use of the finite element approach. However, this will cause us to deviate from our original goal of developing a closed-form mathematical expression for predicting resistivity changes due to radial deformation. Alternatively, we can make the assumption that the strain tensor within the deformed matrix, which leads to a variable matrix resistivity, can be approximated as the volumetric average using the same principle as demonstrated in equation (4.45). As a consequence, the volumetric average of the radial strain in the matrix is calculated as follows.

$$\bar{\varepsilon}_{rr}^{m}\left(\varepsilon_{rr}^{ext}\right) = \frac{1}{V_m}\int_{V_m} \varepsilon_{rr}^{m}\left(r, \varepsilon_{rr}^{ext}\right)\, \mathrm{d}V_m = \frac{2}{b^2 - a^2}\int_a^b \varepsilon_{rr}^{m}\left(r, \varepsilon_{rr}^{ext}\right)\, r\, \mathrm{d}r \tag{4.47}$$

Above, V_m, in this context, refers to the volume of the matrix phase within the CCA composite model. It should be noted that the integral found on the right-hand side of equation (4.47), which is only over r, is obtained by first integrating $\varepsilon_{rr}^{m}\left(r, \varepsilon_{rr}^{ext}\right)$ over θ (ranging from 0 to 2π), then over z (ranging from 0 to l), followed by applying mathematical simplifications. The volumetric average of the angular strain of the deformed matrix $\bar{\varepsilon}_{\theta\theta}^{m}\left(\varepsilon_{rr}^{ext}\right)$ can also be calculated in the same way. By this approach, we can have the strain tensor as a function of

the applied radial strain alone. Consequently, the change in the resistivity of the deformed matrix, according to the Koo and Tallman relation represented in equation (4.34), can be estimated by using the volumetric average of the strain tensor, rather than directly using it. This approach will ensure that the resistivity in the deformed matrix is constant (quasi-constant) such that the governing equation, presented in equation (4.36), is now applicable. Eventually, we can find the effective resistivity of the deformed composite in the same way as we did for the non-deformed one using equation (4.46) while considering the geometrical and electrical properties of the deformed composite.

4.3.3 Resistivity-Strain Analytical Relation

The change in resistivity of the composite under radial external strain can be obtained by finding the difference between the resistivity of the composite before and after deformation. That is, $\Delta\rho_2^c = \rho_{2d}^c - \rho_{20}^c$, where ρ_{20}^c is found previously in equation (4.46) and ρ_{2d}^c is approximated by considering the average strain tensor of the deformed matrix. Ultimately, we can arrive at the following mathematical expression for the change in resistivity as a function of ε_{rr}^{ext}.

$$\Delta\rho_2^c(\varepsilon_{rr}^{ext}) = \left[\left(\Gamma\,\varepsilon_{rr}^{ext}+1\right)^2 + \left(\Psi\,\varepsilon_{rr}^{ext}+1\right)^2\right] F(\varepsilon_{rr}^{ext}) - \rho_0^m \frac{V_f\left(\rho^f-\rho_0^m\right)+\left(\rho^f+\rho_0^m\right)}{V_f\left(\rho_0^m-\rho^f\right)+\left(\rho^f+\rho_0^m\right)} \tag{4.48}$$

The introduced placeholders above, which are Γ, Ψ, and F, can be calculated as follows.

$$\Gamma = (\lambda_m - \gamma_m)\,\Lambda^{-1} \tag{4.49a}$$

$$\Psi = \left[(\gamma_f - \gamma_m)\,V_f + \lambda_m - \gamma_f\right]\Lambda^{-1} \tag{4.49b}$$

$$F(\varepsilon_{rr}^{ext}) = \Phi\,\varepsilon_{rr}^{ext} - 2\,(\Pi_1+\Pi_2)\,T + a^2\left(\rho^f-\rho_0^m\right) \tag{4.49c}$$

Similarly, Φ, and T, are placeholders representing constants that can be calculated according to the following relations.

$$\Phi = \left[2\,\kappa\,(\gamma_f - \lambda_m)\right]\Lambda^{-1} \tag{4.50a}$$

$$T = \left[\lambda_m^2 - \gamma_f^2 + \frac{4a^4 \left(\ln a - \ln b\right)^2 \left(\gamma_f - \gamma_m\right)^2}{\left(a^2 - b^2\right)^2}\right] \Lambda^{-1} \tag{4.50b}$$

In equations (4.49) and (4.50) above, Λ also represents a constant, which can be calculated as shown in equation (4.51) below.

$$\Lambda = \left(\gamma_m - \gamma_f\right) V_f + \lambda_m - \gamma_f \tag{4.51}$$

It is worth mentioning that although we were unable to analytically solve the electromechanical problem for radially deformed composites and derive an exact solution, this method still provides a reliable approximation. As we demonstrate in the Results and Discussion section, this approach offers insight into the electrical behavior of nanofiller-modified composites with fiber reinforcement when subjected to radial deformations. Moreover, computationally, it is significantly more cost-effective than employing numerical methods such as the finite-element approach.

4.4 Results and Discussions

In this section, the derived piezoresistive analytical model is validated and demonstrated. For validation, the homogenized solutions obtained are compared with the exact solutions, which are the solutions acquired by directly solving the BVP of the heterogeneous composite without homogenization. We also compare our model with the predictions obtained from a simple rule of mixtures, similar to the one shown in equation (3.51). As we have previously accomplished in Chapter 3, we will assume that the reinforcing fiber phase is either a carbon fiber or a glass fiber. In addition, both phases within the composite are assumed to be mechanically and electrically isotropic. However, unlike the axial strain case, where the composite was assumed to experience a uniaxial tension caused by an externally applied axial strain, the composite here is subjected to a uniform axisymmetric radial strain, which enables us to observe radial strain-induced axial and transverse piezoresistivity.

It is worth mentioning that, unlike the axial deformation situation in which the reinforcing fibers carry most of the stresses, the external radial deformation is applied directly to the conductive matrix. This generally results in higher matrix deformations compared to the

case of axial strain. As a result, lower values of external radial strains must be considered, compared to those of the axial strain case, to avoid exceeding the limitations of the Koo and Tallman strain-resistivity relation [113]. High strains can lead to incorrect predictions of resistivity changes. That is, the piezoresistive constants in the relation were obtained by curve fitting of the observed resistivity changes in specimens subjected to uniform axial displacements, resulting in axial strains ranging from -6 mε to 6 mε. Therefore, to remain within these limits, we assume that the current applied radial strain must remain within 80% of the Poisson-induced transverse strains resulting from axially applying -6 mε to 6 mε. In other words, we apply radial strains according to the following limits.

$$-0.8\,\nu^m \left(6 \times 10^{-3}\right) \leq \varepsilon_{rr}^{ext} \leq 0.8\,\nu^m \left(6 \times 10^{-3}\right) \tag{4.52}$$

Above, ν^m is the conductive matrix Poisson's ratio. The mechanical and electrical properties of the constituents used to demonstrate the developed models are found in Table 3.1 of the previous chapter. We also use the same matrix composition, which is an epoxy modified with 1 wt.% CNFs, and the piezoresistive constants, which were shown in equation (4.34), are as follows: $\kappa = 4.10\,k\Omega \cdot m$, $\Pi_1 = -150\,k\Omega \cdot m$, and $\Pi_2 = 5.15\,k\Omega \cdot m$ [113]. As a result, we will assume that the applied external radial strains fall between $-1.4 \times 10^{-3} \leq \varepsilon_{rr}^{ext} \leq 1.4 \times 10^{-3}$, that is, the outer surface of the CCA assembly undergoes a uniform axisymmetric radial displacement resulting in strains ranging from -1.4 mε to 1.4 mε, which are well below the presumed limits estimated using equation (4.52) above.

Next, we validate the output of our analytical model using the solutions of the heterogeneous system, which is gained by directly solving the mechanical and electrical BVPs for the inhomogeneous fiber+matrix system shown on the right side of Figure 3.1. As we discussed above, since applying transverse strain leads to resistivity within the matrix that varies radially, we first need to consider the electrical current within the unstrained system in the axial direction, which then is used to calculate the axial resistance and resistivity. After that, the axial resistivity of the deformed heterogeneous system is calculated using the calculated axial current and the corresponding resistance. In detail, when the system is deformation-free, the overall axial current within the inhomogeneous composite can be calculated in a similar way

to the equation (3.47), which is obtained by integrating the current density. Thus, the axial current of the undeformed fiber+matrix composite can be calculated using the following relation.

$$I^{exact}_{axial,0} = I^{f}_{axial,0} + I^{m}_{axial,0} = \frac{\phi_0}{l\rho^{f}_{0}}\pi a^2 + \frac{\phi_0}{l\rho^{m}_{0}}\pi\left(b^2 - a^2\right) \tag{4.53}$$

Here, we use the superscript e*xact* to indicate the inhomogeneous solution, whereas the subscripts 0 indicates properties of the initial (non-deformed) system. In light of equations (4.5) through (4.11), we can express the current along the fiber direction for the inhomogeneous system as follows.

$$I^{exact}_{axial,d} = I^{f}_{axial,d} + I^{m}_{axial,d} = \frac{\phi_0}{l\rho^{f}_{d}}\pi a^2_d + \frac{2\pi\phi_0}{l}\,\omega^{m}_{\rho} \tag{4.54}$$

Above, the subscripts d refers to properties of the system after deformation, and ω^{m}_{ρ} is the integration of the matrix resistivity along the radial direction, as illustrated in equation (4.11b). Note that the axial current in equation (4.54), i.e, $I^{exact}_{axial,d}$, depends on the applied radial strain, since the values of the geometrical and electrical properties of the constituents are functions of the applied radial strain, that is, the axial current $I^{exact}_{axial,d}$ is a function of the applied radial strain. To obtain the resistivity values, we set ϕ_0 to be 10V; then, the resistance due to the applied voltage is calculated using Ohm's law. From the calculated resistance, the resistivity of the system can be predicted as follows.

$$\rho^{exact}_{1} = R_{exact}\frac{A}{l} \tag{4.55}$$

The expression above can be used to calculate the axial resistivity of the system before and after deformations, where l is the overall longitudinal dimension, which is assumed to be 100μm, and A is the cross-sectional area. Strain-induced axial resistivity changes can be calculated by finding the difference between the resistivity values before and after deformations.

In a similar manner, we also aim to compare our homogenized model for transverse piezoresistivity with the exact solution. Consider the total current density within the inhomogeneous system, which is assumed to be the volumetric average of the sum of the current

densities within the fiber and the matrix along the transverse x direction. This can be mathematically expressed as follows.

$$J_{trans}^{exact} = J_x^{avg} = \frac{1}{V}\int_V (J_x^f + J_x^m)\,\mathrm{d}V \tag{4.56}$$

In the above equation, the subscript *trans* refers to the transverse direction, V is the volume of the cylindrical system, and the current densities of the fiber J_x^f and the matrix J_x^m can be calculated using equations (3.40b) and (3.40c), respectively. Here, the resistivity can be derived by imposing the continuum form of Ohm's law, which states that $\mathbf{E} = \rho\mathbf{J}$, where the only non-zero component of the electric field vector, $\mathbf{E}$, is the x components, since we only apply an external electric field in the transverse x-direction, as illustrated in Figure (3.3). Eventually, the following expression is used to obtain the resistivity of the heterogeneous composite in the transverse direction.

$$\rho_2^{exact} = \frac{E_{ext}}{J_{trans}^{exact}} \tag{4.57}$$

Above, E_{ext} is the externally applied electric field along the x-axis. Note that equations (4.56) and (4.57) can be used directly to find the resistivity in the undeformed composite. However, since the resistivity of the deformed matrix varies in the r direction, we have to consider the volumetric averages of the radial and angular strains, calculated using equation (4.47), in order to express the resistivity of the matrix after deformation as quasi-constant (found using the Koo and Tallman relation as shown in equation (4.34). This would allow us to calculate the current density in the x direction of the deformed matrix, and consequently use equations (4.56) and (4.57) to find the overall resistivity of the deformed inhomogeneous system. Again, similar to the exact axial piezoresistivity, the difference between the transverse resistivity values calculated before and after radial deformations, using the above expressions, is considered to be the exact transverse piezoresistivity of the composite.

Figures 4.2 through 4.5 present results for nanocomposites with 20, 40, 60, and 80 vol.% of glass fibers, from which several observations can be made. First, across all the figures, it is evident that the exact solution aligns closely with the proposed model for both axial and

transverse piezoresistivity. Additionally, it is observed that the predictions obtained via the rule of mixtures deviate significantly compared to the homogenization results. These discrepancies, especially between the axial and transverse piezoresistivity, become more pronounced at higher glass fiber volume fractions. A possible explanation is the increased anisotropy of the composite with higher fiber volume fractions. On the contrary, reducing the fiber content leads to the convergence of predictions (axial, transverse, and rule of mixtures), as the electrical characteristics of the composite approach those of a pure isotropic CNF-modified epoxy. Thus, although the rule of mixtures offers a simpler prediction method for piezoresistivity, its assumption of isotropy results in directionless and highly inaccurate predictions, especially at high fiber volumes, where the composite is markedly anisotropic.

Similarly to glass fiber nanocomposites, our model predictions for nanofiller-modified epoxy containing 20, 40, 60, or 80 vol.% of continuous carbon-fiber reinforcement were explored. Figures 4.6 through 4.9 display these results, calculated using the homogenization model, exact solutions, and the rule of mixtures. Here again, the exact solutions closely match the homogenization results. Unlike glass fiber composites, carbon fibers' high conductivity leads to no change in axial resistivity regardless of the carbon fiber volume fraction. More specifically, most of the electric current along the axial direction travels along the highly conductive and non-piezoresistive carbon fibers, resulting in an overall non-piezoresistive composite, despite the conductive matrix (which has much lower conductivity compared to that of carbon fiber). However, piezoresistive behavior is observed in the transverse direction, as the current must first pass through the piezoresistive matrix, resulting in a piezoresistive composite. Therefore, in carbon fiber nanocomposites, radial strain-induced resistivity changes are only observed in the transverse direction. Moreover, the rule of mixtures proves inadequate for predicting piezoresistivity in carbon fiber-reinforced nanocomposites, especially at higher carbon fiber contents.

Further observations are made on the differences in piezoresistive characteristics between glass and carbon fiber composites subjected to axial or radial deformations. Unlike carbon fiber composites, increasing the volume fraction of glass fiber leads to steeper slopes of resistivity change curves as a larger current is forced through the relatively high conductive piezoresistive matrix. This also explains the observation of axial piezoresistivity in com-

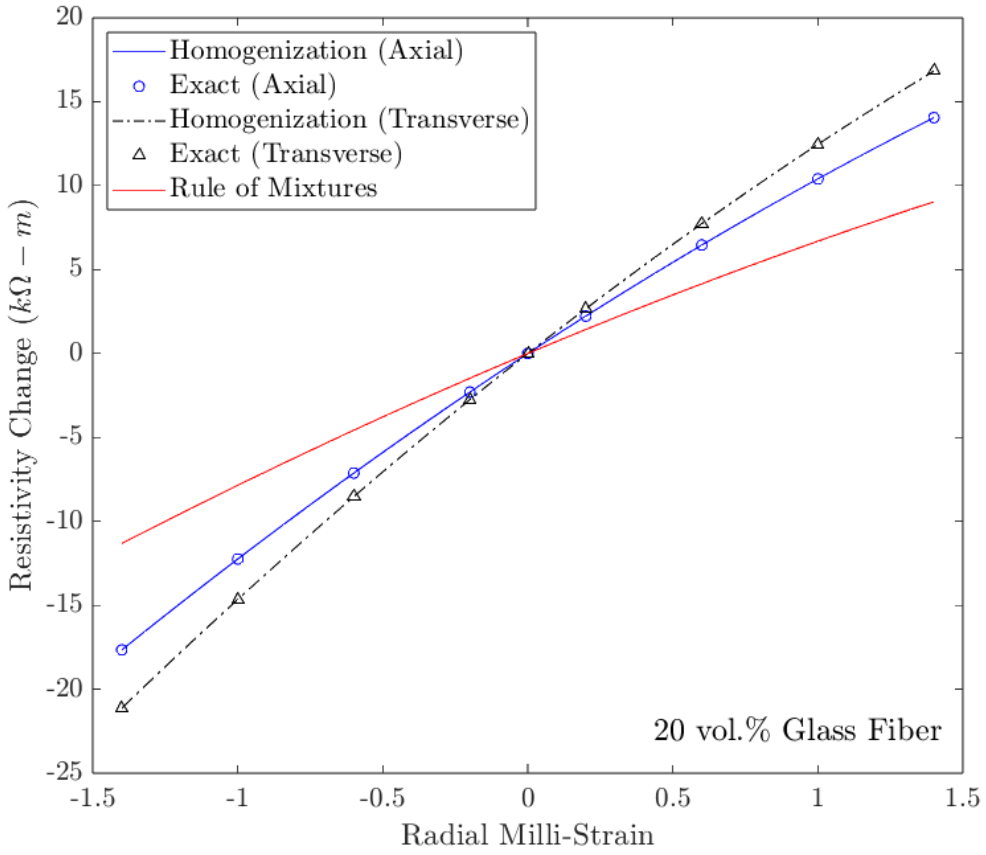

Figure 4.2. The change in the axial and transverse resistivity as a function of radial strain of CNF-modified epoxy composite with glass fiber reinforcement at 20 vol.% glass fiber based on CCA homogenization model, the exact solution, and the rule of mixtures.

posites with electrically insulating glass fibers. Comparing these results for piezoresistivity induced by radial strains with those discussed in the previous chapter for axial strains reveals generally higher resistivity changes for lower radial strains compared to axial strains. This suggests that fiber-reinforced nanocomposites tend to exhibit higher piezoresistivity when subjected to radial strains. A possible reason is that radial displacements directly affect the piezoresistive matrix, which has a significantly lower elastic modulus, leading to greater matrix deformations compared to the axial strain case, where the fibers, with enormously higher elastic moduli, bear most of the load, resulting in smaller matrix deformations. In

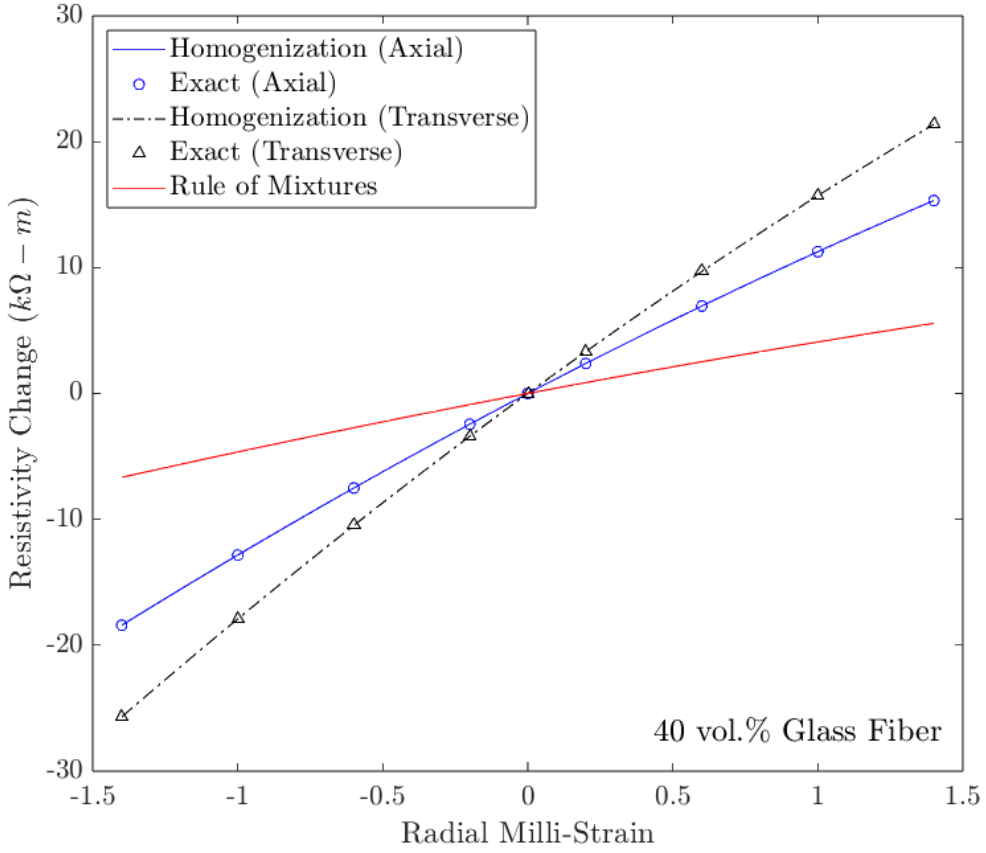

Figure 4.3. The change in the axial and transverse resistivity as a function of radial strain of CNF-modified epoxy composite with glass fiber reinforcement at 40 vol.% glass fiber based on CCA homogenization model, the exact solution, and the rule of mixtures.

summary, greater matrix deformations and thus more significant strain-induced resistivity changes occur when radial strains are applied to the nanocomposite.

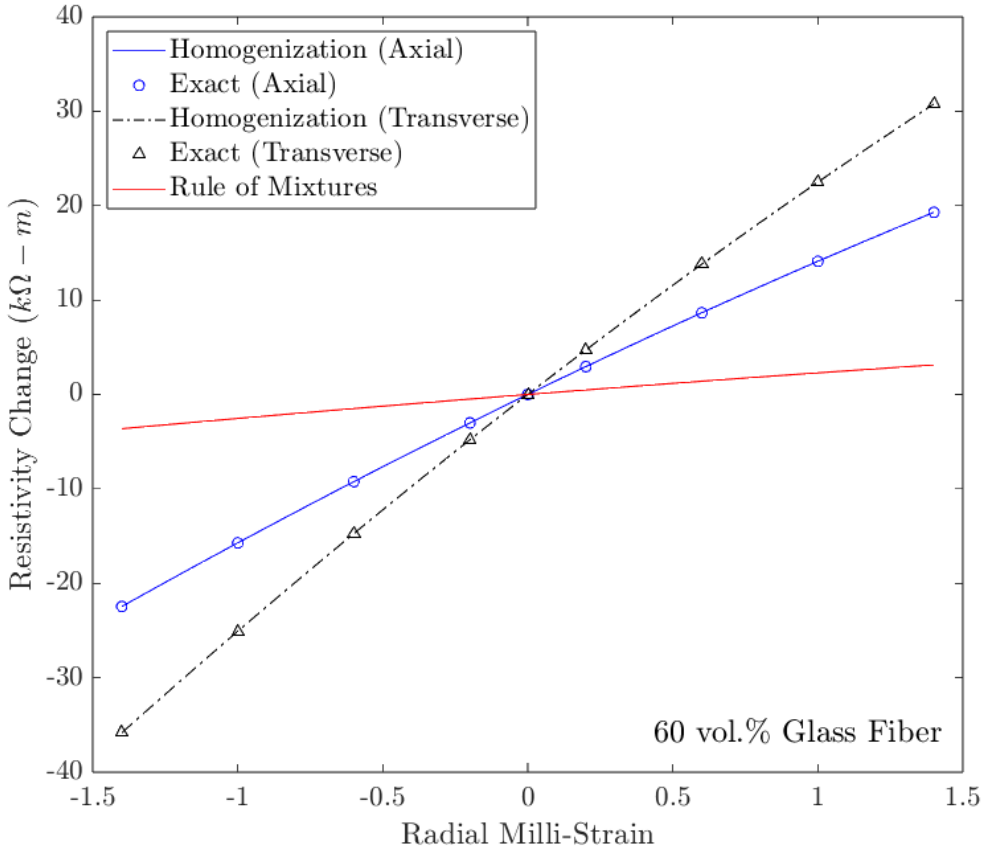

Figure 4.4. The change in the axial and transverse resistivity as a function of radial strain of CNF-modified epoxy composite with glass fiber reinforcement at 60 vol.% glass fiber based on CCA homogenization model, the exact solution, and the rule of mixtures.

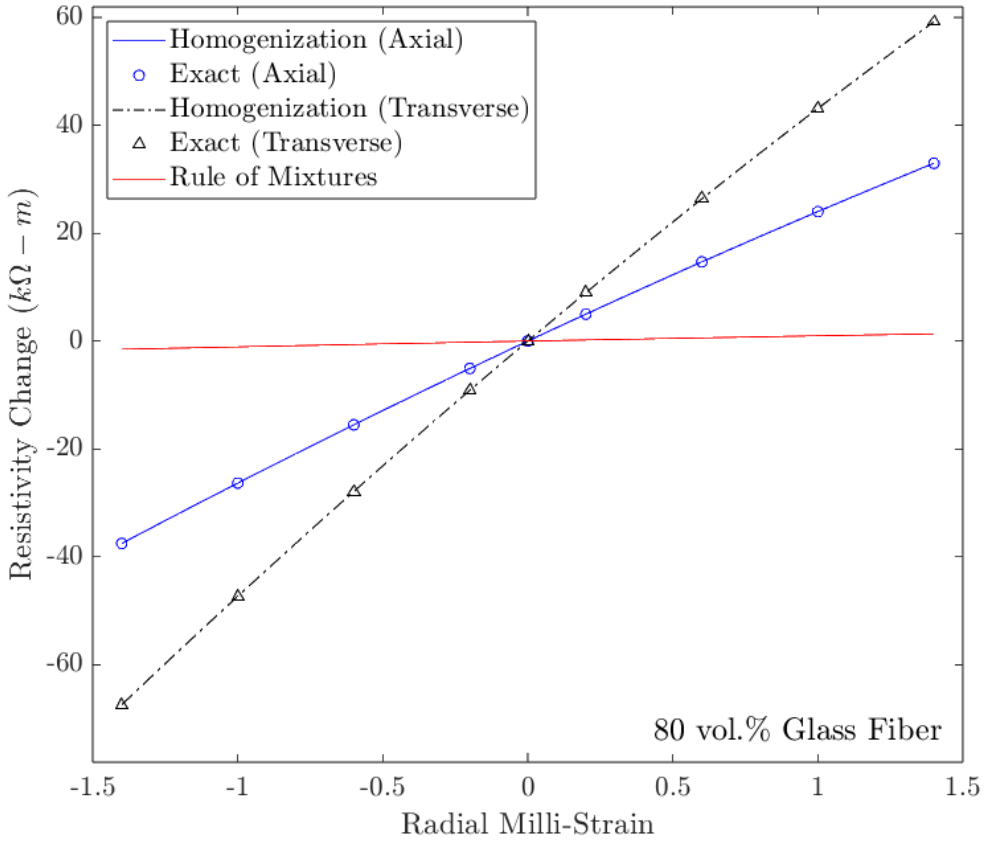

Figure 4.5. The change in the axial and transverse resistivity as a function of radial strain of CNF-modified epoxy composite with glass fiber reinforcement at 80 vol.% glass fiber based on CCA homogenization model, the exact solution, and the rule of mixtures.

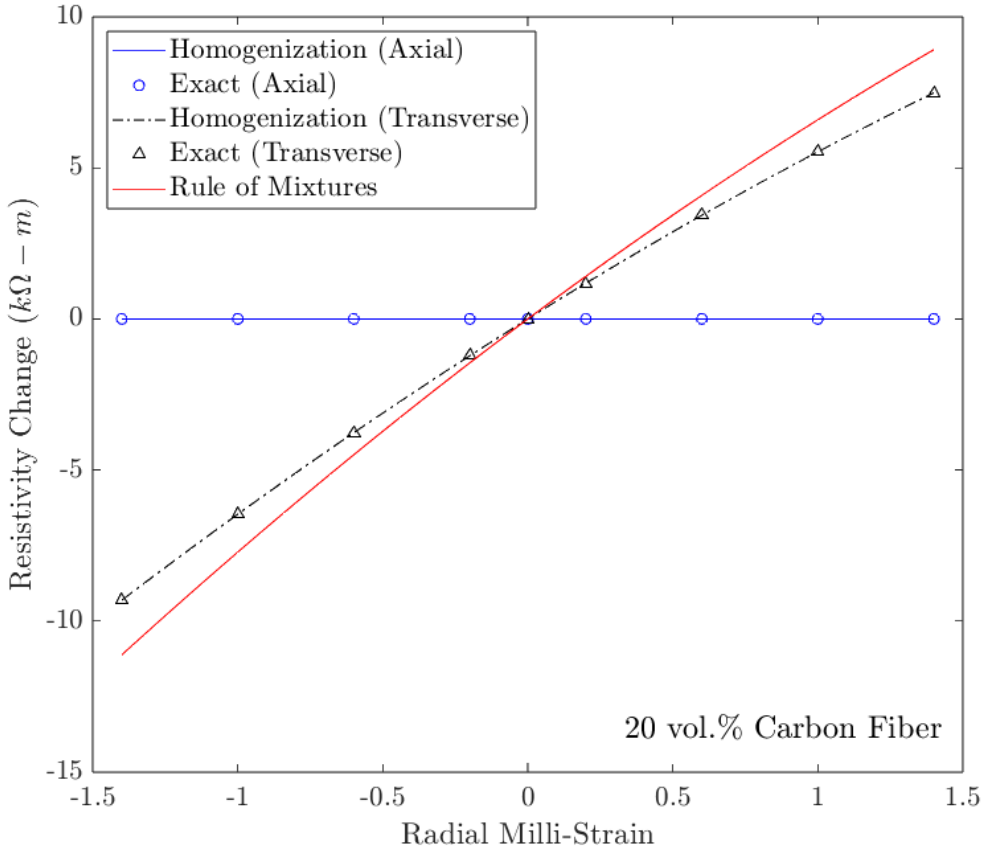

Figure 4.6. The change in the axial and transverse resistivity as a function of radial strain of CNF-modified epoxy composite with carbon fiber reinforcement at 20 vol.% carbon fiber based on CCA homogenization model, the exact solution, and the rule of mixtures.

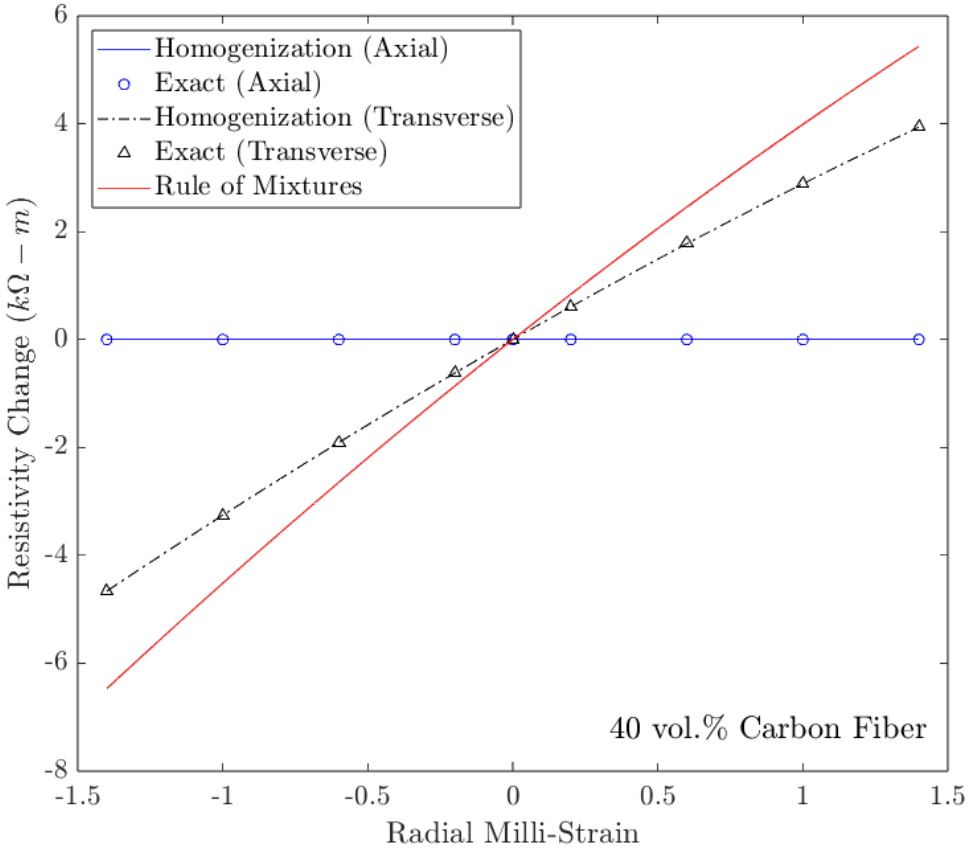

Figure 4.7. The change in the axial and transverse resistivity as a function of radial strain of CNF-modified epoxy composite with carbon fiber reinforcement at 40 vol.% carbon fiber based on CCA homogenization model, the exact solution, and the rule of mixtures.

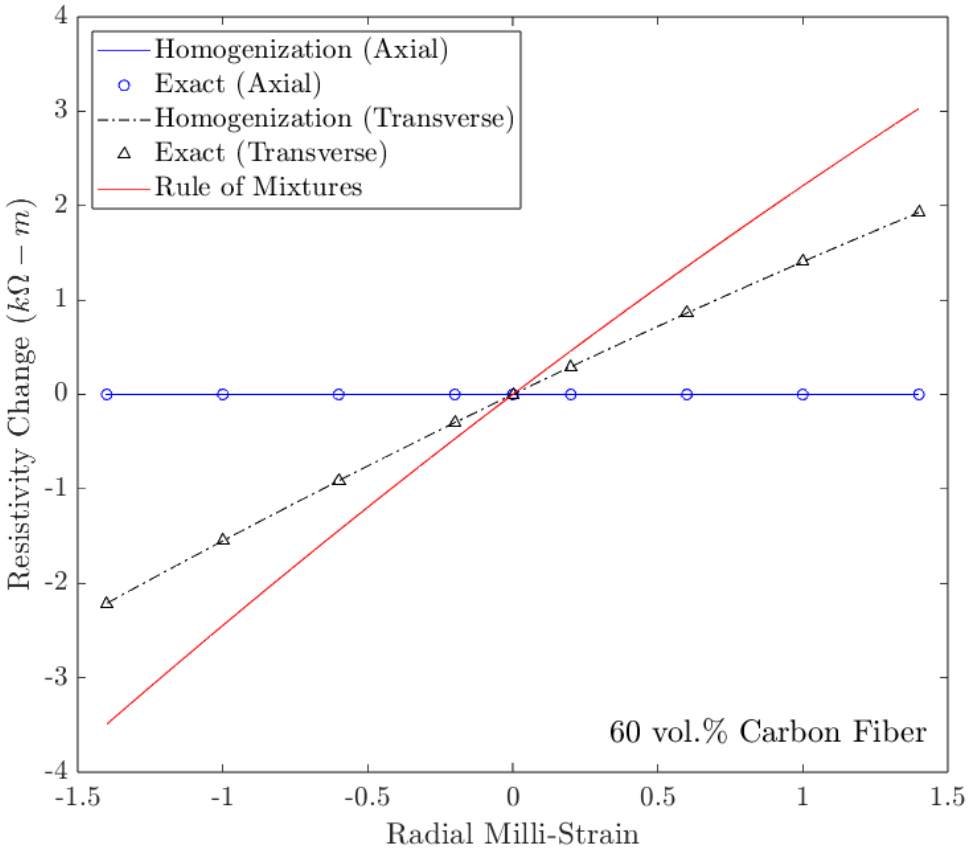

Figure 4.8. The change in the axial and transverse resistivity as a function of radial strain of CNF-modified epoxy composite with carbon fiber reinforcement at 60 vol.% carbon fiber based on CCA homogenization model, the exact solution, and the rule of mixtures.

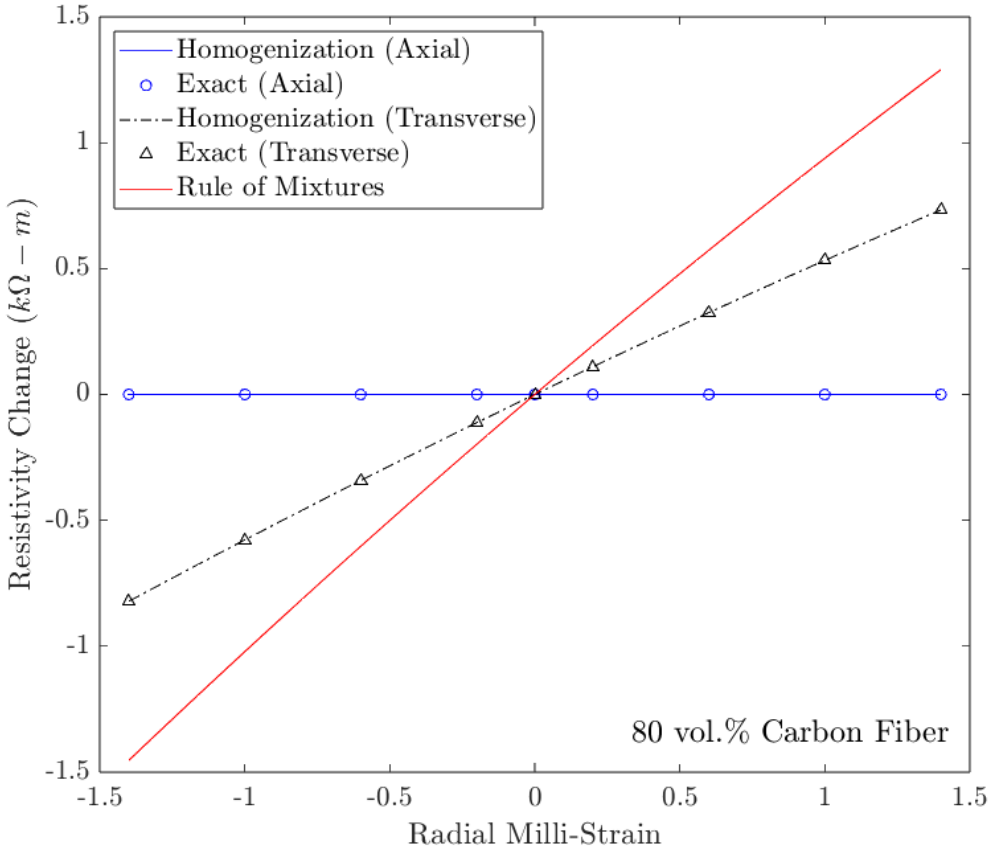

Figure 4.9. The change in the axial and transverse resistivity as a function of radial strain of CNF-modified epoxy composite with carbon fiber reinforcement at 80 vol.% carbon fiber based on CCA homogenization model, the exact solution, and the rule of mixtures.

5. LAMINA-LEVEL VALIDATION VIA COMPUTATIONAL ANALYSES

5.1 Introduction

The CCA electrical homogenization technique, which was implemented in our study to determine the piezoresistivity at the fiber level (as presented in Chapter 3 and Chapter 4), has previously been used to only determine the *effective* electrical conductivity of carbon fiber-reinforced composites [100] or nanofiller-modified glass fiber-reinforced composite laminates [125]. Nevertheless, in these studies, neither strain nor piezoresistive effect were assessed. Besides which, interactions between neighboring continuous fibers were simply overlooked. It was believed that the electrical properties of a single long continuous reinforcing fiber surrounded by a conductive or pure matrix phase are representative of those of the entire lamina. This might be a valid assumption if the effect of strain on resistivity is not taken into account. However, strain induces alterations in the electrical characteristics of the interfiber conductive phase. Consequently, it is currently unclear whether the piezoresistivity predictions at the single fiber level (i.e., the CCA results that were previously displayed) are comparable to those at the lamina-level at which a group of unidirectional parallel reinforcing fibers are involved.

In light of the above discussion, this chapter presents a computational analysis using the finite element analysis (FEA) approach for modeling piezoresistivity in fiber-reinforced, nanofiller-modified composites at the lamina level. The primary objective of this study is to conduct a comparative investigation between computationally derived lamina-level predictions and analytical predictions based on a single-fiber level. Utilizing this computational lamina-level approach offers the benefit of obtaining a deeper understanding of the impact of potential interactions among neighboring fibers on macroscale piezoresistivity. This enables us to determine the applicability of the previously established analytical relations for fiber-reinforced piezoresistive laminae.

In our approach, the lamina is represented by a fiber bundle composite (FBC), which is defined as a cluster of adjacent continuous reinforcing fibers encapsulated by a matrix phase, as illustrated in Figure 5.1. However, given that an FBC may encompass a sig-

nificant number of fibers, leading to high computational costs, we need to scale down our analysis. Therefore, a microscale three-dimensional representative volume element (RVE) is considered, where periodic boundary conditions are imposed to approximate the macroscale behaviors of the composite. The RVE, which consists of multiple nearby fibers embedded inside a piezoresistive matrix phase, is assumed to possess a hexagonal packing arrangement. This adopted arrangement provides the highest possible fiber volume fraction, allowing for a broader perspective on the effect of varying the fiber volume fraction. This configuration is also inspired by the RVE proposed by Ren and Siedel [83], [126], where they modeled the piezoresistivity of a well-dispersed CNT-modified epoxy. However, in our specific scenario, the RVE represents long fibers within a modified matrix, as illustrated in Figure 5.2. By the end of this chapter, we should have a better understanding of the electromechanical behaviors of laminae. This allows for a comparison of the results obtained using the computational RVE approach with those from the CCA method, assessing the effectiveness of using the CCA model for estimating strain-induced resistivity changes in fiber-reinforced nanocomposite laminae.

During the analysis, a specific simulation procedure is adhered to, which will be elaborated upon later. Generally speaking, strains are applied to the RVE as voltage-current relationships are measured along certain directions. From these voltage-current relations, effective resistivity values can be calculated. Moreover, the piezoresistive relation developed by Koo and Tallman [113] is used to predict the resistivity change of the matrix.

5.2 Model Development

In this section, we detail the development of our computational model, which was inspired by Ren et al. [83], [126], who modeled piezoresistivity in composites made of well-dispersed nanofillers. For the sake of clarity, we will employ a comparable modeling procedure, but introduce essential modifications to accommodate a continuous fiber reinforcement phase embedded within a nanofiller-modified matrix phase. To elaborate, the computational model developed in their study was designed to simulate a collection of individual CNTs within a pure matrix phase, with piezoresistivity attributed to either the inherent piezoresistivity of

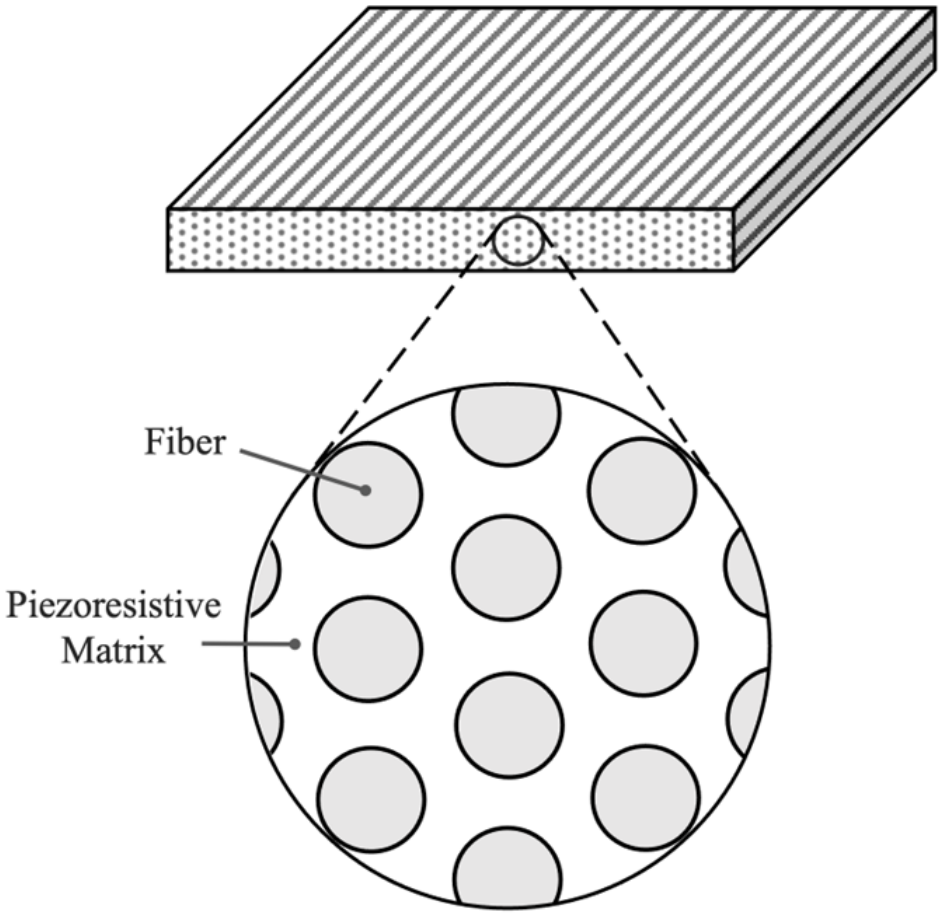

Figure 5.1. An FBC in a composite lamina is defined as a cluster of adjacent reinforcing continuous fibers encapsulated by a matrix phase. A FBC may be considered as a representative of a fiber-reinforced composite lamina.

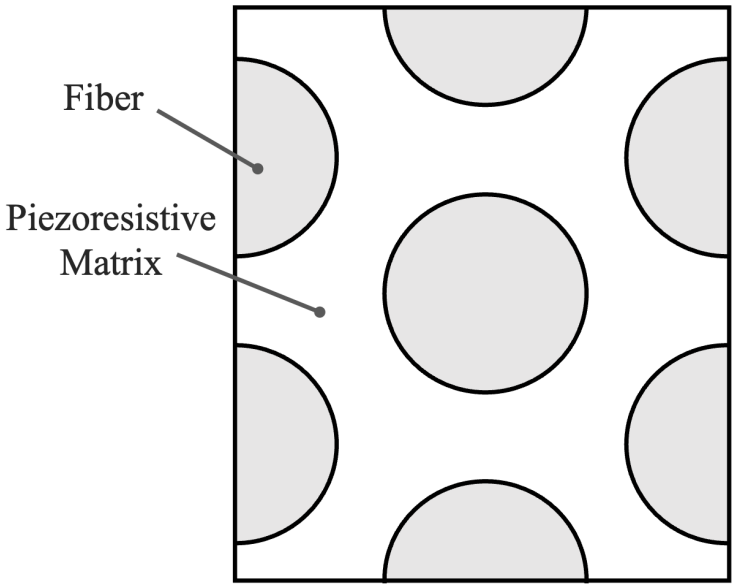

Figure 5.2. A schematic diagram representing the front-side view of the RVE used in the computational modeling of fiber-reinforced nanofiller-modified composites.

the nanofillers or the probability of electron tunneling between nanofillers. In contrast, our work focuses on a cluster of adjacent continuous fibers enveloped by a nanofiller-modified matrix phase. The mechanism of piezoresistivity within the conductive matrix is determined by the Koo and Tallman [113] resistivity-strain relationship. We assume that the fillers are evenly dispersed and that both phases (the continuous fiber and the matrix) are mechanically and electrically isotropic. This means that the electrical and mechanical properties of both the fiber and the matrix are considered to possess directional independence. It should be noted that we utilized ABAQUS, MATLAB, and Python programming language to conduct mechanical and electrical simulations. ABAQUS CAE served as the finite element solver, with Python being used via ABAQUS Scripting Interface (ACI) to manage ABAQUS operations and execute a series of sequential simulations. Meanwhile, MATLAB was utilized for creating electrical RVE models and conducting post-processing analysis on the finite element (FE) simulation results.

The general electrical and mechanical governing equations, in their strong and weak forms, and boundary conditions, as well as the effective resistivity and resistivity changes of the RVE are discussed next.

5.2.1 Electromechanical Governing Equations and Boundary Conditions

Mechanical Boundary Value Problem

In this subsection, we will delve into the mechanical and electrical governing PDEs. Initially, we will examine the macroscale governing PDEs in their strong forms, together with the related boundary conditions for the mechanical problem. Subsequently, these mechanical equations at the macroscale will be connected to the strong-form mechanical governing equations at the microscale. Given our approach to solving these problems via FEA, the weak forms will be established. In a similar manner, the electrical diffusion problem, along with its strong and weak forms at both the macro- and micro-levels, will be outlined. With the electromechanical coupling through piezoresistivity in mind, the FEA output from the mechanical problem will be linked to the electrical diffusion problem through elemental resistivity-strain relations, as we will explore later. It should be noted that, in the subse-

quent discussion, the Einstein notation is employed, where subscripts such as i, j, and k denote the indices of the coordinate system. Additionally, unless explicitly stated otherwise, the governing equations presented are applicable to both the matrix and fiber phases.

First, we begin by considering the mechanical governing equations at the macro- and microscales in their strong forms. To derive the strong-form governing equation in terms of displacements at the macroscale level and then relate it to the microscale level, we start by establishing the macroscale governing equation for an isotropic linear elastic material (since the constituents are assumed to be individually isotropic) under the assumption of small deformations. Following that, we link this to the microscale governing equation and derive the weak form at the microscale. For an isotropic linear elastic material, the governing equation in terms of displacement, U_{i}^{M}, at the macroscale can be derived from the equilibrium condition and Hooke's law. The equilibrium equation can be mathematically expressed as follows.

$$\sigma_{\mathrm{ij,j}}^{M} + F_{\mathrm{i}}^{M} = 0 \tag{5.1}$$

Above, commas denote differentiation, the superscript M indicates macroscale level, and F_{i}^{M} are external forces per unit volume at the macroscale, which is assumed to be zero for simplicity. Using Hooke's law for an isotropic material, the stress σ_{ij}^{M} is related to the strain $\varepsilon_{\mathrm{ij}}^{M}$, which is a function of displacement, as follows.

$$\sigma_{\mathrm{ij}}^{M} = \lambda \delta_{\mathrm{ij}} \varepsilon_{kk}^{M} + 2\mu \varepsilon_{\mathrm{ij}}^{M} \tag{5.2}$$

In the above equation, μ and λ are Lamé's constants, and δ_{ij} is the Kronecker delta. The macroscale strain is related to the macroscale displacement via the following relation.

$$\varepsilon_{\mathrm{ij}}^{M} = \frac{1}{2}\left(U_{\mathrm{i,j}}^{M} + U_{\mathrm{j,i}}^{M}\right) \tag{5.3}$$

By substituting the constitutive relations (after expressing the strains in terms of displacements) shown in equation (5.2) into the equilibrium equation, illustrated in equation (5.1),

the following Navier-Cauchy equation, which represents the governing equations in terms of displacements, is achieved.

$$\mu(U^M_{\mathrm{i,jj}} + U^M_{\mathrm{j,ij}}) + \lambda U^M_{\mathrm{j,ji}} = 0 \tag{5.4}$$

The above relation represents the strong form governing equation at the macroscale in terms of displacement. In general, we can define the following Dirichlet (displacement) and Neumann (traction) boundary conditions for the above PDE, as follows.

$$U^M_{\mathrm{i}} = \hat{U}^M_{\mathrm{i}}, \quad \text{defined on}\, \Gamma_U \tag{5.5a}$$

$$t^M_{\mathrm{i}} = \sigma^M_{\mathrm{ij}} n^M_{\mathrm{j}} = \hat{t}^M_{\mathrm{i}}, \quad \text{defined on}\, \Gamma_t \tag{5.5b}$$

$\hat{U}^M_{\mathrm{i}}$ and $\hat{t}^M_{\mathrm{i}}$ are the externally applied displacement and traction, respectively, on the macro level. Γ_U is the boundary of the domain where the Dirichlet BCs are imposed, whereas Γ_t is the boundary where the Neumann conditions are implemented. At the microscale level, the behavior of the material is described by a similar form of the governing equations but specific to the microscale structure. Using homogenization techniques, the microscale displacement field, U_{i}, is related to the macroscale displacement field, U^M_{i}, through the strain and stress fields, which are linked by volume averaging (denoted by the bar accents), as follows.

$$\sigma^M_{\mathrm{ij}}\left(X^M_k\right) = \bar{\sigma}_{\mathrm{ij}} \tag{5.6a}$$

$$\varepsilon^M_{\mathrm{ij}}\left(X^M_k\right) = \bar{\varepsilon}_{\mathrm{ij}} \tag{5.6b}$$

The above relations signify that the macroscale stress and strain at a macroscale point X^M_k are related to their microscale counterparts through volume averaging, which are refereed to by the bar accents. The governing equation in terms of displacements at the microscale-RVE level can be derived similarly to the macroscale but considering the microscale geometry and boundary conditions. Equation (5.7) below represents the strong form of the PDE at the microscale level.

$$\mu\left(U_{\mathrm{i,jj}} + U_{\mathrm{j,ij}}\right) + \lambda U_{\mathrm{j,ji}} = 0 \tag{5.7}$$

Note that the Neumann (traction) BCs of the above microscale PDE is defined as

$$t_{\mathrm{i}} = \sigma_{\mathrm{ij}}^{M}\left(X_{k}^{M}\right) n_{\mathrm{j}} \tag{5.8}$$

where $\sigma_{\mathrm{ij}}^{M}\left(X_{k}^{M}\right)$ presents the macroscale stress at a macroscale material point X_{k}^{M}, refer to equation (5.6a) above, and n_{j} represents the outward unit normal vector to the boundary of the RVE. The displacement boundary condition, on the other hand, is defined as follows.

$$U_{\mathrm{i}} = \varepsilon_{\mathrm{ij}}^{M}\left(X_{k}^{M}\right) x_{\mathrm{j}} \tag{5.9}$$

$\varepsilon_{\mathrm{ij}}^{M}\left(X_{k}^{M}\right)$ is the macroscale strain at the same macroscale material point X_{k}^{M}, refer to equation (5.6b) above, and x_{j} is a vector representing the local coordinates on the boundary of the RVE.

Next, we construct the weak form of the microscale PDE provided in equation (5.7) with its corresponding boundary conditions provided in equations (5.8) and (5.9). Knowing that both the matrix phase and the fiber phase are assumed to be isotropic, we first consider the stress-strain relation and the strain-displacement relation at the micro level, which are, respectively, as follows.

$$\sigma_{\mathrm{ij}} = \lambda \delta_{\mathrm{ij}} \varepsilon_{kk} + 2\mu \varepsilon_{\mathrm{ij}} \tag{5.10a}$$

$$\varepsilon_{\mathrm{ij}} = \frac{1}{2}\left(U_{\mathrm{i,j}} + U_{\mathrm{j,i}}\right) \tag{5.10b}$$

To derive the weak form, we start with the equilibrium equation in terms of stress at the microscale level, $\sigma_{\mathrm{ij,j}} = 0$, where σ_{ij} represents the microscale stress tensor, then, multiply this equation by an arbitrary weighting function, w_{i}, which vanishes on the Dirichlet boundary. We then integrate the obtained expression over the volume of the RVE, Ω, as follows.

$$\int_{\Omega} w_{\mathrm{i}}\, \sigma_{\mathrm{ij,j}}\, \mathrm{d}\Omega = 0 \tag{5.11}$$

To convert the problem into a form that is more suitable for computational modeling via FEA, apply the divergence theorem (integration by parts for tensor fields) to transfer the

derivative from the stress tensor onto the weighting function. This yields the following integral equation.

$$\int_{\Omega} \sigma_{\mathrm{ij}}\, w_{\mathrm{i,j}}\, \mathrm{d}\Omega - \int_{\Gamma_t} \sigma_{\mathrm{ij}}\, n_{\mathrm{j}}\, w_{\mathrm{i}}\, \mathrm{d}\Gamma_t = 0 \tag{5.12}$$

In the above equation, n_{j} represents the components of the normal vector to the boundary Γ_t of the RVE. The first term now represents the internal virtual work, and the second term represents the virtual work done by the traction boundary conditions. By making use of the stress-strain relations and the strain-displacement relations, illustrated in equations (5.10) along with considering the Neumann boundary condition shown in equation (5.8), which reflects the macro-to-micro scale transition, and the Dirichlet boundary condition presented in equation (5.9), which reflects the prescribed macroscale strains, we have the following expression.

$$\int_{\Omega} \left[\lambda\, \delta_{\mathrm{ij}}\, U_{k,k} + \mu\, \left(U_{\mathrm{i,j}} + U_{\mathrm{j,i}}\right)\right] w_{\mathrm{i,j}}\, \mathrm{d}\Omega - \int_{\Gamma_t} \sigma_{\mathrm{ij}}^{M}\left(X_k^M\right)\, n_{\mathrm{j}}\, w_{\mathrm{i}}\, \mathrm{d}\Gamma = 0 \tag{5.13}$$

This equation represents the weak form of the microscale equilibrium equation, incorporating the influence of macroscale stress and strain fields through the boundary conditions. It sets the foundation for finite element analysis, where both the displacement field, U_{i}, and the weighting function, w_{i}, can be approximated using shape (test) functions.

Electrical Boundary Value Problem

Now, we consider the macroscale and microscale governing equations in their strong forms for the electrical diffusion problem. Analogous to the mechanical problem, the governing differential equation representing steady-state electrical diffusion at the macroscale is defined as follows.

$$J_{\mathrm{i,i}}^{M} = 0 \tag{5.14}$$

In the above equation, J_{i}^{M} is the current density vector at the macroscale level. The electric field, E_{i}^{M}, is related to the potential, ϕ^{M}, which is the primary variable here (analogous to the displacement in the case of a mechanical problem), through the following relation.

$$E_{\mathrm{i}}^{M} = -\phi_{,\mathrm{i}}^{M} \tag{5.15}$$

Note that compared to the primary field in the mechanical boundary value problem (BVP), which is the displacement vector, the primary field here, which the the potential, is a scalar field. The constitutive relation, which is also known as the continuum form of Ohm's law, for the electrical BVP at the macro level is

$$E_{\mathrm{i}}^{M} = \rho_{\mathrm{ij}}^{M} J_{\mathrm{i}}^{M} \tag{5.16}$$

where ρ_{ij}^{M} represents the effective macroscale resistivity, determined through the application of the conservation of energy principle, a topic that will be elaborated on later. We can use equations (5.14) to (5.16) to derive the following electrical PDE that governs the electrical diffusion BVP at the macroscale level.

$$\phi_{,\mathrm{ii}}^{M} = 0 \tag{5.17}$$

The above equation, which is the Laplacian of the scalar field ϕ^{M}, represents the strong form governing equation at the macroscale level in terms of the potential while assuming that the effective resistivity, ρ_{ij}^{M}, is constant throughout the macroscale structure. In general, we can define the following Dirichlet (potential) and Neumann (current density) boundary conditions for the above PDE.

$$\phi^{M} = \hat{\phi}^{M}, \quad \text{defined on } \Gamma_{\phi} \tag{5.18a}$$

$$J_{\mathrm{i}}^{M} n_{\mathrm{i}}^{M} = \hat{J}_{\mathrm{i}}^{M} n_{\mathrm{i}}^{M}, \quad \text{defined on } \Gamma_{J} \tag{5.18b}$$

For the macroscale structure, $\hat{\phi}_{\mathrm{i}}^{M}$ represents the externally applied potential and $\hat{J}_{\mathrm{i}}^{M}$ denotes the current density vector. Furthermore, Γ_{ϕ} and Γ_{J} are the boundaries where the Dirichlet (potential) and Neumann (current density) conditions are imposed, respectively. The microscale governing equations are developed in the same fashion as in the macroscale case, comparable to the mechanical BVP. The relation between the microscale electric field, denoted as E_{i}, and the macroscale electric field, denoted as E_{i}^{M}, as well as the relation between the microscale and macroscale current densities, denoted as J_{i} and J_{i}^{M}, respectively, can be determined through the use of homogenization techniques as follows.

$$E_{\mathrm{i}}^{M}\left(X_{k}^{M}\right)=\bar{E}_{\mathrm{i}} \tag{5.19a}$$

$$J_{\mathrm{i}}^{M}\left(X_{k}^{M}\right)=\bar{J}_{\mathrm{i}} \tag{5.19b}$$

The above relations signify that the macroscale electric field and current density at a macroscale point X_{k}^{M} are related to their microscale counterparts through volume averaging, which are referred to by the bar accents. We can now write the microscale strong-form electrical diffusion PDE as follows.

$$\phi_{,\mathrm{ii}}=0 \tag{5.20}$$

Note that the Neumann (current density) boundary condition of the above microscale PDE is defined in equation (5.21a) below, whereas the Dirichlet BC is defined in equation (5.21b).

$$J_{\mathrm{i}}\, n_{\mathrm{i}}=J_{\mathrm{i}}^{M}\left(X_{k}^{M}\right) n_{\mathrm{i}} \tag{5.21a}$$

$$\phi=E_{\mathrm{i}}^{M}\left(X_{k}^{M}\right) x_{\mathrm{i}} \tag{5.21b}$$

Both $J_{\mathrm{i}}^{M}\left(X_{k}^{M}\right)$, and $E_{\mathrm{i}}^{M}\left(X_{k}^{M}\right)$ are defined above in equations (5.19).

Similar to the previously mentioned mechanical BVP, our objective is also to derive the weak form of the microscale PDE provided in equation (5.20) with its corresponding boundary conditions shown in equations (5.21). It should be emphasized that deriving the weak form for the electrical diffusion problem involves a process similar to the mechanical problem, but adapted for a scalar potential field while considering the electrical properties of

the material, instead of the elastic ones. Given the PDE that governs the electrical diffusion problem on the microscale, which is in equation (5.20), we multiply both sides by a scalar weighting function w and integrate over the domain Ω, so that we can arrive at the following expression.

$$\int_{\Omega} w\, \phi_{,\mathrm{ii}}\, \mathrm{d}\Omega = 0 \tag{5.22}$$

Again, we apply integration by parts to move the derivation from the primary variable ϕ to the weighting function, as follows.

$$-\int_{\Omega} w_{,\mathrm{i}}\, \phi_{,\mathrm{i}}\, \mathrm{d}\Omega + \int_{\Gamma_J} w\, \phi_{,\mathrm{i}}\, n_{\mathrm{i}}\, \mathrm{d}\Gamma_J = 0 \tag{5.23}$$

Here, Γ_J represents the boundary of the domain Ω where the Neumann condition is imposed, and n_{i} is the outward normal vector at the boundary. The given Neumann boundary condition, illustrated in equation (5.21a), can be directly incorporated into the weak form as follows.

$$-\int_{\Omega} w_{,\mathrm{i}}\, \phi_{,\mathrm{i}}\, \mathrm{d}\Omega + \int_{\Gamma_J} w J^M_{\mathrm{i}} n_{\mathrm{i}}\, \mathrm{d}\Gamma = 0 \tag{5.24}$$

This above equation represents the weak form of the electrical diffusion problem at the microscale-RVE level, incorporating the influence of macroscale current density and electric fields through the boundary conditions. It establishes the foundation for finite element analysis, where both the potential field, ϕ and the scalar weighting function w can be approximated using shape functions.

Electromechanical Coupling Effect

Due to the piezoresistive effect, the output of the mechanical BVP influences the electrical properties of the composite in the electrical BVP. This relationship is caused by the inclusion of nanofillers into the matrix, which leads to a conductive matrix phase that changes its electrical characteristic (resistivity/conductivity) as a function of the local strain. Therefore, we consider the local elemental strain tensor, obtained by solving the mechanical BVP using the ABAQUS FE solver, to calculate the elemental conductivity value. The resistivity-strain tensor-based relation developed by Koo and Tallman [113] for predicting the resistivity

changes as a function of strain in nanofiller-modified composites is adopted throughout our computational analysis. The relation can be expressed for calculating the elemental resistivity changes as follows:

$$\Delta\rho^{m}_{elm} = \kappa\,\varepsilon^{elm}_{\mathrm{ii}} + \Pi_1\,\varepsilon^{elm}_{\mathrm{ii}}\,\varepsilon^{elm}_{\mathrm{jj}} + \Pi_2\,\varepsilon^{elm}_{\mathrm{ij}}\,\varepsilon^{elm}_{\mathrm{ij}} \tag{5.25}$$

Above, κ, Π_1, and Π_2 represent experimentally determined piezoresistive constants, and their values can be found in [113] for a given CNF weight fraction. Also note that in the above relation, we have added the subscript and superscripts elm to emphasize that this relation is at the element level, that is, $\Delta\rho^{m}_{elm}$ is the change in the resistivity of an element in the conductive matrix due to the local element strain tensor $\varepsilon^{elm}_{\mathrm{ij}}$. Additionally, it is noteworthy to mention that the strain tensors derived from ABAQUS are computed at the centroid of each element, individually. To clarify, the software calculates the values of strain tensor components supposing that they are concentrated in the geometric center of the element. This procedure entails calculating the average or extrapolating the values from the integration points, where the governing equations are numerically integrated, to the centroid of the element.

Periodic Boundary Conditions

In the context of micromechanical analysis, it is typical to examine a small portion of a composite material, assuming that it comprises a significant number of repeated microscale units (i.e., RVEs). The properties exhibited by an individual RVE can be regarded as indicative of the overall behavior of the composite at the macroscale. Periodic boundary conditions (PBCs) are frequently introduced to the boundaries of the analyzed RVE in order to ensure that the obtained results are equivalent to those at a macroscale [127]. The idea of imposing PBCs is that a composite material at the macroscale level can be thought of as a series of connected RVEs such that each adjacent RVE does not overlap, as they experience identical deformation patterns. In other words, the deformation or displacement pattern on one face of the RVE should match the pattern on the opposite face in a way that if you were to "tile" multiple copies of the RVE next to each other in space, the pattern

of deformation (or material behavior) would appear seamless across the boundaries. As a result, the displacement field on one side of a cuboid-shaped RVE is equivalent to that on the opposite side, ensuring continuity and allowing the RVE to represent an infinite medium by repeating in all directions. Moreover, the traction fields on these two opposing faces must also be equivalent. In essence, the use of PBCs enables the approximation of an infinite system through the utilization of a small unit, resulting in a significant reduction in computing expenses.

Taheri-Behrooz and Pourahmadi [128] have investigated the development of a three-dimensional cuboid-shaped periodic RVE to find the effective mechanical properties of heterogeneous composites using PBCs. They found that to hold the PBCs, the displacement fields, U_{i}, of two opposing parallel pairs of boundaries must obey the following relation.

$$U_{\mathrm{i}}^{q+} - U_{\mathrm{i}}^{q-} = \bar{\varepsilon}_{\mathrm{i}k} \left(x_k^{q+} - x_k^{q-} \right) \tag{5.26}$$

Above, the superscripts $q+$ and $q-$ refer to the fields that belong to the qth pair of the RVE boundaries that are parallel and opposing each other. Moreover, in equation (5.26) above, $\bar{\varepsilon}_{\mathrm{i}k}$ refers to the average strain, while $\left(x_k^{q+} - x_k^{q-} \right)$ is the perpendicular distance between the two opposite parallel pairs. In a cuboid RVE, this distance is constant, which means that it represents a spatial dimension of the RVE and can be expressed as l_k^q, where $l_k^q = \left(x_k^{q+} - x_k^{q-} \right)$. For more details on the development of PBCs and their implications, the reader is encouraged to read reference [128].

Based on the above discussion, we impose periodic conditions in our electromechanical computational FEA model. First, it is important to mention that a Python code developed by Heule [129] is used in our simulations to impose PBCs on the RVE. The code creates a user-friendly plugin on ABAQUS CAE such that the user can easily apply PBCs to three-dimensional RVEs by defining pairs of parallel opposing surfaces called master-slave pairs. This significantly simplifies the application process, as manually linking each pair of nodes would be nearly impossible without such a Python code. Specifically, the pairing process in ABAQUS requires creating constraint equations for each pair of nodes, which is now automated by the code, highlighting its power and the ease it brings for implementing

PBCs. The code, however, mandates that the mesh exhibit periodicity. In other words, a master surface can be paired with an opposing slave surface exclusively if both surfaces share an identical meshing pattern. This requirement ensures that each node on the master surface is paired with a corresponding node on the slave surface possessing identical in-plane coordinates. In addition, it is worth mentioning that since we also conduct electrical diffusion simulations, the original Python code was modified so that it can impose potential PBCs, instead of just displacement PBCs, as the code was originally developed. The electrical PBCs will have a format similar to that of the displacement PBCs described in equation (5.26), which is as follows.

$$\phi^{q+} - \phi^{q-} = E_0 \left(x_k^{q+} - x_k^{q-} \right) = E_0 \, l_k^q \tag{5.27}$$

Note the similarity between the PBC relations described above, as shown in equations (5.26) and (5.27), and those defined by Ren and Seidel [83]. An important difference, however, is that their PBCs are defined for two-dimensional planar RVEs, whereas in our analysis, we adapt the same formats, but tailor them for a three-dimensional analysis.

5.2.2 Effective RVE Resistivity and Resistivity Changes

Following the electromechanical simulations, we determine the effective resistivity of the RVE and subsequently characterize the changes in resistivity due to deformations, as demonstrated in this subsection. To find the effective resistivity of the composite at a certain state of strain, the concept of energy equivalence between the heterogeneous RVE and a hypothetical homogeneous material subjected to the same boundary conditions is considered [83]. This is a similar approach to the one discussed earlier in Chapter 4, particularly the principle of electrical energy conservation discussed in equations (4.42) through (4.44), where we defined a quantity called the volume power density w. We begin by assuming that the volumetric average of the volume power density in the RVE is equal to that of the homogeneous

material, that is, $\bar{w}^{RVE} = \bar{w}^{H}$, where the volume power density is calculated as $w = J_{\mathrm{i}} E_{\mathrm{i}}$. This indicates the following relation.

$$\bar{J}_{\mathrm{i}}^{RVE}\, \bar{E}_{\mathrm{i}}^{RVE} = \bar{J}_{\mathrm{i}}^{H}\, \bar{E}_{\mathrm{i}}^{H} \tag{5.28}$$

Then, since both systems are subjected to the same BCs, they experience equal average internal electric fields, $\bar{E}_{\mathrm{i}}^{RVE} = \bar{E}_{\mathrm{i}}^{H}$. As a result, from equation (5.28) above, they also have equal average current density vectors, $\bar{J}_{\mathrm{i}}^{RVE} = \bar{J}_{\mathrm{i}}^{H}$. From the continuum form of Ohm's law, we can deduce that the averages of the electric field and the current density vector in the homogeneous composite are related via the next relation.

$$\bar{E}_{\mathrm{i}}^{H} = \rho_{\mathrm{ij}}^{c} \bar{J}_{\mathrm{j}}^{H} \tag{5.29}$$

In the above expression, ρ_{ij}^{c} is the effective composite resistivity. Due to the energy equivalence between the RVE and the homogeneous material, the above expression becomes as follows.

$$\bar{E}_{\mathrm{i}}^{RVE} = \rho_{\mathrm{ij}}^{c} \bar{J}_{\mathrm{j}}^{RVE} \tag{5.30}$$

which indicates that the effective resistivity of the composite is found by considering the volumetric averages of the electric field and the current density.

Throughout our analysis, we assume that the composite material making the RVE is electrically transversely isotropic, where the z-axis (parallel to the fiber direction) is the axis of symmetry. This implies that the resistivity tensor of the RVE becomes as follows.

$$\rho^{RVE} = \begin{bmatrix} \rho_x^{RVE} & 0 & 0 \\ 0 & \rho_y^{RVE} & 0 \\ 0 & 0 & \rho_z^{RVE} \end{bmatrix} \tag{5.31}$$

Since the material is assumed to be electrically transversely isotropic, the resistivity values in the transverse directions are equal as $\rho_x^{RVE} = \rho_y^{RVE} = \rho_2^{RVE}$. The axial resistivity, on the other hand, is not equal to the transverse one and will be denoted throughout this chapter

as $\rho_z^{RVE} = \rho_1^{RVE}$. It can be easily proved, using tensor transformations, that the resulting resistivity values obtained here for the RVE, which are defined in the Cartesian coordinates, can be directly compared to the ones that were calculated via the analytical CCA model, which were defined in the cylindrical coordinate, as long as both the CCA model and the RVE model are subjected to identical strain states.

We can apply the findings of the principle of energy conservation discussed above in the context of finite element analysis to determine the effective resistivity of the RVE. It should be mentioned first that, similar to the strain field that was the output of the mechanical BVP, each element has a single vector representing the current density and another vector representing the electric field. Both are defined at the centroid of an element. Consequently, the effective resistivity along a specific direction is determined by calculating the volumetric average of the electric field across all elements in the relevant direction within the RVE. This value is then divided by the volumetric average of the elemental current density along the same direction. This can be expressed mathematically as follows.

$$\rho_s^{RVE} = \frac{\bar{E}_{\mathrm{i}}^{RVE}}{\bar{J}_{\mathrm{i}}^{RVE}} \tag{5.32}$$

Since we are considering an electrically transversely isotropic composite, the subscript s is used to distinguish between the resistivity directions such that $s = 1$ refers to the axial resistivity, which is the resistivity in the direction parallel to the reinforcing fiber direction, whereas $s = 2$ refers to the transverse resistivity, which is the resistivity in the direction perpendicular to the reinforcing fiber direction. To calculate the volumetric average of the electric field across all elements along the ith direction within the RVE, the following relation is used.

$$\bar{E}_{\mathrm{i}}^{RVE} = \frac{1}{\sum_{k=1}^{n} V_k} \sum_{k=1}^{n} \left(E_{\mathrm{i}}^{(k)} V_k \right) \tag{5.33}$$

In the above summations, n is the total number of elements, and V_k is the volume of the kth element. Similarly, the volumetric average of the current density across all elements along the ith direction within the RVE is calculated using the following relation.

$$\bar{J}_{\mathrm{i}}^{RVE} = \frac{1}{\sum_{k=1}^{n} V_k} \sum_{k=1}^{n} \left(J_{\mathrm{i}}^{(k)} V_k \right) \tag{5.34}$$

Note that in the above equations, $E_{\mathrm{i}}^{(k)}$ is the electric field value in the ith direction of the kth element, and $J_{\mathrm{i}}^{(k)}$ is the current density value in the ith direction of the kth element.

Once the effective resistivity of the RVE is found for a certain strain state, the change in the resistivity of the RVE can be calculated as follows.

$$\Delta\rho_s^{RVE} = \rho_{ds}^{RVE} - \rho_{0s}^{RVE} \tag{5.35}$$

In the above equation, the subscripts d and 0 refers to the deformed and the undeformed RVEs, respectively. In other words, ρ_{ds}^{RVE} is the resistivity of the RVE (either axial or transverse resistivities) after deformation, whereas ρ_{0s}^{RVE} is the effective resistivity of the RVE free from deformations.

5.3 Simulation Procedure

ABAQUS CAE Research Edition was used to simulate mechanical and electrical BVPs with the aid of MATLAB, which was used for data preparation and post-processing, and the Python programming language via ASI, which was utilized to control and perform sequential simulations. Details, such as the preparation of the FE model (i.e., properties of the used materials, meshing, boundary conditions, etc.), the procedure followed for conducting the electromechanical simulations, and post-processing of the obtained data are discussed in this section.

To start the FE simulation, we construct a three-dimensional cuboid RVE, representing fiber-reinforced nanofiller-modified composites. The three-dimensional RVE has a pattern inspired by that adopted by Ren and Seidel [83], where they used a two-dimensional hexagonal array RVE to model CNT-polymer composites and predict transverse properties. However,

our RVE differs in that it is a three-dimensional extruded version of the RVE they utilized. This is due to the presence of a nanofilled-modified matrix that exhibits a piezoresistivity property, which surrounds the continuous fibers, as opposed to a pure matrix surrounding the nanofillers, as observed in their RVE. The extruded length or depth of the RVE, L_z, which is the z-axis dimension that is parallel to the fiber phase direction, is assumed to be 20 μm. Note that since we are going to assume PBCs, the depth can be relatively short, minimizing the computational cost, as we are more interested in the inter-fiber interactions in the lateral direction, which is perpendicular to the fiber direction, rather than the depth direction. The other dimensions, that is, the length along the x-axis L_x and the height along the y-axis L_y, are determined based on the fiber volume fraction, according to the following relations derived from the geometric properties of an RVE with fibers arranged in a hexagonal packing pattern.

$$L_y = 4\,a\sqrt{\frac{\pi}{2\sqrt{3}V_f}} \tag{5.36a}$$

$$L_x = L_y\,\cos 30^\circ \tag{5.36b}$$

Above, a refers to the radius of the fiber, and V_f, in this context, is the intended fiber volume fraction within the composite.

After building the RVE in ABAQUS, it is necessary to assign the electrical and elastic properties of the composite constituents. Each constituent, whether the continuous fiber or the conductive matrix, is presumed to be electrically and elastically isotropic, mirroring our assumptions in the CCA analysis. Furthermore, we intend to attribute mechanical and electrical properties to these constituents that are analogous to those utilized in our analytical CCA model, as our goal is to compare the outcomes of both models. For additional details on the properties of the fiber and the matrix used in our FE analysis, see Table 3.1. It should be noted that the matrix in this case is a CNF-modified epoxy containing 1 wt.% CNFs, and the piezoresistive constants, as presented in equation (5.25), are $\kappa = 4.10\,k\Omega\cdot m$, $\Pi_1 = -150\,k\Omega\cdot m$, and $\Pi_2 = 5.15\,k\Omega\cdot m$ [113]. Additionally, to conserve computational time and resources (since running RVEs with PBCs is extremely computationally intensive), we use the same RVE, constructed at a specific fiber volume fraction, irrespective of the fiber type. In essence, there is a single RVE for each fiber volume fraction, which possess

a defined fiber radius, to which we assign the elastic and electrical properties of glass or carbon fibers based on the analysis at hand. This approach still yields valid outputs, such as the strain tensor, which is the desired outcome from the mechanical simulations, and effective composite resistivity at any strain state, since these do not directly depend on the fiber radius, but rather on the fiber volume fraction. Consequently, the fiber radius in the constructed RVEs is fixed at 7.5 μm, while the RVE dimensions are determined using equations (5.36) for a specified fiber volume fraction. This strategy is adopted to avoid the complexities of conducting multiple convergence analyses (i.e., conducting one convergence analysis for each fiber volume fraction instead of two for each fiber volume fraction if an RVE is constructed for every fiber type) to identify the optimal mesh size.

Subsequently, the RVE is meshed and PBCs are assigned. During the meshing process, we adhere to the meshing requirement stipulated by Heule's PBCs Python code [129], which mandates that the mesh patterns be periodic. With this requirement in mind, the RVE is meshed using a three-dimensional, 8-node linear brick element, referred to as element type C3D8 in ABAQUS. For an illustration of what the resulting meshed part looks like, refer to Figure 5.3, which displays a meshed RVE with a 60% fiber volume fraction. It is important to note that partitioning techniques are employed to ensure periodic and systematic mesh patterns across the boundary surfaces of the RVE, guaranteeing that any master-slave pair of surfaces would have matching mesh patterns. Furthermore, given our focus on the mechanical response of the conductive matrix, since we use the resulting strain tensor of the matrix elements to determine the elemental resistivity changes according to equation (5.25), the meshing is more refined in the matrix region compared to the fiber regions. Moreover, since we focus more on the transverse interaction between the fibers and the matrix, the elements are coarser in the z-axis direction. This approach reduces computational costs, while still enabling us to obtain more accurate results for the matrix resistivity changes. After the part is meshed, displacement PBCs are implemented using the user-friendly ABAQUS plugin developed by the aforementioned Python code.

Mesh convergence analyzes are performed for each RVE. The parameter chosen for the mesh convergence study is the total elastic strain energy of the matrix elements, calculated directly by ABAQUS (referred to as ELSE) for each element in its centroid. The total elastic

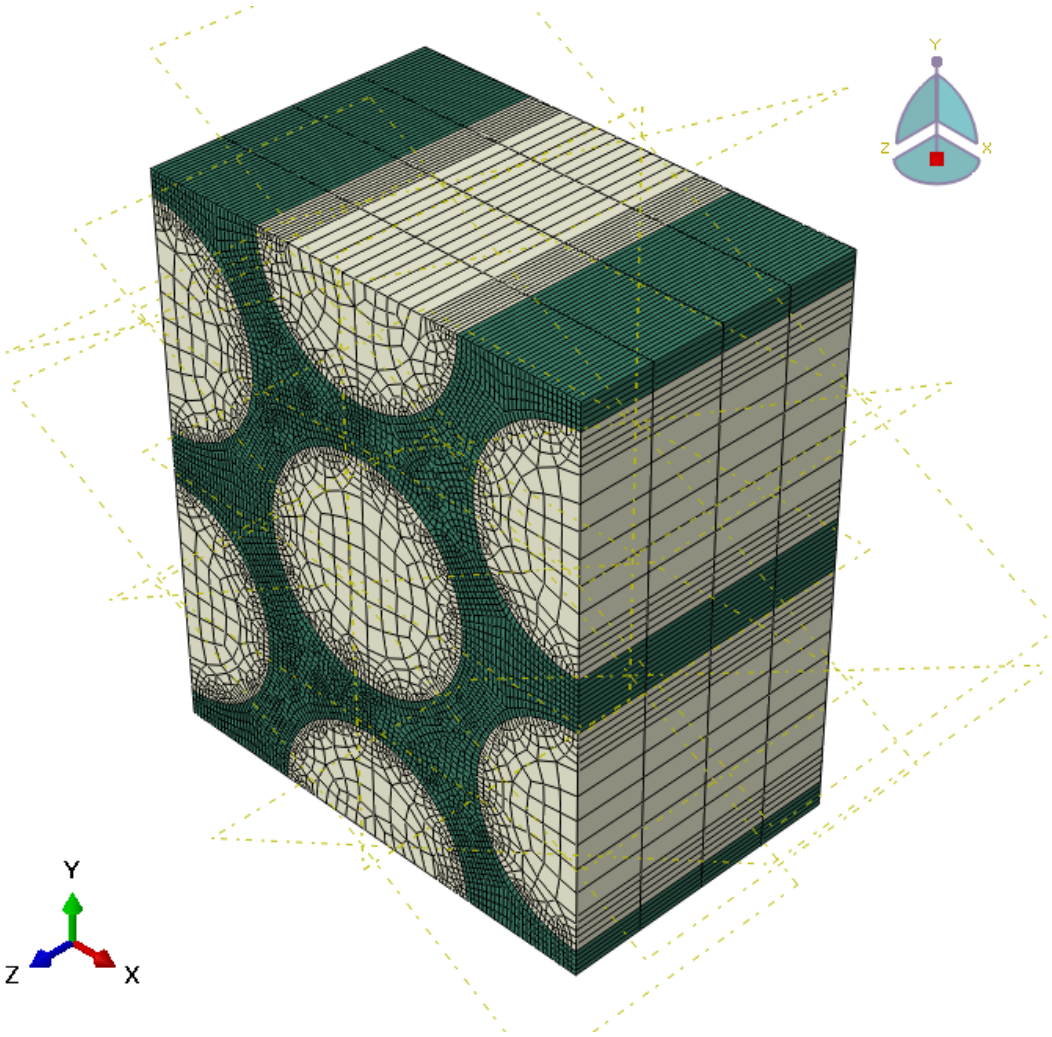

Figure 5.3. A view of a three-dimensional RVE built on ABAQUS to simulate fiber-reinforced composite laminae with 60% fiber volume fraction.

strain energy, U, is generally defined by the integral of the dot product of the stress tensor, σ_{ij}, and the strain tensor, ε_{ij}, over the volume V. This energy represents the work done by stress to induce strain in a material under elastic deformation conditions, and it has the following mathematical formula.

$$U = \frac{1}{2} \int_V \sigma_{ij} \, \varepsilon_{ij} \, dV \tag{5.37}$$

Table 5.1. Number of matrix elements used for RVEs at specified fiber volume fractions based on the convergence analysis.

Fiber Volume Fraction	**20%**	**40%**	**60%**	**80%**
Number of Matrix Elements	22,628	17,064	14,200	13,692

The mesh size is set when the average elastic strain energy of the matrix, which is subjected to an external axial strain of 6 mε and averaged over all matrix elements, converges. Figure 5.4 illustrates the convergence of the average, maximum, and minimum matrix element strain energy, measured in $N \cdot \mu m$, as the mesh becomes finer with an increasing number of matrix elements in the RVE. The number of matrix elements used for each RVE constructed at a specified fiber volume fraction is detailed in Table 5.1. It is important to emphasize that the selection of these mesh sizes aimed to achieve as accurate results as possible, since a specific number of elements had to be chosen initially, while still allowing the analysis to proceed with limited computational resources. Despite these chosen numbers of elements, the computational resources (computer processor power and memory size) were sufficient to perform FE calculations using a combination of a standard desktop PC and a stand alone high-performance computer (HPC).

Next, strains are applied at the RVE boundary in two different directions, individually. These external strains are axial strain in the fiber direction and radial strains applied by imposing a specific group of displacement boundary conditions, as shown in Figure 5.6. More details about these strains will be discussed later in the upcoming section. Each RVE is subjected to incremental strains ranging from a negative value representing compression to a positive strain with the same value representing tension, e.g., axial strains ranging from -6 to 6 mε. This enables us to determine the resistivity's variation with strain. After conducting mechanical simulations for a specific RVE, the elemental strain tensors, computed using ABAQUS, are obtained and stored for future use in determining the conductivity values of each element in the piezoresistive deformed matrix using equation (5.25) on MATLAB.

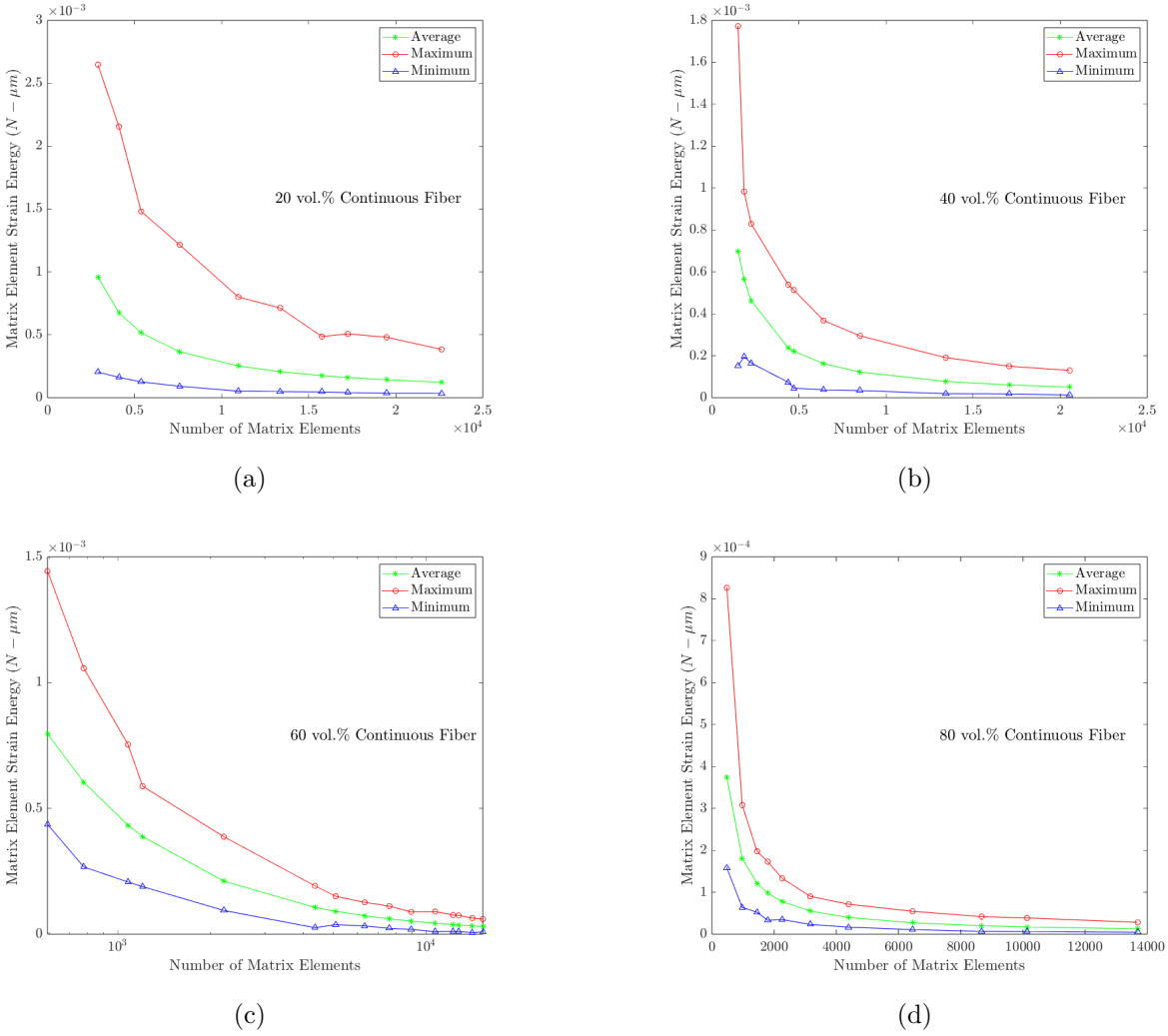

Figure 5.4. Illustration of the convergence of average, maximum, and minimum matrix element strain energies, measured in $N \cdot \mu m$, for RVEs with increasing numbers of matrix elements at fiber volume fractions of (a) 20%, (b) 40%, (c) 60%, and (d) 80%. The plots highlight the mesh refinement effect on the precision of strain energy calculations within the composite material.

Once the mechanical simulation is completed, the same meshed RVE, which has the same electrically isotropic constituents, is used again to conduct an electrical diffusion simulation and find the base effective resistivity of the composite. Similar to the mechanical BVP, we impose electrical PBCs, as illustrated in equation (5.27), using a modified version of the Heile Python code [129], as previously stated. After that, we apply electric field BCs in either the axial direction to observe the axial piezoresistivity effect, or in the transverse direction (y-direction) to observe the transverse piezoresistivity effect. The outcomes of this electrical simulation are the elemental current density and the electrical field vectors. The values of these vectors are then used to calculate the effective resistivity of the undefromed composite in the sth direction, ρ_{0s}^{RVE}, using equations (5.32) through (5.34).

After completing the aforementioned simulation, we utilize the input file generated by ABAQUS and modify it using MATLAB to prepare a second round of simulations that represent electrical diffusion in deformed RVEs, where each element (within the matrix) is now assigned a specific conductivity value. It is worth mentioning that an input file for ABAQUS is a text document containing all necessary instructions and data for ABAQUS to run a simulation. This document outlines the finite element model in a format readable by ABAQUS, including model geometry, material properties, boundary conditions, loads, analysis steps, and output requests. Returning to our task, as specific conductivity values are assigned for each element within the matrix phase, a non-uniform conductivity distribution within the matrix is observed, in contrast to the CCA analytical model case. Figure 5.5 illustrates the conductivity distribution within the matrix phase of a glass fiber composite with a fiber volume concentration of 60%, when the composite is subjected to an axial tensile strain of 6 mε.

To designate a certain conductivity value for each matrix element, we begin by modifying the previously generated input file using MATLAB. This enables us to retain the same meshed RVE with the same electrical BCs as used in the first electrical simulation for the undeformed RVE, in which the matrix had a single conductivity value. This modification produces a set of input files, each representing an RVE deformed by a predefined externally applied strain increment. In each of these newly created input files, a unique conductivity value is assigned to each element of the matrix phase. This value is calculated using

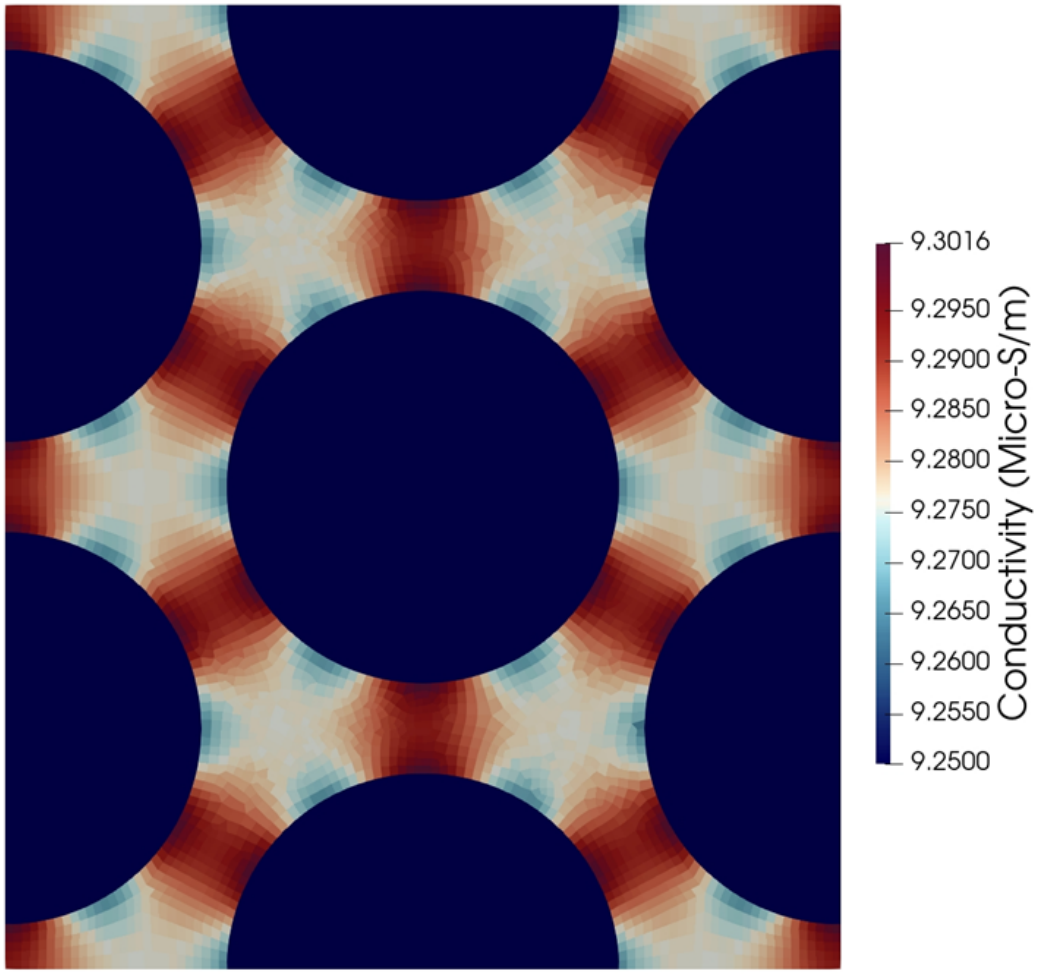

Figure 5.5. Conductivity distribution in μS/m within the matrix phase of a glass fiber-reinforced CNF-modified composite subjected to +6 mε. Note that the scale on the right-hand side does not incorporate the conductivity of the glass fibers, as it they have extremely low conductivity values compared to that of the piezoresistive matrix.

equation (5.25), based on the strain tensor of the element derived from the mechanical simulation. These input files are then used to perform electrical simulations to determine the effective resistivity at each strain increment along the sth direction, ρ_{ds}^{RVE}. Ultimately, using equations (5.32) through (5.35), we computationally derive the change in resistivity of the fiber-reinforced nanocomposite under various types of external deformation.

5.4 Comparison Between Analytical and Computational Approaches

Throughout this section, the results obtained from the analytical CCA model and the computational FE model for piezoresistivity are compared for glass fiber and carbon fiber-reinforced nanofiller-modified epoxy composites. The purpose of this comparative study is to verify our analytical model by directly comparing its results with those of the computational model. Furthermore, comparison of the output of the computational model provides valuable insight into the accuracy and possible limitations of the single-level piezoresistive predictions generated by the developed CCA model, especially for predicting the piezoresistivity of laminae where multiple fibers are tightly packed.

The methodology involves the following steps: Initially, we examine CNF epoxy composites reinforced with glass and carbon fibers, whose mechanical and electrical properties are listed in Table 3.1. The matrix phase is considered to be epoxy modified with 1 wt.% CNFs, characterized by piezoresistive constants that were mentioned in the previous section. Following the established simulation procedure, two types of strain are considered. These strains are applied to both the CCA (analytical) and the RVE (computational) systems: axial strain applied along the fiber direction and transverse strain applied radially in the plane perpendicular to the fiber direction. The transverse strain is chosen to be applied radially because the CCA system is predefined in the cylindrical coordinate. Having transverse deformations along the radial direction is more computationally convenient for cylindrical systems. It is important to mention that to make the outcomes of the cylindrical system and the RVE comparable, particularly for radial deformations, we need to apply displacements in the radial direction on the RVE such that the average internal radial strain within the RVE equals the average internal radial strain within the CCA model. This is to ensure that the internal impact of any externally applied radial displacement on the outer surface of the CCA, which is applied directly and solely on the matrix phase, is equivalent to the internal impact of any externally applied radial displacement on the outer surface of the RVE, which, unlike the CCA, contains both the matrix and fiber phases. This is clearly demonstrated in Figure 5.6, where the external radial displacement on the CCA is *not* equal to that on the RVE, i.e., $U_r^{ext,CCA} \neq U_r^{ext,RVE}$. However, the volumetric averages of the internal radial

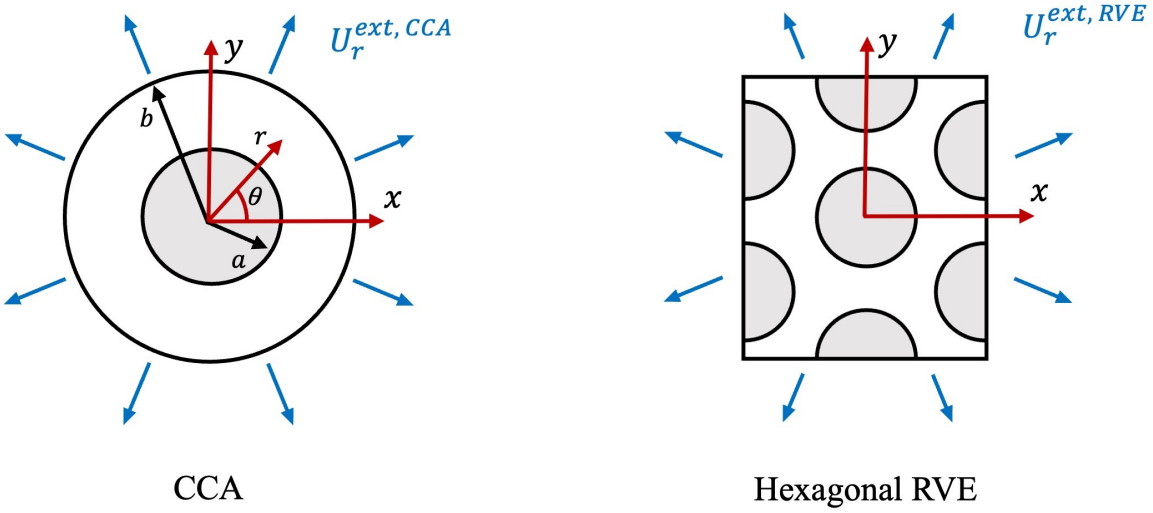

Figure 5.6. Radial Displacements applied on the outer surface of the CCA and the RVE.

strains within both systems must be the same, that is, $\bar{\varepsilon}_{rr}^{CCA} = \bar{\varepsilon}_{rr}^{RVE} = \bar{\varepsilon}_{rr}$. Since the RVE is defined in the Cartesian coordinate system, the in-plane transverse displacements, which are in the x and y-directions, can be related to the radial displacement as follows.

$$U_x = U_r \cos\theta, \quad U_y = U_r \sin\theta \tag{5.38}$$

Note that the radial strain of a point in a space with an r-coordinate is related to the radial displacement by the following relation: $\varepsilon_{rr} = U_r/r$, where r is related to the x- and y-coordinates of that point as follows: $r = \sqrt{(x^2 + y^2)}$. Therefore, the following x and y displacements are applied to the RVE such that $\bar{\varepsilon}_{rr}^{CCA} = \bar{\varepsilon}_{rr}^{RVE} = \bar{\varepsilon}_{rr}$.

$$U_x^{ext,RVE} = r\,\bar{\varepsilon}_{rr}\,\cos\theta \tag{5.39a}$$

$$U_y^{ext,RVE} = r\,\bar{\varepsilon}_{rr}\,\sin\theta \tag{5.39b}$$

Additionally, the effect of fiber volume fraction on the discrepancy between the two models is investigated.

To remain within the limits of the Koo and Tallman relation, as discussed in Chapter 4, displacements are applied in the radial direction such that the resulting internal radial strains, $\bar{\varepsilon}_{rr}$, fall within the specified limits. Therefore, the changes in axial and transverse resistivity are plotted as functions of internal radial tensile or compressive strains of ± 0.2, ± 0.6, ± 1, and ± 1.4 mε. Given that the fibers withstand most of the stress, resulting in smaller matrix strains, higher axial strain values of ± 1, ± 2, ± 3, ± 4, ± 5, and ± 6 mε are imposed. The resistivity changes in the longitudinal and lateral directions are plotted as functions of the externally imposed axial strain.

The piezoresistive characteristics of glass fiber and carbon fiber-reinforced nanocomposites can be inferred from Figures 5.7 and 5.8, which depict axial and transverse resistivity changes resulting from deformations along the fiber direction. Furthermore, Figures 5.9 and 5.10 demonstrate the axial and lateral piezoresistivity of these composites under radial strain. These figures present the output of the analytical CCA and the computational models. First, we can see that the computational results generally closely match the results obtained from the CCA analytical model, especially at low fiber volume fractions, for both composites. Moreover, we observe that, for carbon fiber composites, the highly conductive fibers prevent most of the electrical currents from propagating through the piezoresistive matrix, since carbon fibers have significantly higher conductivity compared to the CNF/epoxy. This makes the composite mostly non-piezoresistive along the axial direction. However, piezoresistive behavior is still detectable in the lateral direction for carbon fiber composites because the electrical current here must pass through the piezoresistive matrix first. However, we can clearly observe strain-induced resistivity changes along the longitudinal direction in glass fiber composites, as the glass fiber here has a remarkably higher resistivity value, compared to the piezoresistive matrix, which forces currents to go through the matrix rather than through the insulating glass fiber. As a consequence, piezoresistive characteristics along the glass fiber direction are observed. All of these findings again confirm our observations previously discussed in Chapters 3 and 4.

Closely comparing the predictions of the analytical and computational models can yield additional fruitful findings. First, it can be observed that as the fiber volume fraction increases, for both axial and radial deformations, the discrepancy between the analytical and

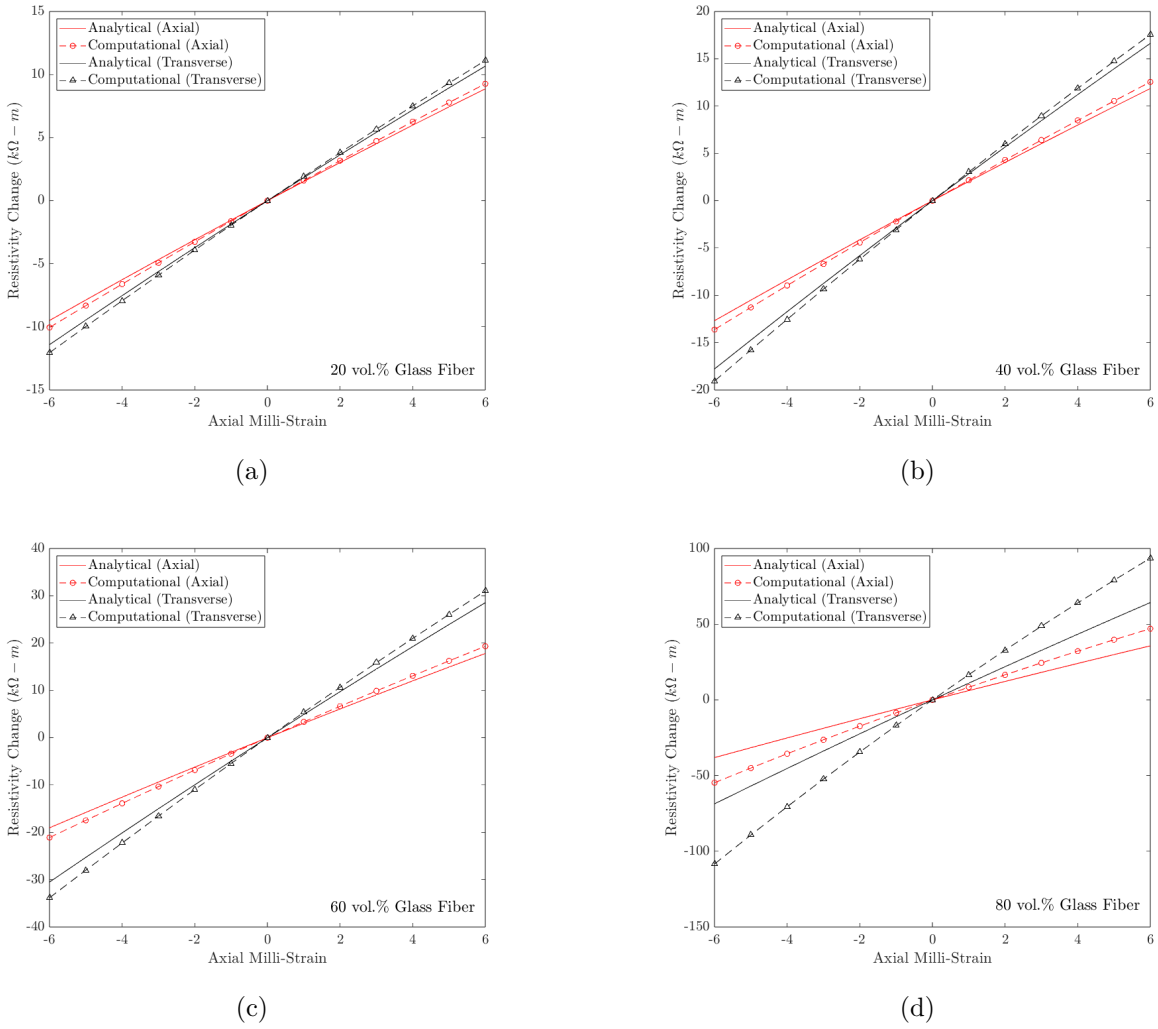

Figure 5.7. Comparing analytical model and computational model predictions for changes in the axial and transverse resistivities as functions of axial strain of CNF-modified epoxy composite with glass fiber reinforcement at (a) 20, (b) 40, (c) 60 and (d) 80 vol.% glass fiber

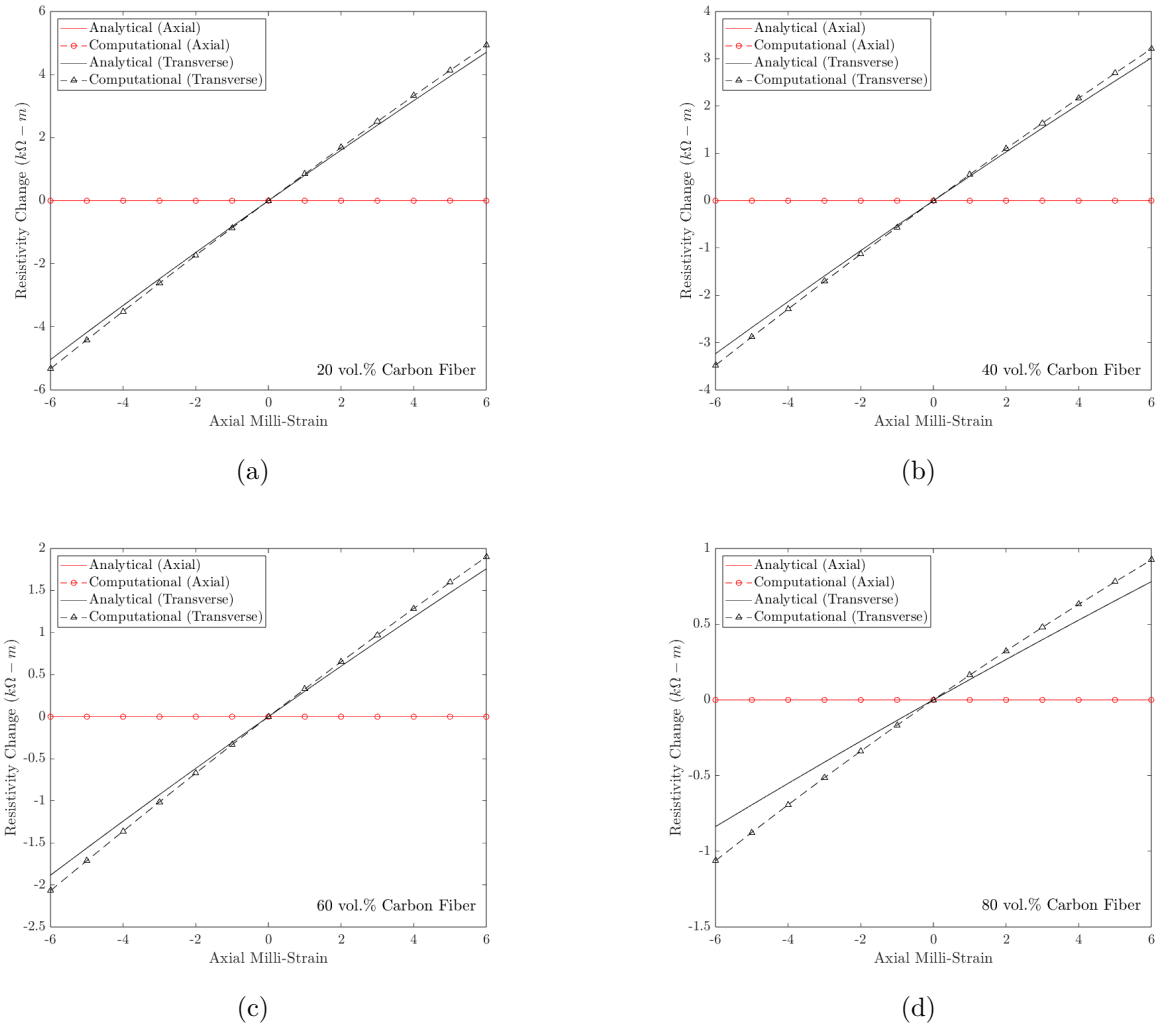

Figure 5.8. Comparing analytical model and computational model predictions for changes in the axial and transverse resistivities as functions of axial strain of CNF-modified epoxy composite with carbon fiber reinforcement at (a) 20, (b) 40, (c) 60 and (d) 80 vol.% carbon fiber

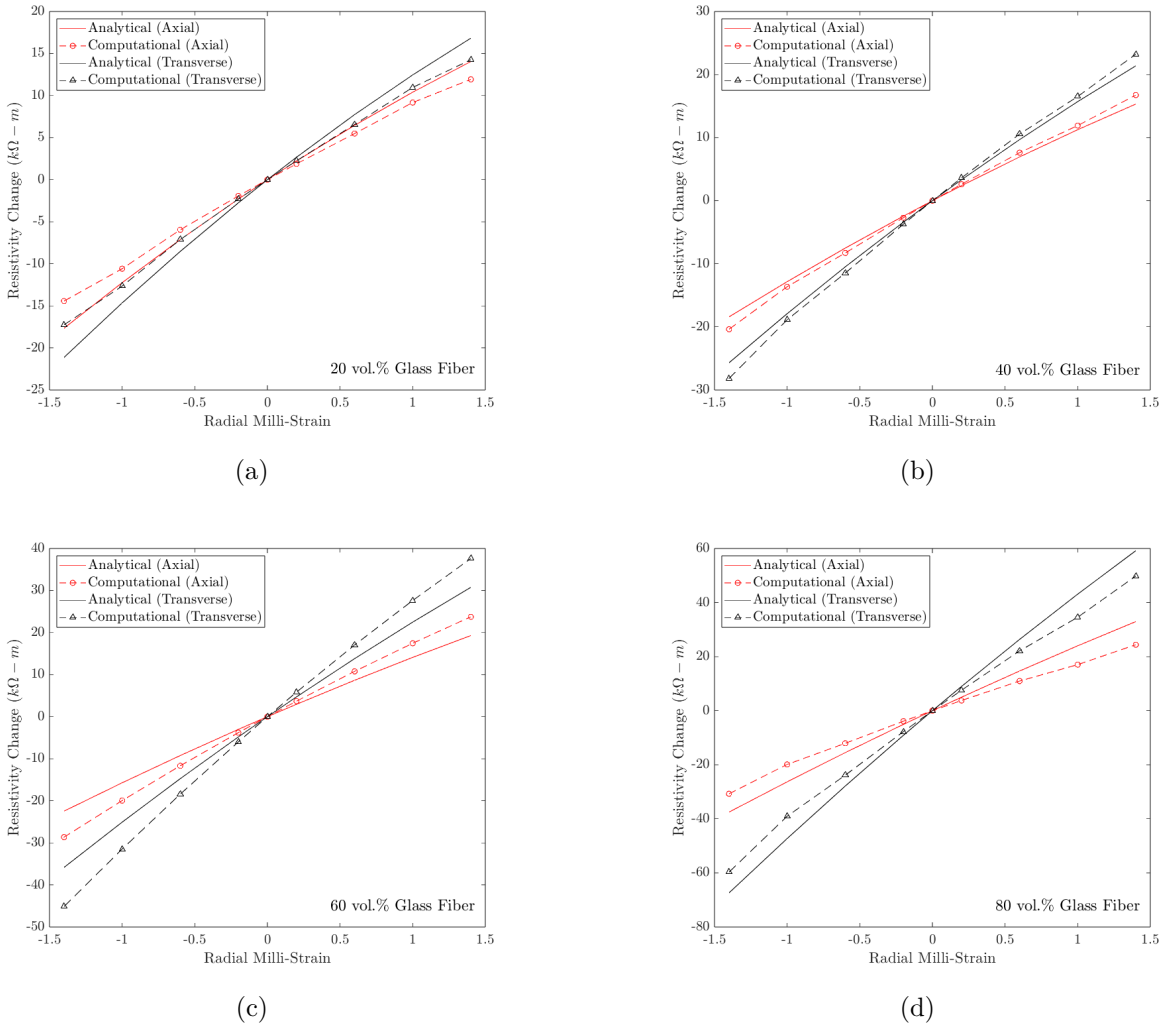

Figure 5.9. Comparing analytical model and computational model predictions for changes in the axial and transverse resistivities as functions of lateral (radial) strain of CNF-modified epoxy composite with glass fiber reinforcement at (a) 20, (b) 40, (c) 60 and (d) 80 vol.% glass fiber

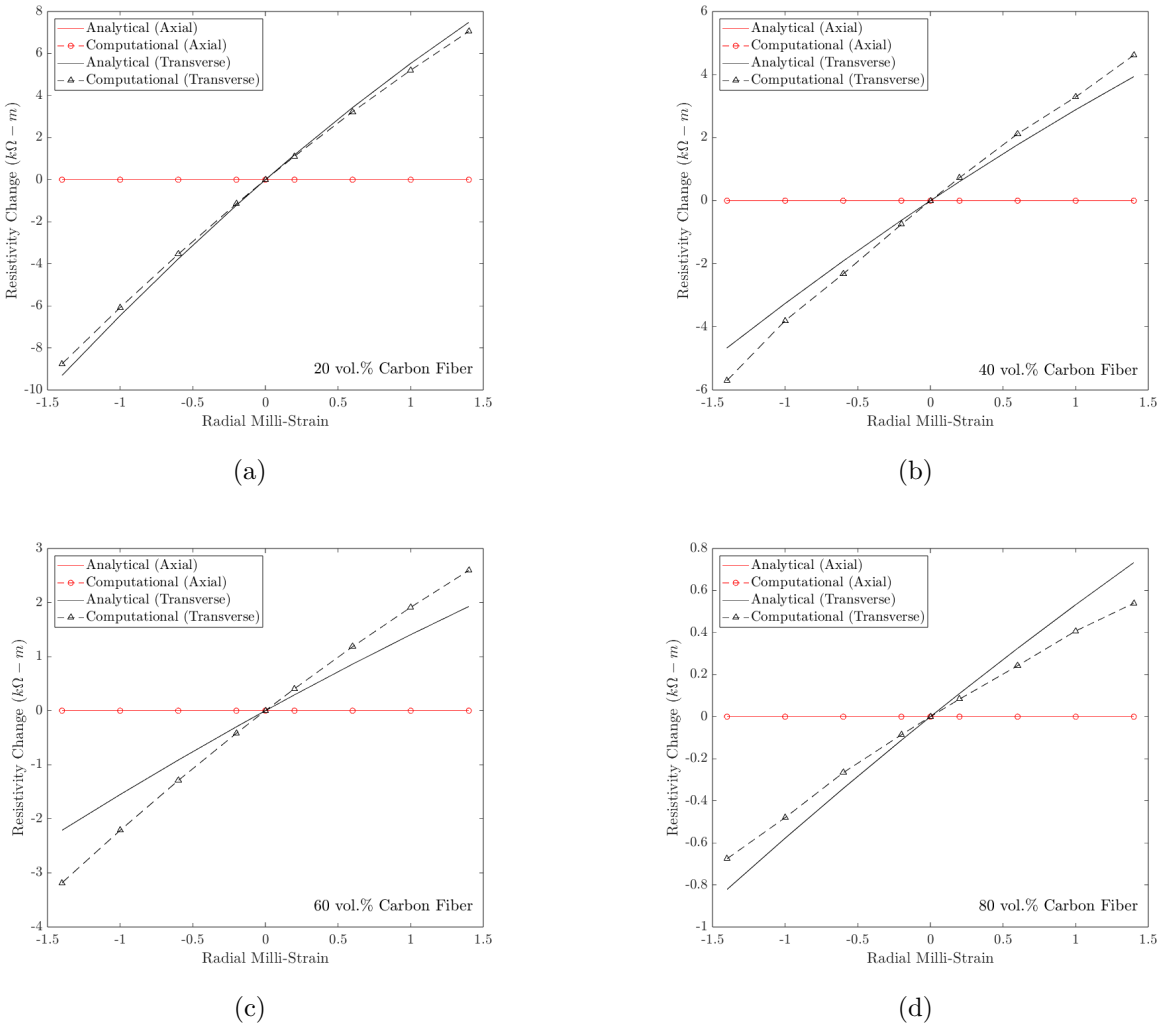

Figure 5.10. Comparing analytical model and computational model predictions for changes in the axial and transverse resistivities as functions of lateral (radial) strain of CNF-modified epoxy composite with carbon fiber reinforcement at (a) 20, (b) 40, (c) 60 and (d) 80 vol.% carbon fiber

computational models becomes more evident. To find an explanation behind these differences, one needs to examine the basic pillar assumptions on which each model was based. Unlike the computational model, which was developed on the basis of an RVE that contains a group of packed adjacent continuous reinforcing fibers enclosed by CNF/epoxy, the analytical CCA model was created by considering a single cylindrical fiber surrounded by the matrix, creating a two-concentric cylinders system. The assumption of a dilute suspension condition is, in fact, inherent in the CCA model. This assumption is an idealization adopted in the well-known mechanical CCA model [130], which states that fibers within a composite are separated and far away from each other such that all interactions between them can be safely ignored. As a result, these interactions do not affect the overall macroscale behavior of the composite. In other words, the single-fiber CCA model is a good enough representative of the macroscale characteristics of the composite. This assumption may fundamentally limit the ability of the CCA model to capture the complex behavior of real composite materials, where fiber interactions can significantly affect overall properties. On the contrary, the RVE model, which incorporates multiple adjacent fibers, allows for the consideration of these interactions, including mechanical constraints and localized stress concentrations that arise from the physical proximity of the fibers. Thus, as the volume fraction of fibers increases, the assumption of negligible fiber interactions becomes less accurate. To elaborate more, interactions between adjacent fibers, particularly in composites with high fiber volume fractions, can lead to a totally different strain distribution within the matrix, compared to the single-fiber assumption, as non-linear effects are not captured by the dilute suspension assumption. Thus, the difference between the strain distributions captured by both models, especially at high fiber fractions, is the main reason behind the observed discrepancy. This is because the piezoresistivity behavior of the matrix is directly related to the strain distribution according to the Koo and Tallman relation [113], which was presented in equation (5.25).

Based on the preceding discussion, we can derive multiple conclusions. The piezoresistive characteristics of the composite are influenced by the complex stress and strain fields that arise from the presence of multiple adjacent fibers, particularly at higher volume fractions. Nevertheless, when considering low-to-moderate fiber volume fractions, the predictions of

the CCA model exhibit significantly reduced deviations. In addition, the solutions of the CCA model and the computational model typically converge at small deformations. Hence, the CCA model, with its ability to provide closed-form relations, can be effectively used to accurately model the piezoresistivity of composites with low or moderate fiber volume fractions (60% vol. or less) at small deformations. That is to say, while there may be variations at larger fiber volume fractions, the CCA remains valuable, as these variations are not significant. Moreover, because of its analytical nature, it is highly practical.

6. SUMMARY AND CONCLUSIONS

Parts of this chapter were previously published in *Composites Science and Technology* [1].

6.1 Summary

This dissertation was driven by the lack of research on analytical macroscale models of piezoresistivity in fiber-reinforced nanofiller-modified composites. These models are crucial for making meaningful structural and/or mechanical predictions based on electrical measurements. To address this deficiency, the subsequent three research contributions were accomplished.

- Research Contribution 1: Analytical Modeling of *Axial* Strain Piezoresistivity
  The first contribution used the CCA analytical modeling approach to explore piezoresistivity as a result of axial strain in fiber-reinforced nanofiller-modified composites. This approach considers a single continuous fiber surrounded by a nanofiller-modified matrix, representing the composite at the macroscale level. By homogenizing the composite, which is modeled as two concentric cylinders, the inner cylinder representing the fiber and the outer cylinder representing the nanofiller-modified epoxy, we aimed to create a hypothetical homogenized material. The piezoresistive characteristics of this homogenized system were intended to mirror those of the inhomogeneous CNF-modified epoxy and continuous fiber composite. Utilizing the conservation of electrical energy and the elasticity solution of the CCA model, alongside the piezoresistive tensor relation developed by Koo and Tallman, we derived closed-form analytical relations. These relations were for the longitudinal and transverse resistivity changes resulting from axial deformations of CNF/epoxy with a continuous fiber phase, allowing us to predict strain-induced resistivity variations. Carbon fiber and glass fiber-reinforced nanocomposites were used to demonstrate the capabilities of the developed model in predicting piezoresistivity. Furthermore, the results obtained were compared with the exact solutions calculated by directly considering the heterogeneous system (no homogenization) and the rule of mixtures. It was observed that the homogenized CCA-based

model and the inhomogeneous exact solutions are in excellent agreement. However, a significant discrepancy was perceived between the predictions obtained via the CCA model and the rule of mixtures.

- Research Contribution 2: Analytical Modeling of *Radial* Strain Piezoresistivity
  The second contribution focused primarily on the piezoresistivity due to radial strain, again utilizing the CCA analytical modeling technique. Within this framework, the same homogenization process was applied to understand the axial and lateral resistivity changes caused by radial deformations. It was found that the strain tensor within the deformed matrix varies radially, in contrast to axial strain piezoresisitivity, where the resistivity values of the constituents remained constant regardless of the deformation state. According to the strain-resistivity relations of Koo and Tallman, the change in the resistivity of the deformed matrix was also a function of r. Consequently, a challenge emerged in the formulation of the lateral piezoresistivity relationship due to the inability to analytically solve the electrical diffusion PDE. Nevertheless, that problem was resolved by taking into account the volumetric average of the deformed matrix strain tensor, which resulted in a resistivity change within the matrix that was "quasi-constant." This allowed us to progress with the development of the strain-resistivity relations. These analytical relations were designed with a specific goal of describing the axial and transverse resistivity changes that occur when radial strains are applied to the CNF/epoxy composite. We successfully validated our approach by comparing the predictions of the radial strain piezoresistive model inhomogeneous solutions. Again, it was also observed that the inhomogeneous predictions aligned well with the CCA model, whereas the rule of mixtures provided poor predictions.

- Research Contribution 3: Lamina-Level Validation via Computational Analyses
  In the third contribution, we sought to model piezoresistivity in fiber-reinforced laminae with a CNF-modified epoxy matrix phase using a computational approach. This approach involved the construction of several three-dimensional RVEs that represent different fiber volume fractions. These RVEs are built based a group of unidirectional adjacent fibers embedded within the epoxy. The main objective of this contribution

was to study the influence of considering multiple adjacent fibers, rather than a single fiber, as in the CCA approach, on the macroscale piezoresistivity. This was accomplished by comparing the obtained analytical results with the computational model predictions. This comparison was intended to validate the use of the analytical model for predicting piezoresistivity in fiber-reinforced laminae. This modeling approach relied on FEA, where ABAQUS, Python, and MATLAB were used simultaneously to find solutions for electromechanical BVPs. Furthermore, to ensure that the obtained FE solutions were comparable to the macroscale responses, periodic boundary conditions were imposed. In the end, this comparative study enabled us to evaluate the accuracy and efficacy of the analytical model, while also acquiring a comprehensive understanding of how fiber volume fractions can impact the piezoresistivity behavior of the composite. Changing the fiber volume fraction may magnify the effect of fiber interactions on the matrix strain field, thereby altering the composite's piezoresistive response.

6.2 Conclusions

We can draw several conclusions from the first two contributions. First, the homogenized CCA-based model and the inhomogeneous exact solutions are in excellent agreement. This agreement validates the accuracy of the results obtained by the analytical model. Second, although CCA homogenization in the axial direction produced results consistent with the rule of mixtures for the constituent conductivities found in [100], the rule of mixtures cannot be used to predict changes in resistivity induced by axial and radial strain. Third, the electrical properties of the constituents strongly influence the piezoresistive response of the composite. For highly conductive fibers, such as carbon fibers, there is essentially no change in axial resistivity. This outcome was anticipated due to the relatively high conductivity of the fiber compared to the CNF-modified matrix, which, even in very small amounts, essentially provides a short circuit for electrical current. On the other hand, for highly resistive fibers, such as glass fibers, the model demonstrated that the transverse and axial piezoresistivity converge at lower fiber volume fractions because of the dominance of the conductive matrix.

We can also draw several conclusions from the third contribution. First, it was found that the general axial and lateral piezoresistivity behaviors of the composite captured via the multiple-fiber approach are approximately equivalent to those predicted analytically. This serves as an additional layer of confirmation in addition to the inhomogeneous exact solution. However, slight discrepancies were observed between the single-fiber and multiple-fiber approaches, particularly at higher fiber volume fractions. This can be explained as follows: As the fiber volume fraction becomes higher, the interaction between densely packed fibers in a composite can strongly affect the strain fields within the matrix and alter them compared to those predicted by models assuming isolated fibers (the CCA model). These strain field alternations directly influence the matrix resistivity changes according to the Koo and Tallman piezoresistive relations. Nevertheless, for composites with low to moderate fiber volume fractions and subjected to small strains, the observed differences are not that significant.

In conclusion, the analytical model presented in this dissertation can serve as an effective piezoresistive modeling tool for continuous fiber-reinforced composites with piezoresistive matrices, precisely predicting changes in lamina resistivity, particularly under small deformations. The accuracy of the analytical model improves even further for composites with low fiber volume fractions, in which fibers are sparsely distributed and the piezoresistivity behavior of the single-fiber + matrix configuration closely resembles that of a lamina. One of the main advantages of employing the analytical model lies in its ability to avoid the complex characteristics and the significant computational costs associated with the computational models, all while still maintaining a high level of accuracy.

7. RECOMMENDATIONS FOR FUTURE WORK

In light of the contributions proposed in this dissertation, which represent significant fundamental advancements that lay the foundation for future contributions and research initiatives that aim to bridge the aforementioned knowledge gap, the following discussions propose several future research directions.

- Model Multi-axial and shear loads for the CCA model

  Multi-axial and shear loading conditions are more representative of real-world applications where composites are subjected to complex stress states. Extending the CCA model to account for multi-axial or shear loading could significantly enhance the model's predictive capability for the piezoresistive behavior under such conditions. Future studies could explore the integration of multi-axial stress states into the homogenization process of the CCA model, potentially employing tensorial representations of stress-strain and piezoresistivity to capture the anisotropic nature of these composites.

- Develop a computational-based linear piezoresistive relations at a unidirectional fiber-reinforced lamina level

  Developing linear piezoresistive relations, analogous to stress-strain linear constitutive relations, enable us to computationally characterize the piezoresistive behavior in fiber-reinforced piezoresistive laminae subjected to multi-axial and shear deformations. They can provide a deeper understanding of the complex interactions between adjacent fibers and the matrix, which in turn influences the overall electrical response of the composite. Additionally, comparing the computationally based piezoresistivity results, which will be based on a lamina level, with the analytical single-fiber ones for composites under shear or multi-axial strains (obtained from the previously proposed future research work) would provide further insight regarding the feasibility of implementing the CCA single-fiber based model for piezoresistivity predictions in laminae.

- Propose a more comprehensive non-linear computational-based piezoresistive relations for laminae

  Recognizing that the piezoresistivity in fiber-reinforced nanocomposite laminae may ex-

hibit nonlinear characteristics, especially at large deformations, opens up more insights for capturing the true nature of piezoresistivity more accurately. In other words, nonlinear piezoresistive relations can reflect the material's response more faithfully under a broader range of strains. Such improvements may offer the potential for significant advancements in the design and application of smart composite materials, especially when subjected to large deformations.

- Develop a laminate theory of piezoresistivity

  Our research has primarily concentrated on the development of models at the lamina level. However, it is worth noting that in practical applications, composite structures are frequently produced in the form of laminates. Thus, our proposed models can serve as fundamental stepping stones toward a laminate theory of piezoresistivity. This piezoresistive laminate theory would leverage the principles of classical laminate theory while integrating piezoresistive effects. It could offer new perspectives on how different layers interact electrically and mechanically, influencing the overall piezoresistive response. Hence, this research contribution has the potential to provide valuable insights for the development of optimized piezoresistive laminates that exhibit improved performance properties.

- Examine the influence of considering non-perfectly bounded interface layers

  It is worth highlighting the implicit role of the interface layer in our CCA model. Within the elastic CCA model framework, the fiber and matrix phases are regarded as perfectly bonded, incorporating the interface boundary conditions. At large applied strains, debonding may occur, which presents a more complex scenario, since significant alternations occur in the strain field within the composite constituents. However, the effect on the electrical response might be different between conductive and non-conductive reinforcing fibers. For instance, in glass fiber composites, it is expected that the strain-field alterations as a result of debonding might not have a major influence on the electrical current transfer, primarily because the glass fiber is not inherently conductive. Conversely, with the conductive carbon fibers, where debonding could substantially disturb the electrical current path, the influence on piezoresistivity would

likely be pronounced. This difference shows how important it is to study the influence of the interface in more depth, especially during large-strain circumstances that can lead to debonding, which is a promising area for future research.

- Model piezoresistivity in carbon fiber-reinforced laminates with non-conductive matrix phases

  The objective of this study is to examine the distinct impact of highly conductive carbon fibers on the piezoresistive properties of the composite material, while disregarding the influence of nanofillers. This contribution will concentrate on the inherent features of carbon fibers that might affect the piezoresistivity, as well as additional potential factors, such as carbon fiber arrangements, waviness, and the interfiber crossings. In order to accomplish this goal, it is necessary to develop laminae and laminate models of piezoresistivity for continuous carbon fiber composites that do not account for nanofillers. This methodology facilitates the advancement of more accurate piezoresistive predictions, resulting in significantly improved structural applications.

REFERENCES

[1] S. M. Ghazzawi and T. N. Tallman, "Deformation-dependent electrical resistivity of fiber-reinforced nanocomposites: A concentric cylindrical model approach," *Composites Science and Technology*, vol. 243, p. 110 251, 2023.

[2] S. Jeyanthi, J. J. Rani, *et al.*, "Improving mechanical properties by kenaf natural long fiber reinforced composite for automotive structures," *Journal of Applied Science and Engineering*, vol. 15, no. 3, pp. 275–280, 2012.

[3] M. Jawaid and M. Thariq, *Sustainable composites for aerospace applications*. Woodhead publishing, 2018.

[4] N. Uddin, *Developments in fiber-reinforced polymer (FRP) composites for civil engineering*. Elsevier, 2013.

[5] N. V. Nayak, "Composite materials in aerospace applications," *International Journal of Scientific and Research Publications*, vol. 4, no. 9, pp. 1–10, 2014.

[6] O. Adekomaya and T. Majozi, "Industrial and biomedical applications of fiber reinforced composites," in *Fiber Reinforced Composites*, Elsevier, 2021, pp. 753–783.

[7] F. Rubino, A. Nisticò, F. Tucci, and P. Carlone, "Marine application of fiber reinforced composites: A review," *Journal of Marine Science and Engineering*, vol. 8, no. 1, p. 26, 2020.

[8] D. K. Rajak, D. D. Pagar, P. L. Menezes, and E. Linul, "Fiber-reinforced polymer composites: Manufacturing, properties, and applications," *Polymers*, vol. 11, no. 10, p. 1667, 2019.

[9] T. Ozbakkaloglu, J.-F. Chen, S. T. Smith, J.-G. Dai, *et al.*, *Applications of fiber reinforced polymer composites*, 2016.

[10] J. Teng, T. Yu, and D. Fernando, "Strengthening of steel structures with fiber-reinforced polymer composites," *Journal of constructional steel research*, vol. 78, pp. 131–143, 2012.

[11] M. Naser, R. Hawileh, and J. Abdalla, "Fiber-reinforced polymer composites in strengthening reinforced concrete structures: A critical review," *Engineering Structures*, vol. 198, p. 109 542, 2019.

[12] H. GangaRao, "Infrastructure applications of fiber-reinforced polymer composites," in *Applied Plastics Engineering Handbook*, Elsevier, 2017, pp. 675–695.

[13] K. N. Keya, N. A. Kona, F. A. Koly, K. M. Maraz, M. N. Islam, and R. A. Khan, "Natural fiber reinforced polymer composites: History, types, advantages and applications," *Materials Engineering Research*, vol. 1, no. 2, pp. 69–85, 2019.

[14] T. N. Tallman and D. J. Smyl, "Structural health and condition monitoring via electrical impedance tomography in self-sensing materials: A review," *Smart Materials and Structures*, vol. 29, no. 12, p. 123 001, 2020.

[15] Y. Liu, Y. Zhong, and C. Wang, "Recent advances in self-actuation and self-sensing materials: State of the art and future perspectives," *Talanta*, vol. 212, p. 120 808, 2020.

[16] J. Duke Jr, E. Henncke II, W. Stinchcomb, and K. Reifsnider, "Nondestructive evaluation of composite materialsa design philosophy," in *Mechanical Behaviour of Materials*, Elsevier, 1984, pp. 489–495.

[17] T. S. Jones, "Nondestructive evaluation methods for composites," in *Handbook of Composites*, Springer, 1998, pp. 838–856.

[18] J. Chen, Z. Yu, and H. Jin, "Nondestructive testing and evaluation techniques of defects in fiber-reinforced polymer composites: A review," *Frontiers in Materials*, vol. 9, p. 986 645, 2022.

[19] M. Strg and W. Swiderski, "Defect detection in aramid fiber-reinforced composites via terahertz radiation," *Journal of Nondestructive Evaluation*, vol. 42, no. 1, p. 9, 2023.

[20] S. Gholizadeh, "A review of non-destructive testing methods of composite materials," *Procedia structural integrity*, vol. 1, pp. 50–57, 2016.

[21] N. Saha, P. Roy, and P. Topdar, "Damage detection in composites using non-destructive testing aided by ann technique: A review," *Journal of Thermoplastic Composite Materials*, p. 08 927 057 231 172 670, 2023.

[22] Y. D. Kotriwar, O. Elshafiey, L. Peng, *et al.*, "Gradient feature-based method for defect detection of carbon fiber reinforced polymer materials," in *2023 IEEE International Conference on Prognostics and Health Management (ICPHM)*, IEEE, 2023, pp. 246–252.

[23] A. Anbalagan, V. S. Ramalingam, E. F. Sundarsingh, and S. Subbaraj, "A novel microwave-based non-destructive testing system for detection of sub-surface defects in natural flax fiber reinforced composite material," *Proceedings of the Institution of Mechanical Engineers, Part L: Journal of Materials: Design and Applications*, p. 14 644 207 231 195 996, 2023.

[24] Z. Tian, Y. Li, J. Zheng, and S. Wang, "A state-of-the-art on self-sensing concrete: Materials, fabrication and properties," *Composites Part B: Engineering*, vol. 177, p. 107 437, 2019.

[25] K. Kanagasundaram and E. Solaiyan, "Smart cement-sensor composite: The evolution of nanomaterial in developing sensor for structural integrity," *Structural Concrete*, 2023.

[26] A. Dinesh, D. Suji, and M. Pichumani, "Real-time implication of hybrid carbonaceous fibre and powder integrated self-sensing cement composite in health monitoring of beams and columns," *European Journal of Environmental and Civil Engineering*, pp. 1–18, 2023.

[27] P. N. Reddy, B. V. Kavyateja, and B. B. Jindal, "Structural health monitoring methods, dispersion of fibers, micro and macro structural properties, sensing, and mechanical properties of self-sensing concretea review," *Structural Concrete*, vol. 22, no. 2, pp. 793–805, 2021.

[28] C. S. Smith, "Piezoresistance effect in germanium and silicon," *Physical review*, vol. 94, no. 1, p. 42, 1954.

[29] X. Xin, M. Liang, Z. Yao, *et al.*, "Self-sensing behavior and mechanical properties of carbon nanotubes/epoxy resin composite for asphalt pavement strain monitoring," *Construction and Building Materials*, vol. 257, p. 119 404, 2020.

[30] D. L. Castañeda-Saldarriaga, J. Alvarez-Montoya, V. Martínez-Tejada, and J. Sierra-Pérez, "Toward structural health monitoring of civil structures based on self-sensing concrete nanocomposites: A validation in a reinforced-concrete beam," *International Journal of Concrete Structures and Materials*, vol. 15, no. 1, pp. 1–18, 2021.

[31] K. Ikikardaslar and F. Delale, "Self-sensing damage in cnt infused epoxy panels with and without glass-fibre reinforcement," *Strain*, vol. 54, no. 4, e12268, 2018.

[32] M. S. Konsta-Gdoutos and C. A. Aza, "Self sensing carbon nanotube (cnt) and nanofiber (cnf) cementitious composites for real time damage assessment in smart structures," *Cement and Concrete Composites*, vol. 53, pp. 162–169, 2014.

[33] J. Tao, X. Wang, Z. Wang, and Q. Zeng, "Graphene nanoplatelets as an effective additive to tune the microstructures and piezoresistive properties of cement-based composites," *Construction and Building Materials*, 2019. DOI: 10.1016/J.CONBUILDMAT.2019.03.173.

[34] S. Ding, C. Xu, Y. Ni, and B. Han, "Extracting piezoresistive response of self-sensing cementitious composites under temperature effect via bayesian blind source separation," *Smart Materials and Structures*, vol. 30, 2021. DOI: 10.1088/1361-665X/abf992.

[35] L. Wang and F. Aslani, "Piezoresistivity performance of cementitious composites containing activated carbon powder, nano zinc oxide and carbon fibre," *Construction and Building Materials*, vol. 278, p. 122 375, 2021. DOI: 10.1016/J.CONBUILDMAT.2021.122375.

[36] R. Ak, A. Hunashyal, F. A. Gudagi, and M. F. Mulla, "Piezo-resistive properties of polymer based cement nano composites," *E3S Web of Conferences*, 2023. DOI: 10.1051/e3sconf/202345503013.

[37] G. Spinelli, P. Lamberti, V. Tucci, L. Vertuccio, and L. Guadagno, "Experimental and theoretical study on piezoresistive properties of a structural resin reinforced with carbon nanotubes for strain sensing and damage monitoring," *Composites Part B: Engineering*, 2018. DOI: 10.1016/J.COMPOSITESB.2018.03.025.

[38] D. Chung, "A critical review of piezoresistivity and its application in electrical-resistance-based strain sensing," *Journal of Materials Science*, vol. 55, no. 32, pp. 15 367–15 396, 2020.

[39] A. Lekawa-Raus, K. K. Koziol, and A. H. Windle, "Piezoresistive effect in carbon nanotube fibers," *ACS nano*, vol. 8, no. 11, pp. 11 214–11 224, 2014.

[40] F. Avilés, A. I. Oliva-Avilés, and M. Cen-Puc, "Piezoresistivity, strain, and damage self-sensing of polymer composites filled with carbon nanostructures," *Advanced Engineering Materials*, vol. 20, no. 7, p. 1 701 159, 2018.

[41] J. Park, T. Hwang, H. Kim, and Y. Doh, "Experimental and numerical study of the electrical anisotropy in unidirectional carbon-fiber-reinforced polymer composites," *Smart materials and structures*, vol. 16, no. 1, p. 57, 2006.

[42] S. Zhu and D. Chung, "Analytical model of piezoresistivity for strain sensing in carbon fiber polymer–matrix structural composite under flexure," *Carbon*, vol. 45, no. 8, pp. 1606–1613, 2007.

[43] H.-h. Wu, S.-c. Li, J.-n. Zhang, and L. Tong, "Electrical resistivity response of unidirectional thin-ply carbon fiber reinforced polymers," *Composite Structures*, vol. 228, p. 111 342, 2019.

[44] X. Gao, J. Yang, J. Wu, *et al.*, "Piezoelectric actuators and motors: Materials, designs, and applications," *Advanced Materials Technologies*, vol. 5, 2019. DOI: 10.1002/admt.201900716.

[45] H. Jin, X. Gao, K. Ren, *et al.*, "Review on piezoelectric actuators based on high-performance piezoelectric materials," *IEEE Transactions on Ultrasonics, Ferroelectrics, and Frequency Control*, vol. 69, pp. 3057–3069, 2022. DOI: 10.1109/TUFFC.2022.3175853.

[46] H. Kulkarni, K. Zohaib, A. Khusru, and K. S. Aiyappa, "Application of piezoelectric technology in automotive systems," *Materials Today: Proceedings*, vol. 5, pp. 21 299–21 304, 2018. DOI: 10.1016/J.MATPR.2018.06.532.

[47] K. K. Sappati and S. Bhadra, "Piezoelectric polymer and paper substrates: A review," *Sensors (Basel, Switzerland)*, vol. 18, 2018. DOI: 10.3390/s18113605.

[48] S. Mohith, A. R. Upadhya, K. Navin, S. Kulkarni, and M. Rao, "Recent trends in piezoelectric actuators for precision motion and their applications: A review," *Smart Materials and Structures*, vol. 30, 2020. DOI: 10.1088/1361-665X/abc6b9.

[49] M. Ju, Z. Dou, J.-W. Li, *et al.*, "Piezoelectric materials and sensors for structural health monitoring: Fundamental aspects, current status, and future perspectives," *Sensors (Basel, Switzerland)*, vol. 23, 2023. DOI: 10.3390/s23010543.

[50] X. Qing, W. Li, Y. Wang, and H. Sun, "Piezoelectric transducer-based structural health monitoring for aircraft applications," *Sensors (Basel, Switzerland)*, vol. 19, 2019. DOI: 10.3390/s19030545.

[51] P. Jiao, K. Egbe, Y. Xie, A. M. Nazar, and A. Alavi, "Piezoelectric sensing techniques in structural health monitoring: A state-of-the-art review," *Sensors (Basel, Switzerland)*, vol. 20, 2020. DOI: 10.3390/s20133730.

[52] W. S. Na and J. Baek, "A review of the piezoelectric electromechanical impedance based structural health monitoring technique for engineering structures," *Sensors (Basel, Switzerland)*, vol. 18, 2018. DOI: 10.3390/s18051307.

[53] X. Zhang, Y. Wang, X. Gao, *et al.*, "High-temperature and flexible piezoelectric sensors for lamb-wave-based structural health monitoring," *ACS applied materials & interfaces*, 2021. DOI: 10.1021/acsami.1c13704.

[54] H. Hassan and T. N. Tallman, "Failure prediction in self-sensing nanocomposites via genetic algorithm-enabled piezoresistive inversion," *Structural Health Monitoring*, vol. 19, no. 3, pp. 765–780, 2020.

[55] H. Hassan and T. N. Tallman, "A comparison of metaheuristic algorithms for solving the piezoresistive inverse problem in self-sensing materials," *IEEE Sensors Journal*, vol. 21, no. 1, pp. 659–666, 2020.

[56] L. Chen, H. Hassan, T. N. Tallman, S.-S. Huang, and D. Smyl, "Predicting strain and stress fields in self-sensing nanocomposites using deep learned electrical tomography," *Smart Materials and Structures*, vol. 31, no. 4, p. 045 024, 2022.

[57] H. Dai, G. J. Gallo, T. Schumacher, and E. T. Thostenson, "A novel methodology for spatial damage detection and imaging using a distributed carbon nanotube-based composite sensor combined with electrical impedance tomography," *Journal of Nondestructive Evaluation*, vol. 35, pp. 1–15, 2016.

[58] H. Hassan, F. Semperlotti, K.-W. Wang, and T. N. Tallman, "Enhanced imaging of piezoresistive nanocomposites through the incorporation of nonlocal conductivity changes in electrical impedance tomography," *Journal of Intelligent Material Systems and Structures*, vol. 29, no. 9, pp. 1850–1861, 2018.

[59] H. Hassan and T. Tallman, "Predicting failure from conductivity changes in piezoresistive nanocomposites," in *Sensors and Smart Structures Technologies for Civil, Mechanical, and Aerospace Systems 2018*, SPIE, vol. 10598, 2018, pp. 15–25.

[60] H. Hassan and T. Tallman, "Experimental identification of stress concentrations in piezoresistive nanocomposites via electrical impedance tomography," in *Sensors and Smart Structures Technologies for Civil, Mechanical, and Aerospace Systems 2019*, SPIE, vol. 10970, 2019, pp. 380–388.

[61] T. Tallman and K. Wang, "An inverse methodology for calculating strains from conductivity changes in piezoresistive nanocomposites," *Smart Materials and Structures*, vol. 25, no. 11, p. 115 046, 2016.

[62] T. Tallman, S. Gungor, G. Koo, and C. Bakis, "On the inverse determination of displacements, strains, and stresses in a carbon nanofiber/polyurethane nanocomposite from conductivity data obtained via electrical impedance tomography," *Journal of Intelligent Material Systems and Structures*, vol. 28, no. 18, pp. 2617–2629, 2017.

[63] T. N. Tallman, S. Gungor, K. Wang, and C. E. Bakis, "Damage detection via electrical impedance tomography in glass fiber/epoxy laminates with carbon black filler," *Structural Health Monitoring*, vol. 14, no. 1, pp. 100–109, 2015.

[64] C. Li and T.-W. Chou, "Modeling of damage sensing in fiber composites using carbon nanotube networks," *Composites Science and Technology*, vol. 68, no. 15-16, pp. 3373–3379, 2008.

[65] R. Haj-Ali, H. Zemer, R. El-Hajjar, and J. Aboudi, "Piezoresistive fiber-reinforced composites: A coupled nonlinear micromechanical–microelectrical modeling approach," *International Journal of Solids and Structures*, vol. 51, no. 2, pp. 491–503, 2014.

[66] Z. Xia, T. Okabe, J. Park, W. Curtin, and N. Takeda, "Quantitative damage detection in cfrp composites: Coupled mechanical and electrical models," *Composites science and technology*, vol. 63, no. 10, pp. 1411–1422, 2003.

[67] S. Gong and Z. H. Zhu, "On the mechanism of piezoresistivity of carbon nanotube polymer composites," *Polymer*, vol. 55, no. 16, pp. 4136–4149, 2014.

[68] S. Gong, Z. Zhu, and E. Haddad, "Modeling electrical conductivity of nanocomposites by considering carbon nanotube deformation at nanotube junctions," *Journal of Applied Physics*, vol. 114, no. 7, p. 074 303, 2013.

[69] M. Taya, W. Kim, and K. Ono, "Piezoresistivity of a short fiber/elastomer matrix composite," *Mechanics of materials*, vol. 28, no. 1-4, pp. 53–59, 1998.

[70] A. B. Oskouyi, U. Sundararaj, and P. Mertiny, "Tunneling conductivity and piezoresistivity of composites containing randomly dispersed conductive nano-platelets," *Materials*, vol. 7, no. 4, pp. 2501–2521, 2014.

[71] W. Shim, S.-Y. Jeon, and W.-R. Yu, "Modeling of the piezoresistive behavior of carbon nanotube/polymer composites during stress relaxation," *Polymer Composites*, vol. 43, no. 5, pp. 2672–2682, 2022.

[72] S. Gong, Z. Zhu, and S. Meguid, "Carbon nanotube agglomeration effect on piezoresistivity of polymer nanocomposites," *Polymer*, vol. 55, no. 21, pp. 5488–5499, 2014.

[73] N. Hu, Z. Masuda, G. Yamamoto, H. Fukunaga, T. Hashida, and J. Qiu, "Effect of fabrication process on electrical properties of polymer/multi-wall carbon nanotube nanocomposites," *Composites Part A: Applied Science and Manufacturing*, vol. 39, no. 5, pp. 893–903, 2008.

[74] N. Hu, Y. Karube, C. Yan, Z. Masuda, and H. Fukunaga, "Tunneling effect in a polymer/carbon nanotube nanocomposite strain sensor," *Acta materialia*, vol. 56, no. 13, pp. 2929–2936, 2008.

[75] R. Rahman and P. Servati, "Effects of inter-tube distance and alignment on tunnelling resistance and strain sensitivity of nanotube/polymer composite films," *Nanotechnology*, vol. 23, no. 5, p. 055 703, 2012.

[76] S. Gong, Z. Zhu, and S. Meguid, "Anisotropic electrical conductivity of polymer composites with aligned carbon nanotubes," *Polymer*, vol. 56, pp. 498–506, 2015.

[77] N. Hu, Y. Karube, M. Arai, *et al.*, "Investigation on sensitivity of a polymer/carbon nanotube composite strain sensor," *Carbon*, vol. 48, no. 3, pp. 680–687, 2010.

[78] F. Dalmas, R. Dendievel, L. Chazeau, J.-Y. Cavaillé, and C. Gauthier, "Carbon nanotube-filled polymer composites. numerical simulation of electrical conductivity in three-dimensional entangled fibrous networks," *Acta materialia*, vol. 54, no. 11, pp. 2923–2931, 2006.

[79] T. Tallman and K. Wang, "The influence of nanofiller alignment on transverse percolation and conductivity," *Nanotechnology*, vol. 26, no. 2, p. 025 501, 2014.

[80] H. Xiao, M. Liu, and J. Jiang, "Effect of aligning conductive particles on the piezoresistivity of composites," *Sensor Review*, vol. 35, no. 1, pp. 43–50, 2015.

[81] A. K. Chaurasia, X. Ren, and G. D. Seidel, "Computational micromechanics analysis of electron hopping and interfacial damage induced piezoresistive response in carbon nanotube-polymer nanocomposites," *Smart materials and structures*, vol. 23, no. 7, p. 075 023, 2014.

[82] N. Prakash and G. D. Seidel, "Electromechanical peridynamics modeling of piezoresistive response of carbon nanotube nanocomposites," *Computational Materials Science*, vol. 113, pp. 154–170, 2016.

[83] X. Ren and G. D. Seidel, "Computational micromechanics modeling of inherent piezoresistivity in carbon nanotube–polymer nanocomposites," *Journal of Intelligent Material Systems and Structures*, vol. 24, no. 12, pp. 1459–1483, 2013.

[84] W. Klimm and K. Kwok, "Computational analysis of tunneling conduction in piezoresistive carbon nanotube polymer composites," *Journal of Intelligent Material Systems and Structures*, p. 1045389X221128575, 2022.

[85] O. V. Lebedev, A. N. Ozerin, and S. G. Abaimov, "Multiscale numerical modeling for prediction of piezoresistive effect for polymer composites with a highly segregated structure," *Nanomaterials*, vol. 11, no. 1, p. 162, 2021.

[86] P. Wu and Z. Chen, "Peridynamic electromechanical modeling of damaging and cracking in conductive composites: A stochastically homogenized approach," *Composite Structures*, vol. 305, p. 116 528, 2023.

[87] S. S. Prabhu, R. Bhavani, G. K. Thonnuthodi, and R. Thiruvengadathan, "A computational approach to determine shielding effectiveness of carbon nanotube-based nanocomposites for emc application," *Computational Materials Science*, vol. 126, pp. 400–406, 2017.

[88] A. Oliva-Avilés, F. Avilés, G. t. Seidel, and V. Sosa, "On the contribution of carbon nanotube deformation to piezoresistivity of carbon nanotube/polymer composites," *Composites Part B: Engineering*, vol. 47, pp. 200–206, 2013.

[89] X. Ren, A. K. Chaurasia, A. I. Oliva-Avilés, J. J. Ku-Herrera, G. D. Seidel, and F. Avilés, "Modeling of mesoscale dispersion effect on the piezoresistivity of carbon nanotube-polymer nanocomposites via 3d computational multiscale micromechanics methods," *Smart Materials and Structures*, vol. 24, no. 6, p. 065 031, 2015.

[90] C. Cattin and P. Hubert, "Piezoresistance in polymer nanocomposites with high aspect ratio particles," *ACS applied materials & interfaces*, vol. 6, no. 3, pp. 1804–1811, 2014.

[91] F. Deng and Q.-S. Zheng, "An analytical model of effective electrical conductivity of carbon nanotube composites," *Applied Physics Letters*, vol. 92, no. 7, p. 071 902, 2008.

[92] F. C. Buroni and E. García-Macías, "Closed-form solutions for the piezoresistivity properties of short-fiber reinforced composites with percolation-type behavior," *Carbon*, vol. 184, pp. 923–940, 2021.

[93] M. A. Matos, S. T. Pinho, and V. L. Tagarielli, "Application of machine learning to predict the multiaxial strain-sensing response of cnt-polymer composites," *Carbon*, vol. 146, pp. 265–275, 2019.

[94] E. García-Macías, R. Castro-Triguero, A. Sáez, and F. Ubertini, "3d mixed micromechanics-fem modeling of piezoresistive carbon nanotube smart concrete," *Computer Methods in Applied Mechanics and Engineering*, vol. 340, pp. 396–423, 2018.

[95] Y. Fang, L.-Y. Li, and S.-H. Jang, "Piezoresistive modelling of cnts reinforced composites under mechanical loadings," *Composites Science and Technology*, vol. 208, p. 108 757, 2021.

[96] E. García-Macías, A. D'Alessandro, R. Castro-Triguero, D. Perez-Mira, and F. Ubertini, "Micromechanics modeling of the uniaxial strain-sensing property of carbon nanotube cement-matrix composites for shm applications," *Composite Structures*, vol. 163, pp. 195–215, 2017.

[97] T. Tallman and K. Wang, "An arbitrary strains carbon nanotube composite piezoresistivity model for finite element integration," *Applied Physics Letters*, vol. 102, no. 1, p. 011 909, 2013.

[98] T. Takeda, Y. Shindo, Y. Kuronuma, and F. Narita, "Modeling and characterization of the electrical conductivity of carbon nanotube-based polymer composites," *Polymer*, vol. 52, no. 17, pp. 3852–3856, 2011.

[99] F. Panozzo, M. Zappalorto, and M. Quaresimin, "Analytical model for the prediction of the piezoresistive behavior of cnt modified polymers," *Composites Part B: Engineering*, vol. 109, pp. 53–63, 2017.

[100] M. F. Haider, M. M. Haider, and F. Yasmeen, "Micromechanics model for predicting anisotropic electrical conductivity of carbon fiber composite materials," in *AIP Conference Proceedings*, AIP Publishing LLC, 2016, p. 030 011.

[101] S. Kundalwal and M. Ray, "Estimation of thermal conductivities of a novel fuzzy fiber reinforced composite," *International Journal of Thermal Sciences*, vol. 76, pp. 90–100, 2014.

[102] W. Chen and D. Zhang, "A micromechanics-based processing model for predicting residual stress in fiber-reinforced polymer matrix composites," *Composite Structures*, vol. 204, pp. 153–166, 2018.

[103] H. Xie, T. Ouyang, É. Germaneau, G. Qin, M. Hu, and H. Bao, "Unexpectedly large tunability of lattice thermal conductivity of monolayer silicene via mechanical strain," *arXiv preprint arXiv:1512.01685*, 2015.

[104] H. Xie, T. Ouyang, É. Germaneau, G. Qin, M. Hu, and H. Bao, "Large tunability of lattice thermal conductivity of monolayer silicene via mechanical strain," *Physical Review B*, vol. 93, no. 7, p. 075 404, 2016.

[105] X. Li, J. Liu, and R. Yang, "Tuning thermal conductivity with mechanical strain," in *International Heat Transfer Conference*, vol. 49415, 2010, pp. 551–558.

[106] X. Li, K. Maute, M. L. Dunn, and R. Yang, "Strain effects on the thermal conductivity of nanostructures," *Physical Review B*, vol. 81, no. 24, p. 245 318, 2010.

[107] A. Markworth, "The transverse thermal conductivity of a unidirectional fibre composite with fibre-matrix debonding: A calculation based on effective-medium theory," *Journal of materials science letters*, vol. 12, no. 19, pp. 1487–1489, 1993.

[108] R. J. DMello and A. M. Waas, "Virtual curing of textile polymer matrix composites," *Composite Structures*, vol. 178, pp. 455–466, 2017.

[109] B. W. Rosen and Z. Hashin, "Effective thermal expansion coefficients and specific heats of composite materials," *International Journal of Engineering Science*, vol. 8, no. 2, pp. 157–173, 1970.

[110] M. Kulkarni and R. Brady, "A model of global thermal conductivity in laminated carbon/carbon composites," *Composites science and Technology*, vol. 57, no. 3, pp. 277–285, 1997.

[111] W. CHEN and D. ZHANG, "A micromechanics based processing model for the curing response of a unidirectional fiber reinforced composite," in *Proceedings of the American Society for Composites: Thirty-First Technical Conference*, 2016.

[112] S. R. Hostler, M. Peswani, H. Yang, H. Paul, S. J. Rowan, and A. R. Abramson, "Stretching-induced thermal conductivity change in shape-memory polymer composites," *Journal of Heat Transfer*, vol. 142, no. 8, p. 081 401, 2020.

[113] G. Koo and T. Tallman, "Higher-order resistivity-strain relations for self-sensing nanocomposites subject to general deformations," *Composites Part B: Engineering*, vol. 190, p. 107 907, 2020.

[114] Z. Hashin, "Theory of fiber reinforced materials," NASA, Tech. Rep., 1972.

[115] X. F. Sánchez-Romate, J. Artigas, A. Jiménez-Suárez, M. Sánchez, A. Güemes, and A. Ureña, "Critical parameters of carbon nanotube reinforced composites for structural health monitoring applications: Empirical results versus theoretical predictions," *Composites Science and Technology*, vol. 171, pp. 44–53, 2019.

[116] M. Siegl and I. Ehrlich, "Transformation of the mechanical properties of fiber-reinforced plastic tubes from the cartesian coordinate system into the cylindrical coordinate system for the application of bending models," *Athens Journal of Technology & Engineering*, vol. 4, no. 1, pp. 47–62, 2017.

[117] A. Ticoalu, T. Aravinthan, and F. Cardona, "A review on the characteristics of gomuti fibre and its composites with thermoset resins," *Journal of Reinforced Plastics and Composites*, vol. 32, no. 2, pp. 124–136, 2013.

[118] *The online materials information resource*, 2022. [Online]. Available: https://www.matweb.com/search/DataSheet.aspx?MatGUID=d9c18047c49147a2a7c0b0bb1743e812&ckck=1.

[119] S. Bal, "Experimental study of mechanical and electrical properties of carbon nanofiber/epoxy composites," *Materials & Design (1980-2015)*, vol. 31, no. 5, pp. 2406–2413, 2010.

[120] I. Krucinska and T. Stypka, "Direct measurement of the axial poisson's ratio of single carbon fibres," *Composites Science and Technology*, vol. 41, no. 1, pp. 1–12, 1991.

[121] D. Varley, S. Yousaf, M. Youseffi, M. Mozafari, Z. Khurshid, and F. Sefat, "Fiber-reinforced composites," in *Advanced Dental Biomaterials*, Elsevier, 2019, pp. 301–315.

[122] N. Angelidis, C. Wei, and P. Irving, "The electrical resistance response of continuous carbon fibre composite laminates to mechanical strain," *Composites Part A: applied science and manufacturing*, vol. 35, no. 10, pp. 1135–1147, 2004.

[123] G. M. Koo, "On the development of macroscale modeling strategies for ac/dc transport-deformation coupling in self-sensing piezoresistive materials," Ph.D. dissertation, Purdue University, School of Aeronautics and Astronautics, 2020.

[124] W. Shu and I. Stanciulescu, "Multiscale homogenization method for the prediction of elastic properties of fiber-reinforced composites," *International Journal of Solids and Structures*, vol. 203, pp. 249–263, 2020.

[125] S. Stankevich, O. Bulderberga, S. Tarasovs, D. Zeleniakiene, M. Omastova, and A. Aniskevich, "Electrical conductivity of glass fiber-reinforced plastic with nanomodified matrix for damage diagnostic," *Materials*, vol. 14, no. 16, p. 4485, 2021.

[126] X. Ren and G. D. Seidel, "Computational micromechanics modeling of piezoresistivity in carbon nanotube–polymer nanocomposites," *Composite Interfaces*, vol. 20, no. 9, pp. 693–720, 2013.

[127] L. Mizzi, D. Attard, R. Gatt, K. K. Dudek, B. Ellul, and J. N. Grima, "Implementation of periodic boundary conditions for loading of mechanical metamaterials and other complex geometric microstructures using finite element analysis," *Engineering with Computers*, vol. 37, pp. 1765–1779, 2021.

[128] F. Taheri-Behrooz and E. Pourahmadi, "A 3d rve model with periodic boundary conditions to estimate mechanical properties of composites," *Structural Engineering and Mechanics*, vol. 72, no. 6, pp. 713–22, 2019.

[129] X. van Heule, *smrg-uob/PeriodicBoundaryCondition: PeriodicBoundaryCondition v2.1*, version v2.1, Python code, 2020. DOI: 10.5281/zenodo.4133511. [Online]. Available: https://doi.org/10.5281/zenodo.4133511.

[130] R. M. Christensen, *Mechanics of composite materials*. Courier Corporation, 2012.

VITA

Education

- Master of Science in Aerospace Engineering, King Fahd University of Petroleum and Minerals, Dhahran, Saudi Arabia, 2018.
- Bachelor of Science in Applied Aerospace Engineering, King Fahd University of Petroleum and Minerals, Dhahran, Saudi Arabia, 2016.

Academic Employment

- Lecturer, Aerospace Engineering Department, King Fahd University of Petroleum and Minerals, Dhahran, Saudi Arabia, May 2019 - Present.
- Graduate Teaching Assistant, School of Aeronautics and Astronautics, Purdue University, West Lafayette, Indiana, USA, Jan. 2024 - May 2024.
- Graduate Assistant, Aerospace Engineering Department, King Fahd University of Petroleum and Minerals, Dhahran, Saudi Arabia, Feb. 2016 - May 2019.

Publications

Journal Papers

- Ghazzawi, S. M., & Tallman, T. N. (2024). Transverse Strain-Induced Resistivity Variations in Fiber-Reinforced Nanocomposites: A Concentric Cylindrical Model Analytical Model. Manuscript in preparation.
- Ghazzawi, S. M., & Tallman, T. N. (2024). Computational Analysis of Piezoresistivity in Fiber-Reinforced Nanofiller-Modified Composites at the Fiber Tow Level: A Comparative Study of Analytical Predictions and Computational Models. Manuscript in preparation.

- Ghazzawi, S. M., & Tallman, T. N. (2023). Deformation-dependent electrical resistivity of fiber-reinforced nanocomposites: A concentric cylindrical model approach. *Composites Science and Technology*, 243, Article 110251.

- Ghazzawi, S. M., & Abdelrahman, W. G. (2020). Static Analysis of Thick Functionally Graded Plates with Different Property Distribution Functions. *Arabian Journal for Science and Engineering*, 45(7), 5099-5108.

Conference Proceedings

- Ghazzawi, S. M., & Tallman, T. N. (2023, September). An Analytical Model for the Transverse Piezoresistive Response of Fiber-Reinforced Nano-Modified Polymers via an Electrical Concentric Cylinders Assemblage Approach. In *Smart Materials, Adaptive Structures and Intelligent Systems* (Vol. 87523, p. V001T01A009). American Society of Mechanical Engineers.

- Ghazzawi, S. M., & Tallman, T. N. (2022, September). On the Development of a Concentric Cylindrical Model for the Deformation-Dependent Electrical Resistivity of Fiber-Reinforced Composites. In *Smart Materials, Adaptive Structures and Intelligent Systems* (Vol. 86274, p. V001T05A003). American Society of Mechanical Engineers.

- Koo, G. M., Ghazzawi, S., & Tallman, T. N. (2022, April). The effect of inter-filler transport on AC piezoresistivity in CNF-modified epoxy nanocomposites. In *Sensors and Smart Structures Technologies for Civil, Mechanical, and Aerospace Systems 2022* (Vol. 12046, pp. 61-68). SPIE.

- Ghazzawi, S. M., & Abdelrahman, W. G. (2019). Effect of transverse shear deformation on static and dynamic responses of classes of thick functionally graded panels. In *AIAA Scitech 2019 Forum* (p. 1966).